ANGULAR TRAPPING OF A MIRROR USING RADIATION PRESSURE

By

David B. Kelley

B.S. Massachusetts Institute of Technology, Cambridge, MA, 2010
M.S. Syracuse University, Syracuse, NY, 2013

Dissertation
Submitted in Partial Fulfillment of the Requirements
for the degree of
Doctor of Philosophy in Physics

Syracuse University
November 2015

ANGULAR TRAPPING OF A MIRROR USING RADIATION PRESSURE

By

David B. Kelley

B.S. Massachusetts Institute of Technology, Cambridge, MA, 2010
M.S. Syracuse University, Syracuse, NY, 2013

Dissertation
Submitted in Partial Fulfillment of the Requirements
for the degree of
Doctor of Philosophy in Physics

Syracuse University
November 2015

Approved : _____
Prof. Stefan Ballmer

Date : _____

ABSTRACT

Alignment control in gravitational-wave detectors has consistently proven to be a difficult problem due to the stringent noise contamination requirement for the gravitational wave readout and the radiation-pressure induced angular instability in Fabry-Perot cavities (Sidles-Sigg instability). In this thesis, I present optical springs as a tool to damp the motion of a mirror. I discuss the design and implementation of a single degree-of-freedom optical spring system and the importance of the photothermal effect in properly predicting optical spring behavior.

I also present the development and implementation of an angular control scheme, attempting to damp two degrees of freedom with two optical cavities. I then extend this understanding into a plausible concept for implementing optical-spring-based angular control in the Advanced LIGO detectors.

Contents

List of Tables

List of Figures

Preface

The work presented in this thesis stems from my participation in the LIGO Scientific Collaboration (LSC). This work does not reflect the scientific opinion of the LSC and it was not reviewed by the collaboration.

The theory of optical trapping in two degrees of freedom in chapter 2 is based on

A. Perreca *et al.*, "Multi-dimensional optical trapping of a mirror," *Phys. Rev. D* **89** (2014) 122002.

Chapter 5 is based on

D. Kelley *et al.*, "Observation of photo-thermal feed-back in a stable dual-carrier optical spring," *Phys. Rev. D* **92** (2014) 062003.

This document has been given the LIGO DCC number LIGO-P1500223.

Acknowledgments

I would like to thank a number of people for helping me during the course of my studies. Without any one of these people, this would have been a far less productive experience.

My adviser, Stefan Ballmer, provided a vast trove of knowledge and many helpful insights in lab.

Antonio Perreca, as a postdoc and my friend, gave me invaluable lessons in optics, organization, and life in general.

James Lough, Fabian Mangaña-Sandoval, and Thomas Vo, as my cohort in lab, have kept me going in the right direction and shared in many victories, both small and large.

Peter Saulson has provided much appreciated guidance and insights about everything from dielectric mirrors to regional variations in breakfast preferences.

Lou Buda, Charlie Brown, Phil Arnold, and Lester Schmutzler have provided me with countless hours of help, advice, and conversation.

Joan Kelley made a custom dust cover for the vacuum chamber that proved very useful and durable.

Emma Tolley has graciously listened to my rambling about optics in the wee hours of the morning, and has remained supportive despite it.

to

my parents and Emma

Chapter 1

Introduction

The Advanced Laser Interferometer Gravitational-Wave Observatory (aLIGO) is part of an international effort to detect gravitational waves. The search resumed this year with the two aLIGO sites in Washington and Louisiana, and will ramp up to full design sensitivity over the following few years.

1.1 Basic layout of aLIGO

In its simplest form, aLIGO is a Michelson interferometer with Fabry-Pérot cavities for arms (see figure 1). In each Fabry-Pérot cavity, the mirror closer to the Michelson beam splitter is called the input test mass (ITM) and the other mirror is called end test mass (ETM).

A gravitational wave approaching from the zenith causes changes in the distance between the ETM and ITM in each cavity. Because the wave is quadrapolar, the changes in the x direction will have the opposite sign of the changes in the y direction. This causes a relative phase shift in each of the arms in opposite directions. When they recombine at the beam splitter, the phase shifts cause changes in the interference between the two beams, changing the amount of power at the the output port. We can detect these power fluctuations to reconstruct the phase shift and thus the strain, $h = \Delta L/L$ experienced by the interferometer due to the gravitational wave. We then use techniques like matched filtering to compare the strain signal from the interferometer to models of expected signals to search for events hidden in the noise background of the interferometer.

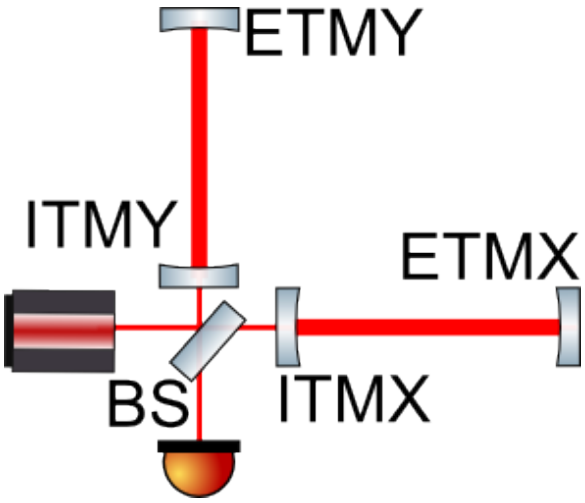

Figure 1 : In its simplest form, aLIGO is a Michelson interferometer with Fabry-Pérot cavities for arms. Light from the laser is split by the beam splitter (BS), then enters the arm cavities through the input test masses (ITMX and ITMY). Power builds up in the cavity between input and end test masses (ETMX and ETMY). When a gravitational wave passes through the detector, it shifts the phases of light in the two arms in opposite directions. Because the cavity is over-coupled ($r_{ITM} < r_{ETM}$), light leaves the arm cavities and goes back to the BS. The phase-shifted light from the two cavities interferes at the BS, producing the error signal that we measure with a photodiode.

With the goal of suppressing the noise and improving the signal, many changes have been made to the initial simple interferometer. The masses have been upgraded to 40 Kg and suspended from quadruple pendulum systems to reduce seismic noise. Mirrors have been installed for power and signal recycling to maximize the laser power in the arms. This has already led us to an increase in range by a factor of almost 3. In addition, aLIGO plans to upgrade the current input laser power from 25 watts to 125 watts, which should bring the final range of the detectors over 200 Mpc for binary neutron star systems.

However, an increase in laser power includes several challenges. One such effect that will scale with power is the Sidles-Sigg instability [1]. In simple terms, the Sidles-Sigg instability comes from angular or beam spot location displacements that cause torques on the mirrors and gets stronger as the intra-cavity power increases. One mode is called the "hard mode" and the other is called the "soft" mode. They are described in more detail in Chapter 7. This effect must be dealt with by using active controls on the angular degrees of freedom of the test masses.

We want to develop a method to control the angular motion and damp the Sidles-Sigg instability of the ITMs and ETMs as we increase the laser power. We know that increasing the gain of the current angular control system will result in more noise from photodiodes (sensing noise) being injected into the system, which may limit the sensitivity of the instrument. We think that optical springs can offer a robust control system that is not subject to sensing noise, which would be a very good solution.

1.2 Optical Springs

Optical spring is a term used to describe the linear region of the interaction between cavity length and radiation pressure force in a detuned Fabry-Pérot cavity.

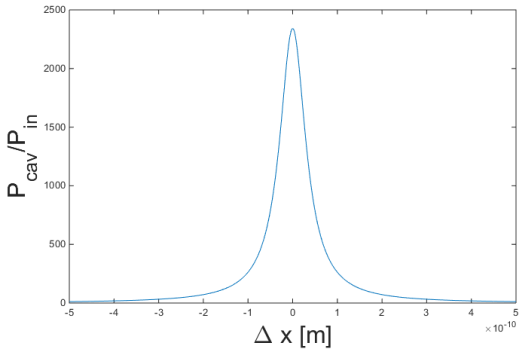

Figure 2 : Optical power in a critically coupled cavity near resonance. The height of the peak is determined by the reflectivities of the two mirrors and the input power. When the cavity is close to but not on resonance, power scales approximately linearly with the cavity length.

The radiation pressure force is given by

$$F = \frac{P_{cav}}{2c}. \tag{1.1}$$

In a cavity with varying length Δx, we expect the cavity power P_{cav} to follow [2] (see figure 2):

$$P_{cav} = P_{in} \left| \frac{t_1}{1 - r_1 r_2 e^{\frac{-4i\pi\Delta x}{\lambda}}} \right|^2, \tag{1.2}$$

where t_1 and r_1 are the amplitude transmisivity and reflectivity of the input mirror and r_2 is the reflectivity of the end mirror. λ is the wavelength

We can see that there are approximately linear regions on both sides of resonance. This is the basis of a pragmatic explanation of optical spring behavior, demonstrated in figure 3. In this demonstration, we see the effects of "red" and "blue" detuning, where the cavity resonant length is longer and shorter, respectively, than the cavity itself. The color association of these detunings comes from the laser frequency shift that could accomplish this detuning: red is a negative frequency detuning and blue is a positive frequency detuning.

In figure 3, we explore four different situations. For each one, I have drawn the resonant power (radiation pressure force) buildup in the cavity as a function of position. I have also shown an effectively static force due to a mechanical spring. It is important to note that we treat this as constant over position and time scales that we are dealing with.

In the first case, we address a red-detuned cavity in the adiabatic, or essentially stationary, case. As the mirror moves away from its equilibrium point, it experiences more force in the direction of displacement. In the blue-detuned case, we see that the net force is pushing the mirror back to its equilibrium position. Thus the red-detuned cavity is statically unstable, while the blue-detuned cavity is statically stable.

In the other case, we address a mirror that is in motion. This cavity will experience the radiation pressure force due to the position of the mirror in the recent past, determined by light storage time. In the red-detuned case, we see that the time-delayed force has an overall damping effect on the motion of the mirror. In the blue-detuned case, we get the opposite, anti-damping behavior.

In summary, we see that a blue-detuned cavity is statically stable and dynamically unstable, while a red-detuned cavity is statically unstable and dynamically stable.

We can describe an optical spring as having a spring constant that follows Hooke's law ($F = -kx$). In this case, we treat damping as an imaginary component to the spring constant. Thus, a blue-detuned optical spring has a positive real part and a negative imaginary part, while a red-detuned optical spring has a negative real part and a positive imaginary part. However, since these optical springs behave like normal springs, you can use two differently detuned laser beams and add the spring constants of two of them together to arrive at a stable spring (see figure 4). The stability and behavior is discussed in more detail in Section 2.3.2.

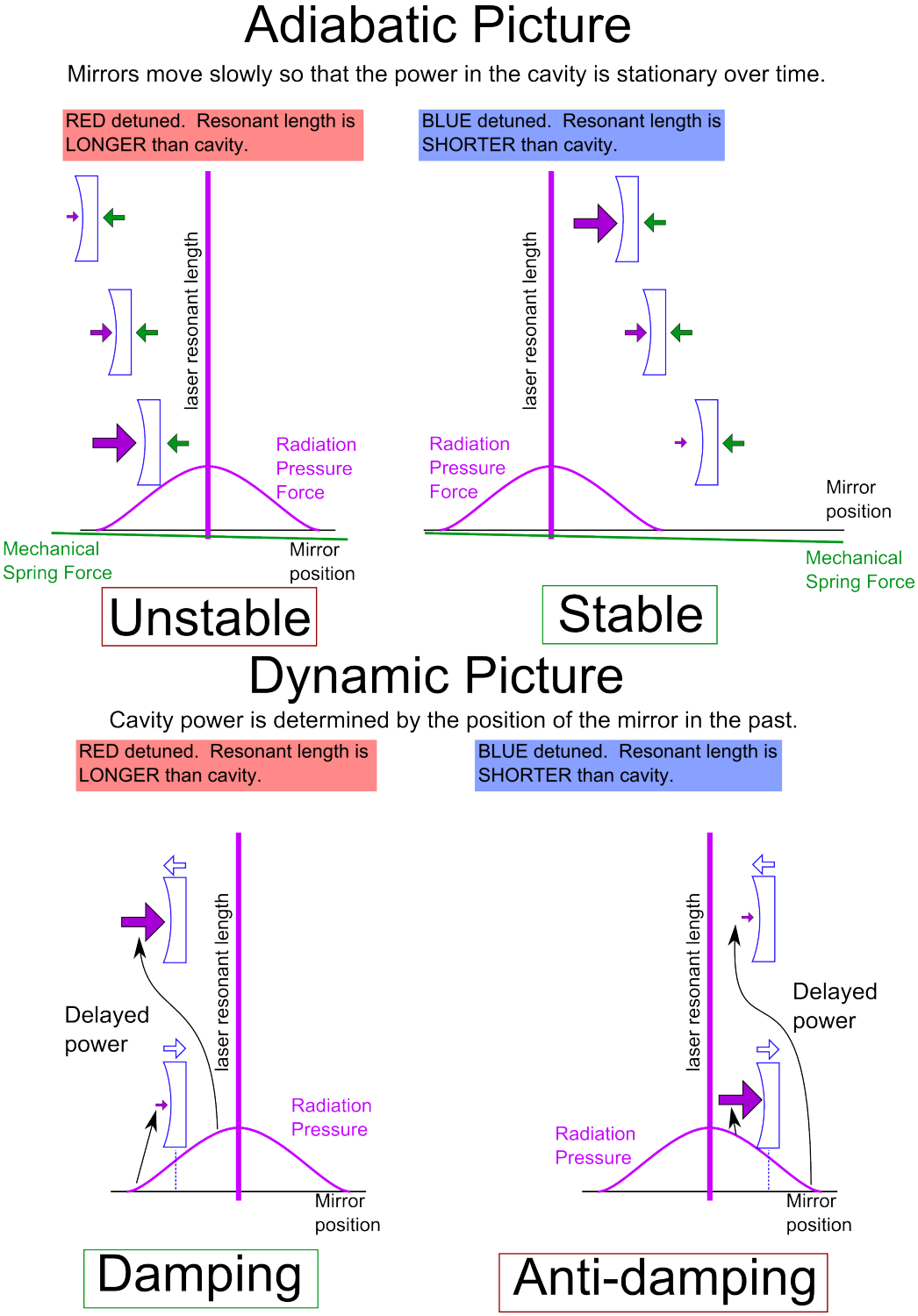

Figure 3 : Stability behavior of detuned cavities (optical springs). It is important to note that we rely on a constant force (green arrows) exerted on the mirror to choose the equilibrium point of the optical spring.

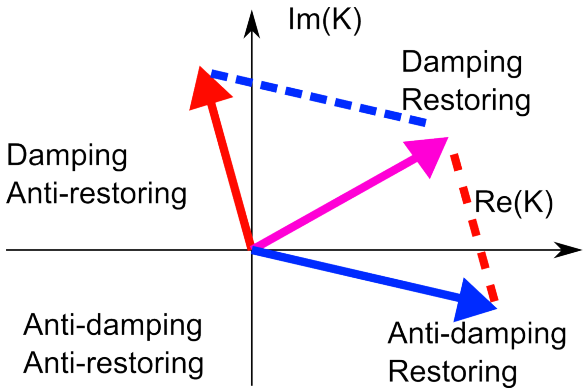

Figure 4 : We can add two unstable optical springs to make a system that is statically and dynamically stable. Note: this picture only makes sense in the low-frequency regime.

1.3 Photothermal Effect

One very important phenomenon that affects any high-finesse cavity is the photothermal effect. There are three different aspects that we will focus on: the bulk behavior, the spot size correction, and the coating correction. The diffusion length gives the characteristic distance that the effects of heat will travel:

$$d_{diff} = \sqrt{\kappa/(\rho C \Omega)}, \tag{1.3}$$

where κ, C and ρ are the thermal conductivity, heat capacity and density of the material, and Ω is the observation angular frequency.

The bulk behavior is due to the thermal expansion of the mirror due to heat absorption. This causes shortening of the optical cavity.

For small spot size and low frequency, we require a spot size correction due to the finite spot size of the laser beam. Heat will dissipate radially, reducing the overall amount of heat at the contact point.

Finally, for high frequencies (short diffusion lengths), we must include the coating correction. It becomes significant when most of the heat deposited is in the coating, i.e. d_{diff} is less than the coating thickness. In this scenario, expansion of the first layer can actually increase the round-trip optical path length, working in the opposite direction of the bulk behavior.

The formulation and measurement of the photothermal effect will be discussed in more detail in Chapter 5.

1.4 Summary

In the rest of this thesis, we will discuss the implementation and use of optical spring systems to investigate and control optomechanical systems. Chapter 2 gives a rigorous discussion of the theory of angular trapping. Chapter 3 discusses the suspensions and control loops required to isolate, reposition, and damp the optics. Chapter 4 covers the feedback systems used to generate the frequency-detuned beam and lock the optical spring cavities. Chapter 5 details the single-dimensional trap and the measurement of the photo-thermal effect. Chapter 6 discusses the implementation of the angular trap. Chapter 7 discusses how we could implement an angular control scheme using radiation pressure in aLIGO.

Chapter 2

Multidimensional optical trapping of a mirror

The following chapter is taken from a paper, "Multidimensional optical trapping of a mirror" by Antonio Perreca, James Lough, David Kelley, and Stefan W. Ballmer. It was published in Physical Review D, volume 89, issue 12, on June fifth, 2014 [3].

2.1 Abstract

Alignment control in gravitational-wave detectors has consistently proven to be a difficult problem due to the stringent noise contamination requirement for the gravitational wave readout and the radiation-pressure-induced angular instability in Fabry-Perot cavities (Sidles-Sigg instability). We present the analysis of a dual-carrier control scheme that uses radiation pressure to control a suspended mirror, trapping it in the longitudinal degree of freedom and one angular degree of freedom. We show that this scheme can control the Sidles-Sigg angular instability. Its limiting fundamental noise source is the quantum radiation pressure noise, providing an advantage compared to the conventional angular control schemes. In the Appendix we also derive an exact expression for the optical spring constant used in the control scheme.

2.2 Introduction

The Laser Interferometer Gravitational-Wave Observatory (LIGO) is part of a worldwide effort to detect gravitational waves and use them to study the Universe [4]. Construction of LIGO's advanced detectors is underway. The installation is expected to finish in 2014. The goal of Advanced LIGO (aLIGO) is the first direct detection of gravitational waves from astrophysical sources such as coalescing compact binaries and core-collapse supernovae. These detections will open a new spectrum for observing the Universe and establish the field of gravitational-wave astronomy. These initial observations will also show the potential science gain of further increasing the state-of-the-art sensitivity of gravitational-wave detectors [5, 6, 7]. Such detectors operate near the standard quantum limit, meaning that the contributions from quantum radiation pressure and shot noise are about equal in the observation band [8, 9].

To design a successor to aLIGO, techniques to operate gravitational-wave interferometers below the standard quantum limit need to be developed [10, 11]. Dual carrier control systems and angular control using stable optical springs are promising methods for evading quantum-mechanical limitations on detector sensitivity [12, 13, 14, 15, 16, 17]. In 2007 Corbitt *et al.* at the LIGO Laboratory at the Massachusetts Institute of Technology demonstrated a one-dimensional optical trap of a one gram mirror using a novel two-carrier scheme [18]. Their work clearly demonstrated the potential of this technique. Extended to angular degrees of freedom, it has the prospect of opening a completely new approach to the angular control problem in future generation gravitational-wave detectors [19]. Sidles and Sigg have shown that, for a Fabry-Perot cavity with a single resonating laser field, the radiation pressure force will couple the two end mirrors, always creating one soft (unstable) and one hard (stable) mode [1]. This sets a lower limit on the required angular control bandwidth, which inevitably results in higher noise contamination by angular control noise and limits the angular control performance in the first and second generation gravitational-wave interferometers [12, 20, 21, 22]. As we will show in Sec. 2.5, angular optical trapping can bypass the Sidles-Sigg instability. Its fundamental noise limit is quantum radiation pressure noise. By design it is not affected by sensing noise, making it a promising candidate for low-noise angular control. Additionally, optical trapping can be used to cool a

mechanical degree of freedom. Radiation pressure-based cooling is the preferred approach for cooling to the quantum ground state in the limit where the cavity line width is smaller than the mechanical frequency (good cavity limit)[23]. It can enable the manipulation of a macroscopic object at the quantum level [24, 25, 26, 27, 28]. However reaching the quantum ground state requires reducing the total rms motion, rather than the spectral density in the frequency band above the mechanical suspension resonance, as desired for a low-noise angular control system. We therefore will not further explore reaching the quantum ground state.

In this paper we present a prototype of a position and yaw optical trap for a suspended test mirror using a double dual-carrier control scheme. With mechanical suspension frequencies around 1 Hz such a system is, in virtually all cases, in the bad cavity limit; i.e., the cavity line widths are larger than the mechanical frequencies. We propose a system with two longitudinal traps acting on different spots of a single mirror; together, these traps will constrain both the position degree of freedom and one angular degree of freedom of the mirror. This essentially replaces the current magnetic drives with optical traps. The idea is promising and will be easy to apply to the other angular degree of freedom. The model includes two optical cavities with the trapped end-mirror in common. Each cavity is illuminated with two overlapping laser beams at different frequency detunings: one is positive detuned (blue detuning) and the other is negative detuned (red detuning). The two dual beams form two statically and dynamically stable optical springs with different lever arms and different power, designed such that the static (commonly named DC) radiation pressure torques of the two dual beams cancel each other while DC radiation pressure force is canceled by displacing the position pendulum.

As a result, by picking the right parameters, we can obtain a system that is stable in the longitudinal and angular degrees of freedom with a mirror displacement range of the order of picometers.

The outline of this paper is as follows. In Sec. 2.3 we review the idea of an optical spring. We then couple optical springs to a mechanical system and analyze the stability of the resulting optomechanical system. Section 2.4 extends the stability analysis to more than one dimension. In Sec. 2.5 we show that such a two-dimensional optical spring is necessarily stronger than the Sidles-Sigg instability. In Sec. 2.6 we calculate the radiation pressure noise, which is the fundamental limiting noise for

radiation pressure control. Finally, in Appendix 2.7, we derive the approximation-free expression for the optical spring in a Fabry-Perot cavity, which to our knowledge has not been published yet.

2.3 Stability principle

An optically detuned Fabry-Perot cavity naturally leads to a linear coupling between intracavity power and mirror position. Depending on the sign of the detuning, this coupling creates an optical spring which is either statically stable or unstable. Due to the time delay in the optical field build-up, the optical spring restoration force is slightly delayed. This leads to a dynamically unstable spring for the statically stable case and a dynamically stable spring for the statically unstable case. Corbitt *et al.* [18] demonstrated that by adding a second, frequency-shifted optical field (subcarrier) with a different detuning and power, a statically and dynamically stable optical spring can be achieved. The dual-carrier scheme has been used to optically trap a gram-scale mirror, controlling its longitudinal degree of freedom. Moreover, the damping of the optical spring can be controlled by adjusting the detuning of both carrier and subcarrier and their relative amplitudes. This naturally allows for efficient cooling of the degree of freedom seen by the optical spring. In contrast to a mechanical spring, this damping does not introduce intrinsic losses, and thus does not contribute to the thermal noise.

This technique can be extended to alignment degrees of freedom. By duplicating the Corbitt *et al.* approach for trapping with a second, different, optical axis and a different beam spot on the controlled mirror, it is possible to control the angular degree of freedom with radiation pressure alone.

To be able to understand the stability of multidimensional optomechanical systems, we first recall the simple driven damped mechanical oscillator. From there we will stepwise increase the complexity by adding optical springs and additional degrees of freedom.

2.3.1 Damped mechanical oscillator stability

Although the damped mechanical oscillator is a well known system, we will take it as a starting point to make the reading clearer. Our goal is to describe the mechanical

oscillator in the language of control theory, which allows us to understand the stability of the system from a different point of view. This approach can then be naturally extended to include the effect of additional optical springs.

The motion of a harmonic oscillator of mass m, spring constant k_m and velocity damping b, driven by the external force F_{ext}, can be expressed as [29]

$$m\ddot{x} = -k_m x - b\dot{x} + F_{ext} \tag{2.1}$$

where b is also called the viscosity coefficient. Often the damping rate $\Gamma = b/(2m)$ is used instead. Traditionally the Eq. (2.1) is directly used to get the system's position response x when applying the external force F_{ext}. The resulting transfer function is

$$G = \frac{x}{F_{ext}} = \frac{1}{-m\Omega^2 + k_m + ib\Omega} \tag{2.2}$$

where Ω is the angular frequency of the motion.

Alternatively we can describe a damped mechanical oscillator as a feedback system, with the plant being just a free test mass described by the transfer function $M = x/F_{ext} = -1/m\Omega^2$, obtained directly from the equation of motion of a free test mass. The control filter of the feedback loop is the mechanical spring, which takes the mass displacement x as input and acts on the plant with the control signal, or force, F_K, which is subtracted from the external force F_{ext}. The transfer function of the control filter is $K_M = F_K/x = k_m + ib\Omega$. In this picture we can now calculate the closed loop transfer function and obtain the same expression as in Eq. (2.2),

$$G = \frac{M}{1 + K_M M} = \frac{1}{-m\Omega^2 + k_m + ib\Omega} \tag{2.3}$$

where $OL_M = -K_M M = (k_m + ib\Omega)/m\Omega^2$ describes the open loop transfer function of the system.

Stability

We can now check for the stability of the system in both pictures. We recall from literature that the stability of a system described by its transfer function G can be evaluated looking at the poles of its transfer function in the s-plane ($s = i\Omega$) [30]. In particular a system is stable only if its transfer function's poles have a negative real

part, and the multiplicity of poles on the imaginary axis is at most 1. The transfer function in Eq. (2.2) has the following poles:

$$i\Omega = -\frac{b}{2m} \pm \sqrt{\frac{b^2}{4m^2} - \omega_0^2}, \tag{2.4}$$

where $\omega_0^2 = k_m/m$ is the resonant frequency of the pendulum. The value of the damping rate $\Gamma = b/2m$ compared to ω_0 determines whether the system is overdamped, underdamped or critically-damped. But since Γ (or b) is always positive, the real part of the poles is always negative. The system is thus always stable.

From the control theory point of view, the stability can also be evaluated with no loss of generality by considering the open loop transfer function $OL_M = (k_m + ib\Omega)/m\Omega^2$ and applying, for example, the Bode stability criterion [31]. The positivity of b guarantees an always positive phase margin and therefore stability. In the reminder of this work, for simplicity, we will test the stability of the control scheme using the Bode graphical method.

2.3.2 Optical spring: A classical model

Next, we look at an optical spring. We start with a Fabry-Perot cavity of length L_0, frequency detuning δ (rad/Hz), amplitude transmittance coefficients t_1, t_2 and amplitude reflectance coefficients r_1, r_2 of the input and output cavity mirror respectively. The light field inside the cavity builds up and exerts a radiation pressure force on both mirrors.

We define the propagator $X = r_1 r_2 e^{-2i\delta\tau}$ and phase factor $Y = e^{-i\Omega\tau}$, with $\tau = L_0/c$ the one-way travel time of the photon inside the cavity, k is the wave vector of the light field and Ω is the mechanical frequency of the pendulum. From this we can obtain an elastic force-law for small displacement values x, but potentially large detuning from resonance:

$$F_{rad} = F_0 - K_{OS} \cdot x + O(x^2), \tag{2.5}$$

where

$$K_{OS} = K_0 \left[\frac{Y^2}{(1 - Y^2 X)(1 - Y^2 \overline{X})} \right] \tag{2.6}$$

is the optical spring constant and $\overline{X}$ is the complex conjugate of X. Here K_0 is the (mechanical) frequency-independent part of the spring constant:

$$\begin{aligned} K_0 &= F_0 \cdot 2ik \cdot (X - \overline{X}), \quad \text{with} \\ F_0 &= P_0 \cdot \frac{2r_2^2}{c} \cdot \frac{t_1^2}{(1-X)(1-\overline{X})} \end{aligned} \tag{2.7}$$

The expression in Eqs. (2.6) and (2.7) is the general expression for K_{OS} up to linear order in x. While approximations for this formula have been published before [32], we are not aware of a previous publication providing the full expression. We address the complete derivation of the optical spring constant K_{OS} in Appendix 2.7. There we also show that with the approximations $2\Omega\tau \ll 1$ and $2\delta\tau \ll 1$ Eq. (2.6) is equivalent to the expressions already existing in literature [32, 18].

We note that K_0 is a real number. Its sign is determined by the imaginary part of X. A positive sign is associated with positive detuning ($\delta > 0$) and a restoring force (statically stable), while a negative sign is due to negative detuning ($\delta < 0$) and leads to a antirestoring force (statically unstable). Also, for small (positive) frequencies $\Omega\tau \ll 1$, the sign of the imaginary part of Eq. (2.6) is opposite to its real part, leading to positive dynamic feedback for the statically stable case and negative dynamic feedback for the statically unstable case.

Our next step is to couple the optical spring to a mechanical pendulum. We can treat this as either a damped mechanical oscillator with transfer function G, controlled by an optical spring K_{OS}, or as a free mass with transfer function M, controlled by the total feedback filter $H = K_M + K_{OS}$, see Fig. 5. In both cases we obtain the same closed-loop transfer function, equivalent to the one we would have obtained by rewriting the equation of motion of a damped mechanical oscillator with an optical spring:

$$\begin{aligned} G_{CL} = \frac{x}{F_{ext}} &= \frac{G}{1 + K_{OS}G} = \frac{M}{1 + HM} \\ &= \frac{1}{-m\Omega^2 + K_M + K_{OS}} \end{aligned} \tag{2.8}$$

The stability of the total system can again be evaluated by either looking at the poles of the closed-loop transfer function G_{CL}, or looking at the gain and phase margin of the open loop transfer function $OL_{MH} = -H/m\Omega^2$. The latter is generally more convenient. Unless compensated by large mechanical dissipation in K_M, the positive

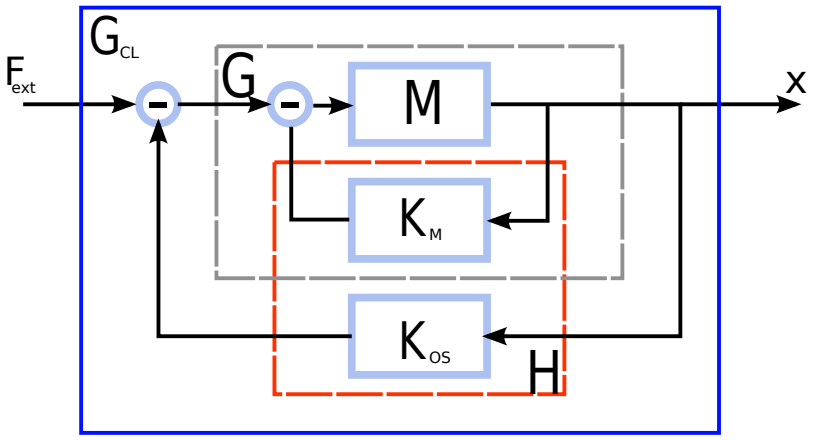

Figure 5 : Mechanical oscillator and feedback systems. The mechanical oscillator can be seen as plant (G) and the optical spring K_{OS} as feedback or alternatively as free test mass (plant M) and $H = K_{OS} + K_M$ as feedback. Both the cases lead to the same closed loop transfer function G_{CL} which describes the system as a damped mechanical oscillator in the presence of the optical spring, which is subjected to the external force F_{ext} and has the corresponding displacement x as output.

dynamic feedback for the statically stable case ($\delta > 0$) leads to a dynamically unstable system. Intuitively this can be understood as a phase delay in the radiation pressure build-up which is caused by the cavity storage time. For $\delta < 0$ the system is statically unstable.

2.3.3 Double carrier spring

The seemingly intrinsic instability of optical springs can be overcome by a scheme proposed by Corbitt *et al.* [18]. The carrier is set at a large positive detuning ($\delta > 0$, large $|\delta|/\gamma$, where γ is the line width). This provides a static restoring force, together with a relatively small dynamic instability (antidamping). Then a subcarrier is added at lower power and with a small negative detuning ($\delta < 0$, small $|\delta|/\gamma$). The subcarrier adds sufficient damping to stabilize the total optical spring, while leaving the sign of the static restoring force unchanged. For appropriately chosen parameters of carrier (c) and subcarrier (sc) (power P_0^c and P_0^{sc}, detuning δ_c and δ_{sc}) the resulting total system thus becomes stable.

The spring constant of the total optical spring is simply the sum of the individual spring constants of the carrier and subcarrier,

$$K_{OS} = K_{OS}^c + K_{OS}^{sc}, \tag{2.9}$$

where the individual springs K_{OS}^{c} and K_{OS}^{sc} are given by Eq. (2.8).

Conceptually we can think of the dual-carrier optical spring as a physical implementation of a feedback control filter for the mechanical system. With this tool at hand, we can start to analyze the behavior and stability of higher-dimensional mechanical systems in the next section.

2.4 Control model of longitudinal and angular degrees of freedom

We will now extend our analysis to additional degrees of freedom. Experimentally, a torsion pendulum suspension is easy to build. Therefore we will focus our attention to controlling the yaw motion of a test mirror, keeping in mind that the method can be applied to any additional degree of freedom. For actively controlling two degrees of freedom (length and yaw), we need a two-dimensional control system. In other words, we will need a second dual-carrier optical spring in a setup that for example looks like Fig. 6. We will label the two dual-carrier optical fields as beams A and B. Each beam includes a carrier and a subcarrier field, i.e.

$$\begin{aligned} \text{beam}A &= \text{carrier}A + \text{subcarrier}A \\ \text{beam}B &= \text{carrier}B + \text{subcarrier}B. \end{aligned} \tag{2.10}$$

The two beams have a different optical axis, and each has its own optical spring constant, K_{OS}^{A} and K_{OS}^{B}, given by Eq. (2.9).

If we define x_A and x_B as the longitudinal displacement of the mirror at the contact points of beam A and beam B on the test mirror, and F_A and F_B as the corresponding exerted forces, we can describe the mechanical system with a plant matrix M:

$$\begin{pmatrix} x_A \\ x_B \end{pmatrix} = M \begin{pmatrix} F_A \\ F_B \end{pmatrix}. \tag{2.11}$$

The explicit expression for M for a torsion pendulum is given in Appendix 2.8.

The control is provided by the optical springs. In the x_A-x_B basis the control matrix H is diagonal and given by (also see Fig. 7)

$$\begin{pmatrix} F_A \\ F_B \end{pmatrix} = H \begin{pmatrix} x_A \\ x_B \end{pmatrix} = \begin{pmatrix} K_{OS}^{A} & 0 \\ 0 & K_{OS}^{B} \end{pmatrix} \begin{pmatrix} x_A \\ x_B \end{pmatrix}. \tag{2.12}$$

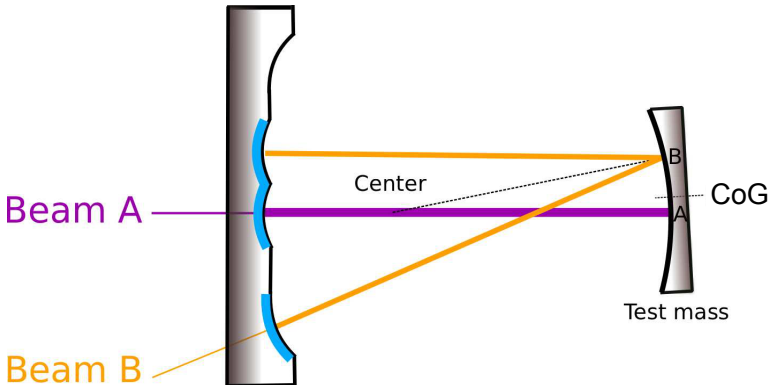

Figure 6 : In this sketch the main purple (beam A) optical axis hits the test mirror at point A, slightly displaced from the center of gravity (CoG), such that it still corresponds mainly to the length degree of freedom. Thus the second orange (beam B) optical axis, which hits the test mirror closer to the edge at point B, needs much less power to balance the total DC torque. In our test setup the large input coupler is a composite mirror. It is 600 times more massive than the small mirror. The choice of a V-shaped beam B results in a more practical spot separation on the input coupler.

For a multidimensional feedback system to be stable, it is sufficient that each individual (one-dimensional) feedback loop is stable, assuming all remaining control loops are closed. In other words, in our two-dimensional optomechanical system, we close the beam B control filter for evaluating the open loop transfer functions OL_A, and vice versa. For the open loop transfer functions OL_A and OL_B we then find:

$$\begin{aligned} OL_A &= e_A^T \left(\mathbb{1} + HM(\mathbb{1} - e_A e_A^T)\right)^{-1} HMe_A \\ OL_B &= e_B^T \left(\mathbb{1} + HM(\mathbb{1} - e_B e_B^T)\right)^{-1} HMe_B, \end{aligned} \tag{2.13}$$

with $e_A^T = (1,0)$ and $e_B^T = (0,1)$. The derivation of this expression is given in Appendix 2.9.

2.4.1 An example

It is worth considering a specific set of possible values for our model and evaluate the control of angular and longitudinal degrees of freedom of a gram-scale test mirror using the radiation pressure of the light. All the optical fields involved in our analysis are derived from the same wavelength light source through frequency shifting. The model includes two optical cavities (Fig. 6), referred to as beam A and B, both with an optical finesse of about 8500, line width $\gamma/(2\pi) = 125\,\mathrm{kHz}$ and mechanical frequency

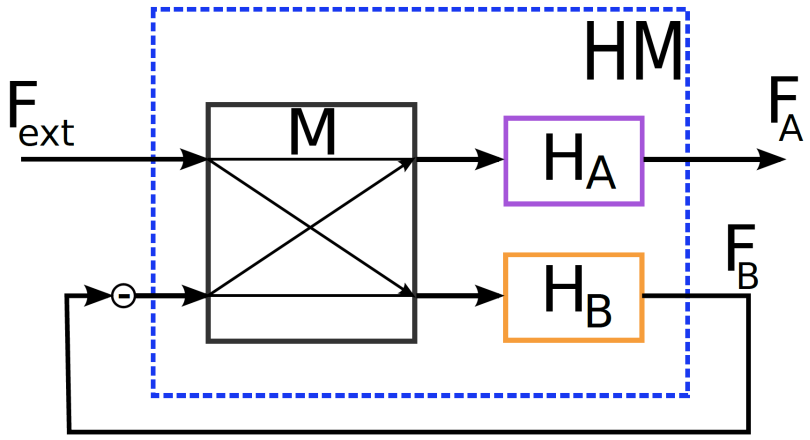

Figure 7 : Block diagram of beam A and beam B. The transfer function F_A/F_{ext} is equal to OL_A from Eq. (2.13). Each loop affects the other resulting in cross terms present in the matrix HM. M and $H_{A,B}$ are the transfer functions of the mechanical system and the optical springs of beam A and B, respectively.

of $\backsim$ 1 Hz. The main cavity (beam A) is pumped with 1 W of carrier light, detuned by $\delta/(2\pi) = 250$ kHz (blue detuning, $\delta/\gamma = 2$), and 0.2 W of subcarrier light, detuned by $\delta/(2\pi) = -62$ kHz (red detuning, $\delta/\gamma = -0.5$). This produces a statically and dynamically stable optical spring with a lever arm of 0.8 mm, measured from the mirror center of gravity. A second optical spring (beam B) is pumped with 6 times less power of carrier light, detuned by = 186 kHz (blue detuning, $\delta/\gamma = 1.5$), and 40 mW of subcarrier light, detuned by 62 kHz (red detuning, $\delta/\gamma = -0.5$). This side cavity has a lever arm of 3.3 mm on the mirror, such that the DC radiation pressure torques of beam A and B cancel. The DC radiation pressure force can be canceled by displacing the position pendulum.

The stability of the combined two-dimensional system is addressed in Fig. 8. Plotted are the open loop gain functions of the two degrees of freedom (the two optical traps) under the assumption that the other loop is closed. The presence of the second loop introduces a resonance feature in each loop at the unity gain frequency of the other loop. However the open loop gain avoids the critical point -1 (phase at 180), leading to a stable system. The model parameters were intentionally tuned for low damping / high quality factor in order to demonstrate that the system remains stable. Lower quality factors, and therefore stronger cooling is easily achievable.

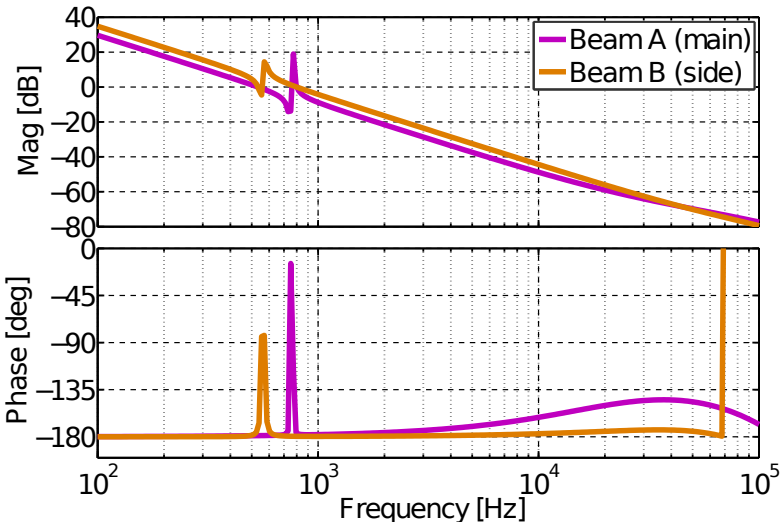

Figure 8 : Open loop gain (OLG) for the main and side cavity. The respective other loop is closed, and shows up as a resonance in the OLG. Note that, despite multiple unity gain crossings, both loops are stable because the resonances effectively implement a lead filter and the OLG avoids the critical point -1. Thus the dynamic interplay between multiple trapping beams on one payload does not introduce an instability.

2.4.2 Stability range

We can now estimate the robustness of our feedback control system by changing the microscopic length x_A and x_B of the two cavities. This changes the detuning of the optical springs for both beams. Therefore the propagators X_A and X_B for both beams change according to $X_{A,B} = r_1 r_2 e^{-i\delta_{A,B}\tau_{A,B}} \cdot e^{ikx_{A,B}}$. For each position both the static and dynamical stability of the total optical spring system given by Eq. (2.13) is reevaluated.

In Fig. 9 the radiation pressure force due to the intracavity power of both beams versus the cavity offset is shown. The green shaded area represents the position range in which the two loops remain stable. The range is $\backsim$ 20 pm. The DC force fluctuations that the system can tolerate are given by the y-axis interval that the total radiation force spends in the green shaded area.

2.5 Angular instability

When operated with high intracavity laser power, suspended Fabry-Perot cavities like the arm cavities of LIGO have a well known angular instability. It arises from

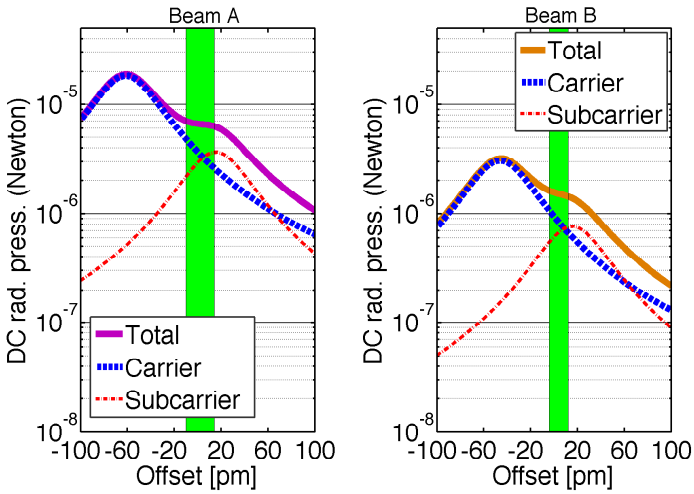

Figure 9 : Static carrier and subcarrier build-up (calibrated in radiation pressure force) as a function of the respective cavity position. Also shown in purple and orange are the total radiation pressure forces of the two cavities. Using the stability testing method from Sec. 2.4.2 we find that the trap is both statically and dynamically stable in the green shaded area. With the chosen model parameters those regions are about 20 picometers wide.

coupling the misalignment of the two cavity mirrors to radiation pressure torques. This is known as the Sidles-Sigg instability [1]. In this section we show that the intrinsic strength of an optical trap for alignment degrees of freedom is generally bigger, i.e. has a bigger spring constant than any associated Sidles-Sigg instability.

We start with a cavity of length L, with x_1, x_2 being the position of the beam spots on mirrors 1 and 2. θ_1, θ_2 are the yaw angles of the two mirrors and R_1, R_2 are their radii of curvature. The corresponding g-factors are $g_{1,2} = 1 - L/R_{1,2}$. If one or both of the mirrors are slightly misaligned ($\theta_{1,2} \neq 0$), then the radiation pressure force exerts torques T_1 and T_2 on the two mirrors, given by (see for instance [1] or [33])

$$\begin{pmatrix} T_1 \\ T_2 \end{pmatrix} = \frac{F_0 L}{1 - g_1 g_2} \begin{pmatrix} g_2 & -1 \\ -1 & g_1 \end{pmatrix} \begin{pmatrix} \theta_1 \\ \theta_2 \end{pmatrix}, \tag{2.14}$$

where $F_0 = P_0 \frac{t_1^2}{(1-X)(1-\overline{X})} \frac{2r_2^2}{c}$ is the intracavity radiation pressure force. Sidles and Sigg first pointed out that, since the determinant of the matrix in this equation is negative, the two eigenvalues have opposite sign. This always leads to one stable and one unstable coupled alignment degree of freedom.

First we note that for a situation in which one mass is sufficiently heavy that we

can neglect any radiation pressure effects on it (i.e. $\theta_1 = 0$), it is sufficient to choose a negative branch cavity (i.e. $g_1 < 0$ and $g_2 < 0$) to stabilize the setup. This is for instance the case for the example setup described in Fig. 6.

Next we want to compare the order of magnitude of this effect to the strength of an angular optical spring. If we call h the typical distance of the beam spot from the center of gravity of the mirror, and x the cavity length change at that spot, the order of magnitude of the optical spring torque is

$$T \approx \frac{F_0 L}{1 - g_1 g_2} \cdot \frac{x}{h}. \tag{2.15}$$

We can express this as the strength of an optical spring located at position h. The corresponding spring constant $K_{SS} \approx T/(hx)$. Thus we can see that

$$K_{SS} \approx \frac{F_0}{1 - g_1 g_2} \cdot \frac{L}{h^2}. \tag{2.16}$$

We now consider the adiabatic optical spring ($\Omega = 0$) in Eq. (2.7). Expressed in terms of F_0, K_{OS} becomes

$$K_{OS} = iF_0 \frac{X - \overline{X}}{(1 - X)(1 - \overline{X})} 2k. \tag{2.17}$$

Since we operate near the maximum of the optical spring, the order of magnitude of the resonance term can be estimated as

$$\frac{X - \overline{X}}{(1 - X)(1 - \overline{X})} \approx \frac{-i}{1 - |X|}. \tag{2.18}$$

Thus we can estimate the magnitude of K_{OS} as

$$K_{OS} \approx F_0 \frac{4\pi}{\lambda} \frac{1}{1 - |X|} \approx F_0 \frac{4}{\lambda} \mathcal{F}. \tag{2.19}$$

where $\mathcal{F}$ is the cavity finesse. From Eqs. (2.16) and (2.19) we see that the optical spring K_{OS} is much larger than the Sidles-Sigg instability spring K_{SS} if

$$h^2 >> \frac{\lambda L}{\pi} \frac{1}{1 - g_1 g_2} \frac{\pi}{4\mathcal{F}}. \tag{2.20}$$

Now recall that the beam spot size in a Fabry-Perot cavity is given by [34]

$$w_1^2 = \frac{\lambda L}{\pi} \sqrt{\frac{g_2}{g_1(1 - g_1 g_2)}}. \tag{2.21}$$

Assuming a symmetric cavity ($g_1 = g_2$) for simplicity, we thus find that K_{OS} dominates over K_{SS} if

$$h^2 >> w_{1,2}^2 \frac{1}{\sqrt{1-g_1 g_2}} \frac{\pi}{4\mathcal{F}}. \tag{2.22}$$

This condition is naturally fulfilled since we need to operate the angular optical spring with separate beams ($h > w_{1,2}$) and a large finesse ($\mathcal{F} >> 1$). Therefore the angular optical spring is indeed strong enough to stabilize the Sidles-Sigg instability.

2.6 Radiation pressure noise

Another advantage of radiation pressure angular control, compared to a classical approach based on photodetection and feedback, is its fundamental noise limit. The classical approach used in gravitational-wave detectors measures angular displacement of a single beam using wave-front sensors. Unlike that control method, the shot noise and other sensing noises never enter a radiation-pressure-based feedback loop. Even though technical laser noise is typically bigger in the simple cavity setup discussed in this paper, the only fundamental noise source of the scheme is quantum radiation pressure noise. In this section we give the full expression for radiation pressure noise in the case of a dual-carrier stable optical spring.

First, we note that as long as we are interested in frequencies much smaller than the any of the features in the detuned cavity transfer function, the radiation pressure noise is relatively simple. If we also assume that the end mirror has a reflectivity of 1, the one-sided ($f \geq 0$) radiation-force amplitude spectral noise density is given by

$$S_F(f) = \frac{2}{c} G_{DC} \sqrt{2\hbar\omega P_0} \tag{2.23}$$

where G_{DC} is the power gain of a static cavity in the detuned configuration, P_0 is the power of the shot noise limited beam entering the cavity, and ω is its frequency. Equation (2.23) is valid for carrier and subcarrier separately. Note that this equation does not hold if the end mirror has a finite transmissivity, as quantum fluctuations entering from that port will also contribute to the intracavity shot noise. In the case of a critically coupled cavity, this will result in an increase of the intracavity radiation-force amplitude spectral noise density by exactly a factor of 2.

To calculate the exact expression for the radiation pressure noise induced cavity fluctuations, including behavior near the cavity pole frequency, we first realize that we can calculate the radiation-force amplitude spectral noise for a static cavity, and then compute the response of the dual-carrier optical spring system to that driving force. This yields the correct answer up to first order in the size of the quantum fluctuations. For the calculation we track the quantum vacuum fluctuations entering at both ports of the cavity. We introduce F, the amplitude build-up factor for a fluctuation at frequency $f = \frac{\Omega+\delta+\omega_{res}}{2\pi}$:

$$F(f) = \frac{1}{1 - XY^2} = \frac{1}{1 - r_1 r_2 e^{-2i\delta\tau} e^{-2i\Omega\tau}}. \tag{2.24}$$

Thus, the total buildup for fluctuations entering through the input coupler (1) and the end mirror (2) are $t_1 F(f)$ and $r_1 t_2 F(f)$, where we already dropped the one-way propagation factor because it drops out in the radiation force noise calculation below. We can now introduce the notation $F_0 = F(f_0)$, $F_+ = F(f_0 + f)$ and $F_- = F(f_0 - f)$. We then get the following expression for the one-sided radiation-force power spectral density for either carrier or subcarrier.

$$S_F(f) = \frac{2}{c} S_P(f) \quad \text{and} \quad S_P(f) = G(f)\sqrt{2\hbar\omega P_0} \tag{2.25}$$

$$G^2(f) = \frac{1}{2} t_1^2 |F_0|^2 (t_1^2 + r_1^2 t_2^2)(|F_+|^2 + |F_-|^2). \tag{2.26}$$

Here P_0 is the entering carrier power, and f_0 is its frequency. We can see that we recover Eq. (2.23) in the limit $t_2 \to 0$ and $G/t_1^2 = |F_0|^2 = |F_+|^2 = |F_-|^2$. The resulting force noise from carrier and subcarrier for the cavity A in the example above (see Fig. 6) is plotted in Fig. 10 (top).

Next we calculate the response of the coupled optomechanical system to this driving force, using the following closed loop transfer function obtained from Eqs. (2.11) and (2.12):

$$x = M(1 + HM)^{-1} F \tag{2.27}$$

Above the optical spring resonances this leads to a $1/f^2$ falloff of the displacement noise, as expected for radiation pressure noise. Meanwhile below the resonance, due

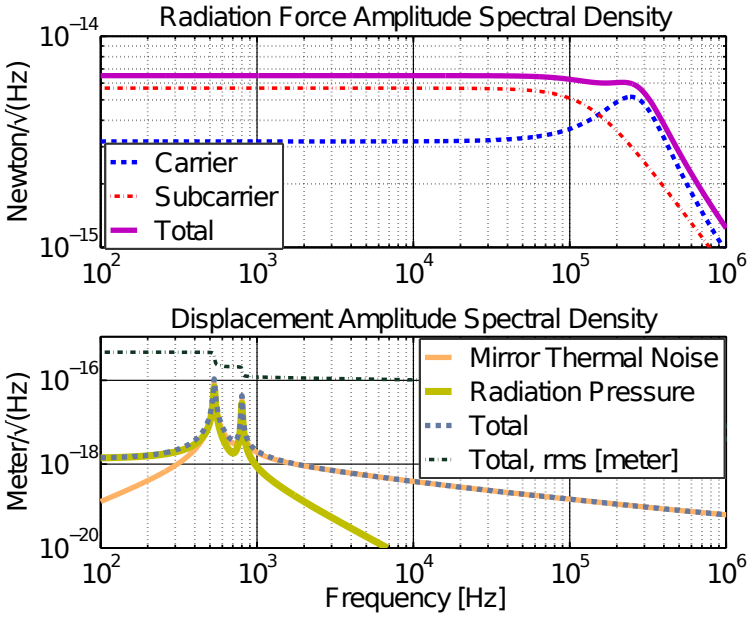

Figure 10 : (Top) Radiation force amplitude spectral density for the dual-carrier optical spring used in beam A of the above example. The subcarrier dominates the noise at low frequency, but the higher-power carrier contributes more at high frequencies. Also note that if we choose the same free spectral range for the two carriers, there would be an additional beat note at the difference frequency of 310 kHz. (Bottom) Radiation pressure and thermal noise displacement amplitude spectral density. The radiation pressure noise is calculated using the optomechanical response given in Eq. (2.27). The thermal noise is based on a theoretical calculation described in [29], [33]. Since seismic and suspension thermal noise depend on the experimental implementation, they are not shown, but they would also be suppressed by the optical spring closed loop response. The residual rms motion due to the shown noise sources is less than 10^{-3} picometers. With the total rms motion smaller than the 20 picometer stability band shown in Fig. 9, the two cavities will remain locked purely due to the radiation pressure trapping force.

to the closed loop suppression, we will have a flat displacement noise. Figure 10 (bottom) illustrates this in the case of the two-dimensional angular trap discussed above. The level of this flat displacement noise below the unity gain frequency, or optical spring resonance, is at

$$S_x(f) = \frac{S_F(f)}{K_{OS}} \tag{2.28}$$

$$\backsim \frac{\lambda}{\mathcal{F}P_0}\sqrt{2\hbar\omega P_0}. \tag{2.29}$$

where we used Eqs. (2.19) and (2.23) for the estimate, and $\mathcal{F}$ is the cavity finesse.

To compare this noise limit with existing schemes we will consider three angular control schemes: wave front sensing with a single beam (as seen in modern gravitational-wave detectors [21, 22]), two spatially separated beams with stable optical springs, and an intermediate scheme of two spatially separated beams locked with no detuning using the Pound-Drever-Hall technique [35].

First we compare the sensitivity to a cavity locked with a Pound-Drever-Hall classical feedback scheme. For the sake of this comparison we want the same dynamics, i.e. the same unity gain frequency and roughly the same loop-shape as in the optical spring system. We can however vary the input power. In addition to radiation pressure noise we now also have sensing noise. photodiode sensing is limited by photodiode quantum efficiency and other factors such as modulation depth, mode matching and overlap. Additionally, in gravitational-wave interferometers the available beam pick-off fraction for alignment sensing is tiny. All of these factors are typically less than or equal to one, which causes a relative increase in the sensing noise. However, we will not consider these effects for the moment so that we can simply illustrate our point. At best we can use all available power and only have shot noise to worry about. Then the sensing noise is given by

$$S_x \backsim \frac{\lambda}{\mathcal{F}P_0}\sqrt{2\hbar\omega P_0}. \tag{2.30}$$

We are interested in the noise in the frequency band between the mechanical resonance frequency and the unity gain frequency of the control loop. In this band the radiation pressure noise is loop-suppressed to the level of Eq. (2.28), while the displacement noise due to sensing noise is given by Eq. (2.30). At the nominal power P_0 the two schemes are the same. If we now vary P_0, we find that the displacement due to sensing

noise scales as $P_0^{-1/2}$, while the displacement due to radiation pressure noise scales as $P_0^{1/2}$ [see Eq. (2.23)]. Note that we keep the feedback gain in Eq. (2.28) equal to the unchanged reference optical spring K_{OS} in order to maintain the same unity gain frequency. We conclude that the lowest total noise, and therefore the best classical feedback scheme, can be achieved at the same power the optical spring operates. Thus the classical scheme can achieve about the same sensitivity as the optical spring system, but in practice performs worse due to real-world sensing limitations.

Finally we want to compare the displacement noise of Eqs. (2.30) and (2.28) to a wave front sensing scheme. The approximate shot noise limited sensing noise for beam angular and transverse position mismatch, S_θ and S_w, of a wave front sensing scheme is given by

$$S_\theta \backsim \frac{\theta_0}{P_0}\sqrt{2\hbar\omega P_0} \tag{2.31}$$

$$S_w \backsim \frac{w_0}{P_0}\sqrt{2\hbar\omega P_0} \tag{2.32}$$

where the divergence angle θ_0 and waist size w_0 of the resonant beam in the cavity are related to the wave length through $\theta_0 w_0 \pi = \lambda$ [36]. We can directly compare this wave front sensing scheme to Eq. (2.28) if we divide our result by the beam separation d. As long as we choose the beam separation d to be larger than spot size w, the angular sensitivity of a two-beam system such as the optical spring system is better than the wave front sensing scheme by a factor given by the cavity finesse. Intuitively this result can be understood because having two cavity resonance conditions in the two cavities restricts the angular deviations much tighter than in a one-cavity case.

2.7 Optical spring constant derivation

In this section we consider the effect of light stored in a detuned Fabry-Perot cavity using a classical approach. The intracavity power generates radiation pressure that exerts on the cavity mirror a force $F_{rad} = -K_{OS} \cdot x$, where x is the mirror displacement and K_{OS} is the optical spring constant. Here we show the full derivation of the optical spring constant K_{OS}.

We consider a suspended Fabry-Perot cavity of length L_0 with an incident beam of wavelength λ and power P_0. First we calculate a general expression of the intracavity

power and then its radiation pressure force exerted on the end mirror.

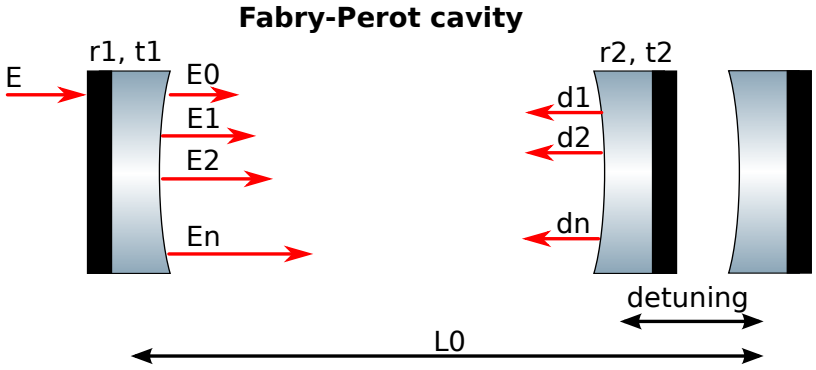

Figure 11 : A Fabry-Perot cavity of length L_0 and coefficients r_1, t_1 and r_2, t_2 for the input and end mirrors respectively. The input mirror is stationary while the end mirror is affected by harmonic motion. The incoming field E at each round-trip i adds up a phase shift due to the displacement d_i

The field $E = A_0 e^{i\omega t}$ enters the cavity (shown in Fig. 11) through the input mirror of coefficient $t_1 = t$ and r_1 and the field inside the cavity at the input mirror can be seen as the following:

$$E_{tot} = E_0 + E_1 + E_2 + E_3 + ... + En + ... \tag{2.33}$$

We consider in our model the following definitions, with d_n being the displacement of the mirror,

$$\begin{aligned} L_1 &= 2(L_0 + d_1) \\ L_2 &= 2(2L_0 + d_1 + d_2) \\ L_3 &= 2(3L_0 + d_1 + d_2 + d_3) \\ &... \end{aligned} \tag{2.34}$$

with

$$d_n = d(t - [(2n-1)\tau + \alpha_n]) \quad \text{and} \tag{2.35}$$

$$\alpha_n = 2\sum_{l=1}^{n-1} \frac{d_l}{c} - \frac{d_n}{c} \tag{2.36}$$

where $\tau = L_0/c$. With the round trip length $L = 2L_0$ and with $X = r_1 r_2 e^{-ikL}$ we obtain

$$E_{tot} = tE(1 + Xe^{-2ikd_1} + X^2 e^{-2ik(d_1+d_2)} + X^3 e^{-2ik(d_1+d_2+d_3)} \cdots).$$

Since by definition the optical spring K_{OS} is the linear term in the expansion $F = F_0 + K_{OS}d + O(d^2)$, we now expand the exponential in d_n and we group d_n terms

$$E_{tot} = \frac{tE}{1-X}(1 - 2ikd_1X - 2ikd_2X^2 - 2ikd_3X^3 + \cdots).$$

Given that any correction from α_n [Eq. (2.36)] is quadratic in $d(t)$, we can again neglect it by definition, and find for the harmonic mirror motion (i.e. in the Fourier domain)

$$\begin{aligned} d_n &= x_0 e^{i\Omega(t-(2n-1)\tau)} = x_0 e^{i\Omega t} e^{-i\Omega(2n-1)\tau} \\ &= x_0 e^{i\Omega t} \frac{Y^{2n}}{Y}\frac{Y}{Y} = Y^{2n-2} d_1 \end{aligned} \tag{2.37}$$

where $Y = e^{-i\Omega\tau}$. Thus we can write

$$E_{tot} = \frac{tE}{1-X}\left[1 - \frac{2ikd_1X}{1-Y^2X}\right] \tag{2.38}$$

where d_1 is a complex number. Since we have to take its real part $Re(d_k) = \frac{d_k + \bar{d}_k}{2}$, we consider the field inside the cavity with $\bar{d}_k$ conjugate of d_k and we obtain as total field:

$$E_{tot} = tE\left[\frac{1}{1-X} - \frac{2ikX}{2(1-X)}\left(\frac{d_1}{1-Y^2X} + \frac{\bar{d}_1}{1-\overline{Y}^2X}\right)\right].$$

Using the following expression

$$d_1 = x_0 e^{i\Omega(t-\tau)} = x_0 e^{i\Omega t} e^{-i\Omega\tau} = xY \tag{2.39}$$

we can now obtain the intracavity power expression by multiplying E_{tot} by its conjugate and considering only the linear terms of x and $\bar{x}$

$$\begin{aligned} P = & \quad E_{tot} \cdot \overline{E}_{tot} = -P_0 t^2 [\frac{ikY}{(1-\overline{X})(1-X)} \\ \times & \quad \left(\frac{X}{1-Y^2 X} - \frac{\overline{X}}{1-Y^2 \overline{X}} \right) x + const]. \end{aligned} \tag{2.40}$$

where we have also neglected the first constant term.

Once we have calculated the power we can obtain the radiation pressure force on the end mirror by $F_{rad} = \frac{2r_2^2}{c} P$. Furthermore we can also notice the similarity of the expression with the elastic force. Thus we recall that in frequency domain and complex notation K is defined by $F = -Kx$, the real form is thus

$$F' = Re[F] = -\frac{1}{2}(Kx + \overline{K}\bar{x}) = -\frac{1}{2}(Kx + const)$$

Taking into account that we are calculating the radiation pressure on the end mirror, we need to consider an extra delay factor Y for the calculation of the power which appears in the expression of K. The complex spring is then given by

$$K_{OS} = \frac{2r_2^2}{c} P_0 t^2 \frac{2ikY^2}{(1-\overline{X})(1-X)} \left(\frac{X}{1-Y^2 X} - \frac{\overline{X}}{1-Y^2 \overline{X}} \right)$$

which can be rewritten in the form of Eqs. (2.6) and (2.7).

2.7.1 Detuning

Given the frequency detuning is $\delta = \omega_0 - \omega_{res}$ and $\Omega = \omega - \omega_0$, where ω_0 is the carrier (subcarrier) frequency and $\omega_{res} = 2\pi n \cdot c/L$ is the resonant frequency, we get the following expression:

$$e^{-ikL} = e^{-i\delta 2\tau}. \tag{2.41}$$

If we now replace X and Y we obtain the exact expression for K_{OS}:

$$K_{OS} = -P_0 t^2 r_2^2 \frac{4ike^{-2i\Omega\tau}}{c(1-r_1r_2e^{i2\delta\tau})(1-r_1r_2e^{-i2\delta\tau})} \times \left(\frac{r_1r_2e^{-i\delta\tau}}{1-r_1r_2e^{-2i\Omega\tau}e^{-i2\delta\tau}} - \frac{r_1r_2e^{i2\delta\tau}}{1-r_1r_2e^{-2i\Omega\tau}e^{i2\delta\tau}} \right). \tag{2.42}$$

2.7.2 Comparison

To compare to existing literature we now expand the exponentials to linear order in Ω and δ, $e^{-i\delta 2\tau} \approx 1 - i\delta 2\tau$ and $e^{-i2\Omega\tau} \approx 1 - i2\Omega\tau$:

$$\begin{aligned} K_{OS} = & -P_0 t^2 r_2^2 \\ & \times \frac{4ik(1-2i\Omega\tau)r_1r_2}{c(1-r_1r_2+r_1r_2i2\delta\tau)(1-r_1r_2-r_1r_2i2\delta\tau)} \\ & \times \left[\frac{1-i2\delta\tau}{1-r_1r_2(1-2i\Omega\tau-i2\delta\tau)} - \frac{1+i2\delta\tau}{1-r_1r_2(1-2i\Omega\tau+i2\delta\tau)} \right]. \end{aligned}$$

We further simplify this equation using expressions for the $Finesse \approx \pi \frac{r_1r_2}{1-r_1r_2} = \pi FSR/\gamma$ and the free spectral range $FSR = 1/2\tau$, introducing the cavity bandwidth γ. We also neglect the $i\Omega\tau$, $i\delta\tau$ terms in the numerator since they correspond to a simple time delay. We obtain:

$$K_{OS} \approx P_0 t^2 r_2^2 \frac{8kr_1r_2}{c(1-r_1r_2)^3} \frac{\frac{\delta}{\gamma}}{(1+\frac{\delta^2}{\gamma^2})} \left[\frac{1}{1+\frac{\delta^2}{\gamma^2}-\frac{\Omega^2}{\gamma^2}+i2\frac{\Omega}{\gamma}} \right] \tag{2.43}$$

which is equivalent to the expression already existing in the literature [32, 18].

2.7.3 Overcoupled cavity

In the particular case of perfectly overcoupled cavity ($r_2 = 1$) $Finesse/\pi = 2/T_1$ and $(1-r_1r_2)^2 = T_1^2/2$ and the optical spring constant becomes

$$K_{OS} \approx 128P_0 \frac{\pi}{c\lambda T_1^2} \frac{\frac{\delta}{\gamma}}{(1+\frac{\delta^2}{\gamma^2})} \left[\frac{1}{1+\frac{\delta^2}{\gamma^2}-\frac{\Omega^2}{\gamma^2}+i2\frac{\Omega}{\gamma}} \right]. \tag{2.44}$$

2.7.4 Matched cavity

In this case of a matched cavity ($r_1 = r_2$) $Finesse/\pi = 1/T_1$ and $(1-r_1 r_2)^2 = T_1^2$ and the optical spring constant remains the same as in Eq. (2.44) except for the factor 128 which has to be replaced with 16.

2.8 Torsion pendulum mechanical plant

Here we transform the basis of coordinates $\{x_G, \Theta\}$ formed by the position of the center of gravity x_G of the mirror and its rotation angle Θ with respect to the vertical axis passing from x_G into a basis $\{x_A, x_B\}$ formed by the length of the cavities relative to beam A and beam B respectively. Thus the longitudinal and angular control of the mirror can be treated as the longitudinal control of the two above mentioned cavities. The basis can be expressed as

$$\begin{pmatrix} x_A \\ x_B \end{pmatrix} = \begin{pmatrix} 1 & r_A \\ 1 & r_B \end{pmatrix} \begin{pmatrix} x_G \\ \Theta \end{pmatrix} = \mathcal{B} \begin{pmatrix} x_G \\ \Theta \end{pmatrix} \tag{2.45}$$

where r_A and r_B are the lever arms of the two beams with respect to x_G.

The equation of motion for the mirror is

$$-\omega^2 \begin{pmatrix} m & 0 \\ 0 & I \end{pmatrix} \begin{pmatrix} x_G \\ \Theta \end{pmatrix} = \begin{pmatrix} F_{tot} \\ T_{tot} \end{pmatrix} \tag{2.46}$$

where I is the moment of inertia of the mirror of mass m. We now express the total force and the total torque exerted on the mirror as function of the individual forces F_A and F_B:

$$\begin{pmatrix} F_{tot} \\ T_{tot} \end{pmatrix} = \begin{pmatrix} 1 & 1 \\ r_A & r_B \end{pmatrix} \begin{pmatrix} F_A \\ F_B \end{pmatrix} = \mathcal{B}^T \begin{pmatrix} F_A \\ F_B \end{pmatrix}. \tag{2.47}$$

Using Eqs. (2.47) and (2.45) in Eq. (2.46) we obtain the equation of motion in the x_A, x_B basis:

$$-\omega^2 \left[\mathcal{B}^{T-1} \begin{pmatrix} m & 0 \\ 0 & I \end{pmatrix} \mathcal{B}^{-1} \right] \begin{pmatrix} x_A \\ x_B \end{pmatrix} = \begin{pmatrix} F_A \\ F_B \end{pmatrix}. \tag{2.48}$$

2.9 Stability in two dimensions

The control loop stability in multiple dimensions can be evaluated by considering the one-dimensional open-loop transfer function of every control filter (i.e. optical spring) while all other loops stay closed. Here we calculate these open-loop transfer functions for the two-dimensional case.

Referring to Fig. 7, we inject a signal $F_{\rm ext}$ into the path of beam A. The output of path A is F_A. Simultaneously we close the control loop relative to beam B by feeding back the force F_B, which represents the output of path B.

We obtain the following expression:

$$HM \begin{pmatrix} 0 \\ -F_B \end{pmatrix} + HM \begin{pmatrix} F_{ext} \\ 0 \end{pmatrix} = \begin{pmatrix} F_A \\ F_B \end{pmatrix}. \tag{2.49}$$

If we introduce the 2×2 matrix S,

$$S_A = \begin{pmatrix} 0 & 0 \\ 0 & 1 \end{pmatrix} \tag{2.50}$$

we can write

$$HMS_A \begin{pmatrix} -F_A \\ -F_B \end{pmatrix} + HM \begin{pmatrix} F_{ext} \\ 0 \end{pmatrix} = \begin{pmatrix} F_A \\ F_B \end{pmatrix}. \tag{2.51}$$

Using the vector $e_A^T = (1, 0)$ we are able to extract the following open loop transfer function related to cavity A:

$$OL_A = \frac{F_A}{F_{ext}} = e_A^T (\mathbb{1} + HMS_A)^{-1} HMe_A. \tag{2.52}$$

The same open loop transfer function can be obtained considering an external signal injected into the loop of the beam B while the loop of beam A remains closed,

$$OL_B = \frac{F_B}{F_{ext}} = e_B^T (\mathbb{1} + HMS_B)^{-1} HMe_B \tag{2.53}$$

with $e_B^T = (0, 1)$ and

$$S_B = \begin{pmatrix} 1 & 0 \\ 0 & 0 \end{pmatrix}. \tag{2.54}$$

2.10 Conclusions

In conclusion, we investigated the use of the radiation pressure of laser light as an alternative to a conventional feedback system for controlling the longitudinal and angular degrees of freedom of a mirror. The method is based on a double dual-carrier scheme, using a total of four detuned laser fields in two cavities. The two dual-carrier beams hit the mirror in separate spots, forming two stable optical springs. This constrains both the longitudinal and the angular degrees of freedom of the mirror, replacing completely the commonly used electronic feedback system. We showed that this setup allows a stable control of the two degrees of freedom, within a displacement range of the test mirror of $\sim 20\,\mathrm{pm}$. This promising idea can be extended to the other angular degree of freedom. We found that such a method creates an angular optical spring stronger than the angular Sidles-Sigg instability, which drives the requirement for angular control in the high power arm cavities of gravitational-wave detectors. We also showed that the fundamental limit of this scheme is the quantum radiation pressure noise, resulting in a reduction in control noise compared to a conventional active feedback approach. We are working towards the experimental demonstration of this effect for a gram-scale mirror and beginning to explore its extension to large-scale gravitational-wave detectors.

Chapter 3

Suspensions

In this set of experiments, we are required to suspend optics to reduce the effects of seismic motion on the mirrors to acceptable levels. We also use suspensions because they recreate angular suspension modes similar to that of the LIGO detectors, allowing us to study the Sidles-Sigg instability. However, suspending the optics is one of the most complicated and delicate aspects of the experiment. The optics are constructed as discs with roughly 76 mm (3 inch) diameters. They are suspended from modified Small Optics Suspensions (SOSs) and controlled with Optical Sensing Electro-Magnets (OSEMs), both originally developed for the initial LIGO detectors.

3.1 Input coupler

The input coupler (see fig 12) is designed to hold three mirrors at specific positions and angles. The mirrors are 0.5 inches in diameter with 7.5 cm radius of curvature (RoC). They are mounted in an approximately 300 gram aluminum disk. The central mirror forms the straight cavity with the end mirror, while the two mirrors on the side are part of the folded cavity. The angle and, to a lesser degree, z position of the two side mirrors are adjustable using set screws.

For each of the adjustable mirrors, set screws push on the bevel of the back surface of the mirror. The mirror is held in place by a Teflon tube placed on the front side of the mirror, which is in turn clamped down with springs on screws. This gives us the flexibility to adjust for manufacturing defects and to adjust the beam separation on the end mirror after construction.

Tapped screws in the top and bottom allow for precision correction of the center of mass of the mass after suspension. In designing the input coupler, we had to shift the mirror mounts laterally about 0.2 inches away from the optical axis to center the mirrors in the disk.

The placement of the mirrors inside the input coupler was determined using the calculated separation of the beams, the angle of the folded cavity, and the desired lengths of the two cavities.

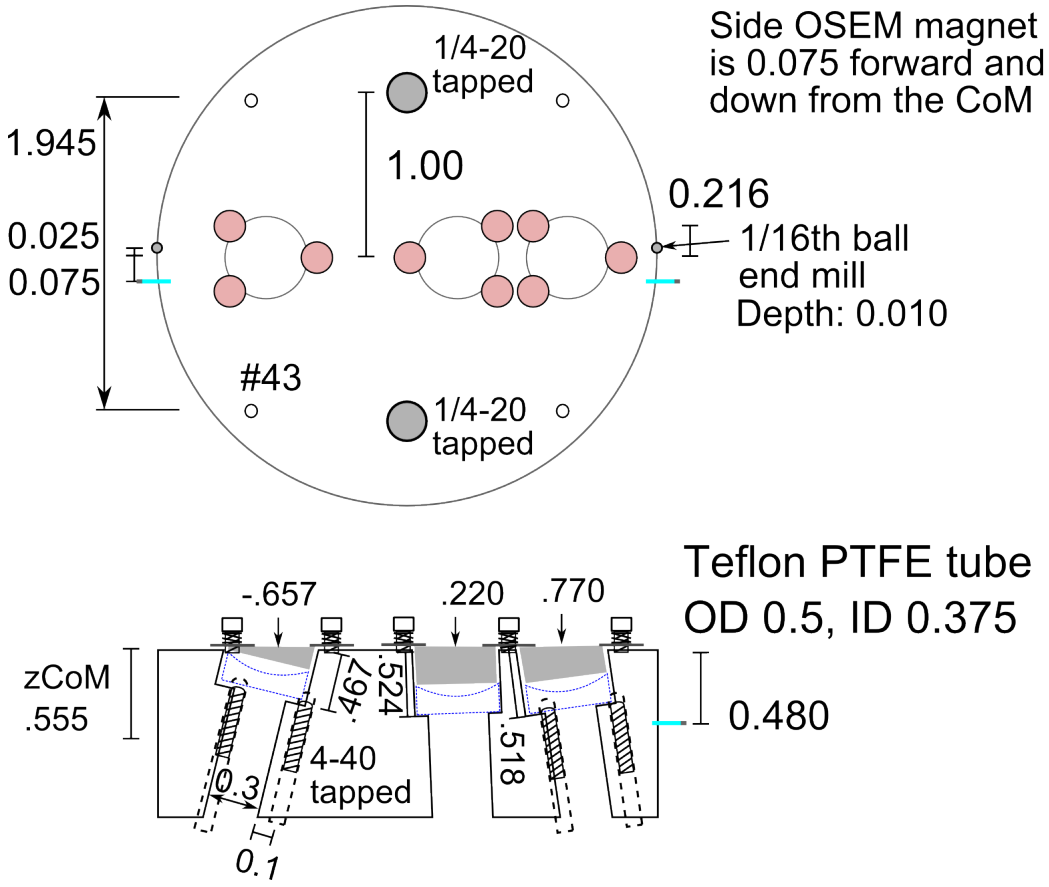

Figure 12 : The input coupler for the cavity. Three 0.5 inch diameter mirrors with 7.5 cm RoC are held at specific angles inside an aluminum disk. The two side mirrors are adjustable using set screws, while the central mirror is fixed. All of the mirrors have been shifted 0.2 inches in the positive direction to center them in the disk.

3.2 End mirror

The end mirror has a diameter of 0.305 inches, a radius of curvature of 5 cm, and a mass of 0.4 grams. It is suspended by glass fibers from a steel ring, which is in turn suspended from a modified SOS. The schematic of the suspension is shown in figure 13 and an older version of the suspension is pictured in figure 33.

The fibers are manufactured by cold welding a fused silica rod onto a mirror blank, creating a nub, then pulling a fiber off it, to a length of about 1 inch. Once the fiber cools, we break the cold weld. This leaves us with a nub attached to a fiber, which is in turn attached to a silica rod. The silica rod is glued into an aluminum block, which is screwed down to the steel ring. The nubs are then glued to the actual mirror using Optocast 3553. Because the nubs were created on a mirror blank with the same diameter, the volume of glue required is minimized, reducing the thermal noise effects of the glue joint. After gluing on all three fibers, the fibers are tensioned to raise the resonance of the position mode to the desired frequency.

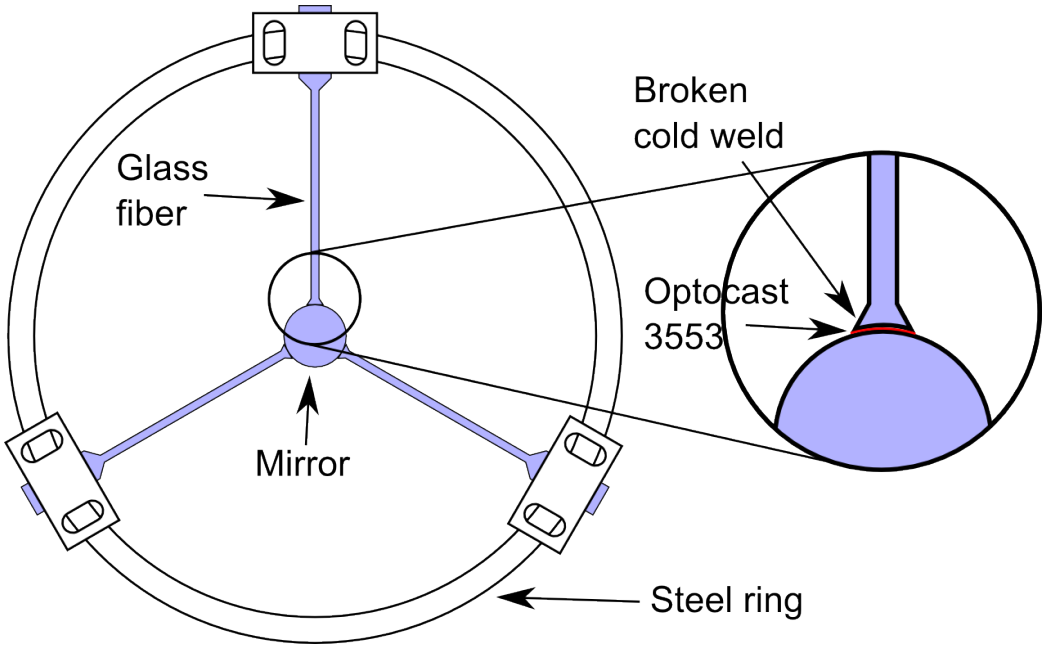

Figure 13 : End mass suspension. A 0.4 gram mirror is suspended from a steel ring using glass fibers. The nubs at the end of the fibers are glued onto the mirror using Optocast 3553. The rods on the other side of the fiber are glued into aluminum blocks which are tensioned then screwed down to the ring.

3.3 Blade Springs

This is a discussion of the relevant physics to the construction of blade spring suspensions for a small optics suspension. The theoretical parts of this discussion are based primarily on the notes posted by Justin Greenhalgh on the LIGO Document Control Center (DCC) [37].

3.3.1 A little theory

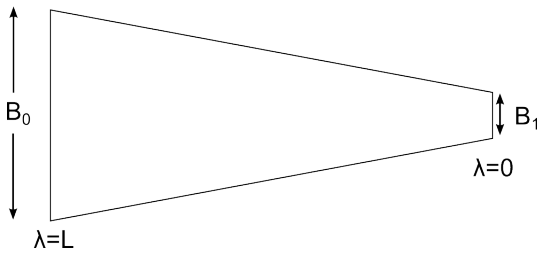

Figure 14 : Illustration of the basic layout of a blade spring. L is the length of the blade, B_0 is the large base and B_1 is the small base. λ is the distance along the blade.

The behavior of blade springs can be modeled by looking at the behavior of cantilevered beams. Greenhalgh gives the general formula for an elastic beam under a load (see e.g. [38], eq. 8.1-4):

$$\frac{E}{R(\lambda)} = \frac{M(\lambda)}{I(\lambda)}. \tag{3.1}$$

Here λ is the distance along the blade (with the $\lambda = 0$ at the tip), E is the Young's modulus, R is the radius of curvature at λ, I is the area moment of inertia at λ, and M is the bending moment at λ, expressed as

$$M = mg\lambda \tag{3.2}$$

where m is mass supported, g is 9.81 m/s^2.

$b = B_1 + (B_0 - B_1)\frac{\lambda}{L}$ is the width between $\lambda = 0$ ($b = B_1$) and $\lambda = L$ ($b = B_0$) (see figure 14) so

$$I = \frac{bt^3}{12} = (b_0 - b_1)\frac{t^3}{12}\frac{\lambda}{L} + b_1\frac{t^3}{12} \tag{3.3}$$

where t is the thickness of the blade and L is the blade length. If we consider the blade to be triangular ($b_1 = 0$), I becomes

$$I = \frac{B_0 t^3}{12}\frac{\lambda}{L}. \tag{3.4}$$

Then we see that

$$\frac{E}{R(\lambda)} = \frac{M(\lambda)}{I(\lambda)} = \frac{mg\lambda}{B_0\frac{t^3}{12}\frac{\lambda}{L}} = \frac{12mgL}{B_0 t^3} \quad \rightarrow \quad R = constant. \tag{3.5}$$

In other words, R is constant along the blade (the blade profile is circular). We can accomplish this behavior by specifying that the wire is clamped where the end of the 'triangle' should be.

Thus we can, without difficulty, treat a change in force on the spring (for instance by changing the mass) as a change in the radius of curvature of the blade.

From Eq. (3.5) we obtain R

$$R(\lambda) = R = \frac{EB_0 t^3}{12mgL}. \tag{3.6}$$

We can determine the effective spring constant k based on the vertical displacement D of the end of the spring and Hooke's law.

$$D = R(1 - \mathrm{Cos}(\frac{L}{R})) \approx \frac{L^2}{2R} = \frac{mg}{k} \tag{3.7}$$

From Eqs. (3.6 and 3.7) we can obtain the bounce mode frequency f_b

$$f_b = \frac{1}{2\pi}\sqrt{\frac{k}{m}} = \frac{1}{2\pi}\sqrt{\frac{EB_0 t^3}{6mL^3}} \tag{3.8}$$

and the maximum stress in the blade as:

$$\sigma = \frac{Mt}{2I} = \frac{6mgL}{B_0 t^2}. \tag{3.9}$$

We can use Eq. (3.9), solved for B_0, to simplify Eq. (3.8), thus

$$f_b = \frac{1}{2\pi}\sqrt{\frac{Egt}{L^2\sigma}}. \tag{3.10}$$

Given a target stress σ, a target bounce frequency f_b, and a length limit L based on the chamber dimensions, we can determine the proper thickness t for the blade.

If we manipulate equations 3.10 and 3.9, we get

$$t = \frac{(2pi f_b L)^2\sigma}{Eg} = \sqrt{\frac{6mgL}{B_0\sigma}}. \tag{3.11}$$

This equation gives the minimum thickness requirement for a blade spring.

3.3.2 Materials

During the course of designing and constructing blade spring suspensions, we considered several different sizes, locations, and overall suspended masses. We finally decided on the small blade springs currently in use. It is however still useful for comprehensiveness to review other options that would be better for larger blade springs to support more massive loads.

For large blade springs, the LIGO-recommended material is "maraging" steel (sometimes known by the tradename Vascomax), which is easy to machine, but becomes very hard when baked. One drawback of this material is that it can corrode over time. To combat this, LIGO recommends putting a nickel plating on the blades [39]. The hardness of the final product is the primary reason it is used. This material is difficult and expensive (best offer was $1200 for six blade's worth) to buy in small quantities.

As an alternative, we considered "full hardened" 301 stainless steel. It is a factor of about 2.5 weaker than the maraging steel, but we have have found that workable solutions exist. This would not need any special baking, but is more difficult to machine.

A third alternative is 17-4 precipitation hardened (PH) stainless. This material is similar to maraging steel in that it becomes harder when you bake it. Baking at 900 F for one hour results in a yield strength of 200000 psi = 1379 MPa. Baking longer

or at a higher temperature makes the yield strength drop a bit, but this behavior is understood and fairly error-tolerant [1].

One more alternative, which LIGO uses for the small blade springs, is 304 stainless (yield strength of 200 MPa) because the expected strain in the small blades is about 80 MPa. We ended up using this because of high availability and very good vacuum compatibility.

For comparison, McMaster has details of many of the metals that are available [2]. All of the metals we considered are on the LIGO vacuum compatible materials list [40], though not all are recommended for unrestricted use.

When we are determining the maximum amount of stress that the blade can withstand before deforming, we typically use the yield strength. This is the amount of stress that causes the metal to deform by 0.2%. We have chosen as a target strain 60% of the yield strength.

One LIGO document [41] uses a modified Young's modulus

$$E_{eff} = \frac{E}{1-\mu^2} \tag{3.12}$$

which includes a factor with Poisson's ratio, μ, effectively increasing the strain. This is attributed to a change in the strain of the material due to bending. Our predictions seem to work better with this factor removed, but we have chosen to keep the factor for estimations because it represents the 'worst case' scenario.

Steel	E (GPa)	E (psi)	σ_{max} (MPa)	σ_{max} (PSI)
C350 Maraging	200	29×10^6	2344	34×10^4
301 Stainless	193	28×10^6	965	14×10^4
17-4 PH Stainless	196.5	28.5×10^6	1379	20×10^4
304 Stainless	193	28×10^6	207	3×10^4

Table 1 : Characteristics of proposed materials. We chose 304 Stainless because it is easy to work with, easy to put in vacuum, and the maximum stress expected was more than a factor of two less than σ_{max}.

[1] http://www.aksteel.com/pdf/markets_products/stainless/precipitation/17-4_PH_Data_Bulletin.pdf

[2] http://www.mcmaster.com/library/20121105/8984KAC.pdf

3.3.3 Blade spring design

To design and build useful blade springs, we must satisfy the following criteria:

1. Maintain safe levels $\leq 80\%$ of material stress limits: $\sigma \leq 0.8\sigma_{max}$.
2. Blades must be mounted on top of the existing suspensions; smaller is better.
3. Choose a 'small' (within reason) bounce mode frequency (This determines t).
4. Effective adjustment of the suspended mass height and roll once suspended.

3.3.4 Small blade

We decided to build a small blade suspension system, mounting the blades to the top of a modified SOS and hanging the optics from the blades using tungsten wire.

For the small spring system, our design is very similar to the parameters used in the HAM AUX design for aLIGO [42]. We could use 304 Stainless or 17-4 Stainless with little impact on the final performance. However, the maximum stress of this design is only 40% of the expected yield strength of 304 and much less than that for 17-4, so using 304 gives us more leeway with the construction and reduces the chance of failure due to improper baking. The final design schematic is shown in figure 15.

We have included angular adjustment of the blade mounts to allow for small corrections to the suspended mass height and roll.

The final design had a resonant frequency of about 7 Hz and provided effective $1/f^2$ damping above that frequency.

3.3.5 Coupling

For the small spring system, we do not need to worry about mass height to cavity length coupling because changes in height will cause opposite lateral forces on the suspended optic, which should cancel out. There are no foreseeable first order couplings between height and cavity length.

3.4 OSEM diagonalzation

To control the mass under vacuum, we use devices called OSEMs (Optical Sensing Electro-Magnets). These are devices (see fig. 16) that sense the position of an optic

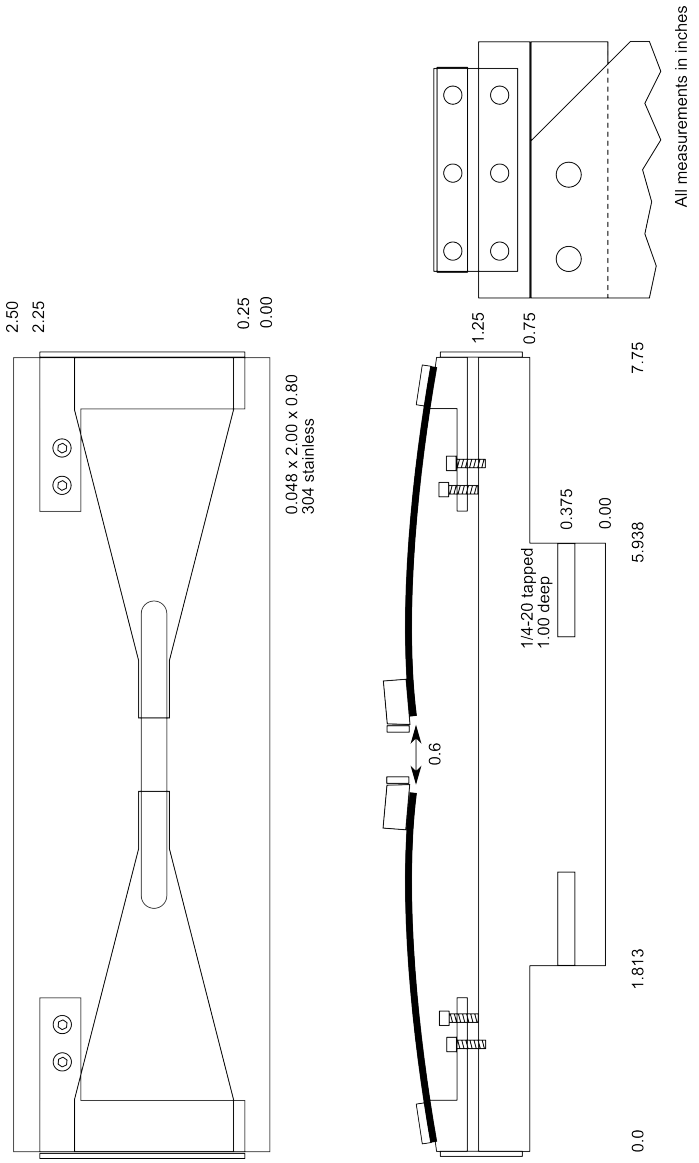

Figure 15 : Drawings for the small blade suspension modification to the SOS. The blade angle can be adjusted using the screws. This adjustment was used for fine adjustment of the optic height and rotation.

Parameter	**Metric**	**Imperial**
Blade length, L	7.68 cm	3.0 in
Blade base width, B_0	3.3 cm	1.3 in
Blade thickness, t	0.51 mm	0.020 in
Mounting angle, θ	0.083 rad	4.78°
Supported mass, m	0.15 kg	0.33 lbs
Result	**Metric**	**Imperial**
Bounce Frequency, f_b	7.19 Hz	
Max height	2 mm	0.08 in
Tip height	2 mm	0.06 in
Effective length	7.7 cm	3.0 in
Maximum Stress, σ	81 MPa	11700 PSI

Table 2 : Characteristics of the final blade design. Upon testing, the frequency for a 155 g test mass gave a resonant frequency of $7.3 \pm .1$ Hz.

using magnets which are mounted on the optic. The magnet partially blocks light from an LED, so when it moves it causes changes in the voltage out from a photodiode. This signal is sent to the digital system, where it is converted into position, pitch, yaw, and side motion. Each of these degrees of freedom have specific filters applied to them, then the signals are converted back into the five sensor distances. Coils in the OSEM are driven accordingy, controlling the motion of the optic.

The hardest part to get right when using OSEMs is to properly diagonalize them so that you can push in the standard degrees of freedom (i.e. position, pitch, yaw, and side). This is accomplished in two steps, along with some sneaky meter-to-radian conversion.

First, we diagonalize the input matrix. An ideal input matrix should look like table 3. The input values are converted to micrometers before they get to this matrix. This matrix then converts the measurements to position and side measurements in μm and pitch and yaw measurements in μrad (the angular conversion is dependent on the fact that the magnets are mounted in a 4.94 by 4.94 cm square). Thus a change of $1\,\mu$m the upper left (UL) sensor is counted as : $.25\,\mu$m position, $-10.1\,\mu$rad in pitch, $10.1\,\mu$rad in yaw, and no change in side.

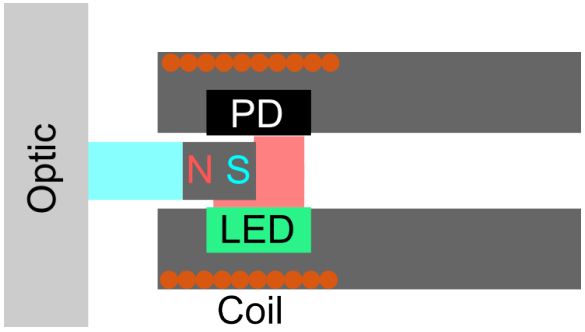

Figure 16 : Layout of an Optical Sensing Electro-Magnet (OSEM). Optic motion is sensed when the magnet changes the amount of light from the light emitting diode (LED) that gets to the photodiode (PD). The coils can be driven to move the magnet and thus the optic.

UL	**UR**	**LR**	**LL**	**SD**	
.25	.25	.25	.25	0	position (μm)
-10.1	-10.1	10.1	10.1	0	pitch (μrad)
10.1	-10.1	-10.1	10.1	0	yaw (μrad)
0	0	0	0	1	side (μm)

Table 3 : Ideal input matrix. The sensor inputs (in μm) are multiplied by the coefficients to get position of the mass in two directions (position and side) and the orientation of the mass (pitch and side). The coefficient for the angular measurements is calculated from the distance (1.945 in) between the magnets mounted on the mass.

However, due to OSEM alignment, machining defects, suspension inaccuracy, etc. the ideal matrix is not the most effective. Thus, we have a method for diagonalizing the matrices.

We drive one OSEM and look at the transfer function between that and all of the other OSEMs. We can determine from this the different modes (pos, pit, and yaw) by looking at the phase differences between the four back OSEMs (UL UR LL LR) at resonances. After this, we orthogonalize based on the coupling of each mode to the five osems. Here we have one interesting note: the position mode that we see is actually the pendulum mode, which is a combination of the pitch and position modes of the mass. The coupling scales inversely with the pendulum length.

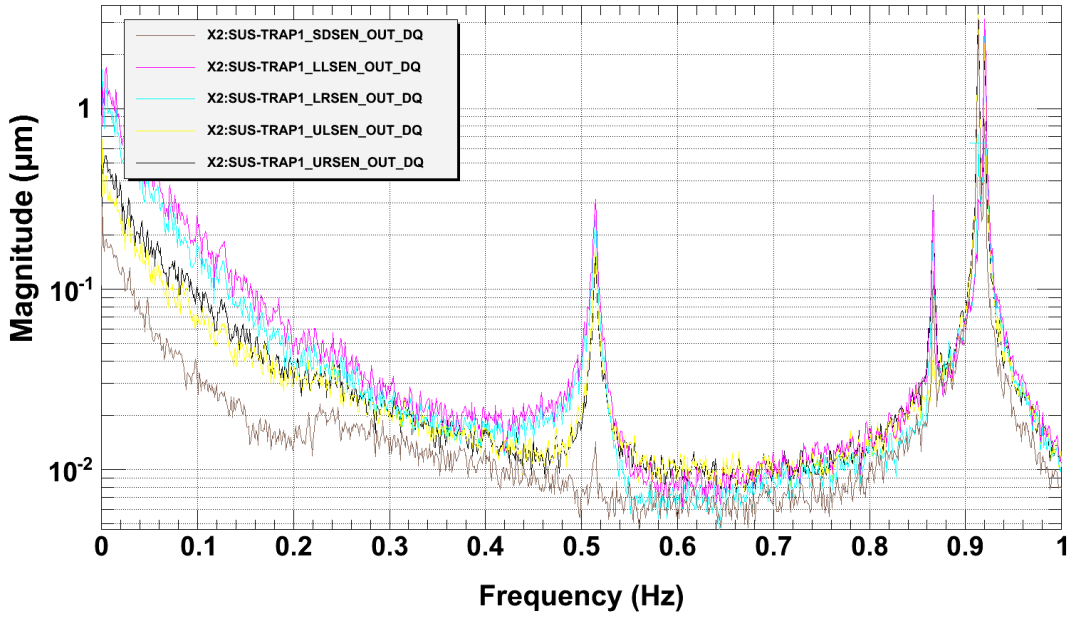

Figure 17 : Spectrum showing the modes of the input coupler. Modes from low to high are: Pitch (0.511 Hz), Yaw (0.866 Hz), Side (0.911 Hz), and Position (0.918 Hz).

Once we have the input matrix set, we diagonalize the output matrix. We close the loops and drive each degree of freedom with a slow signal, then measure the responses in each of the (properly diagonalized) sensors. We subtract out the drive to the not desired degrees of freedom to determine the output matrix.

Chapter 4

Control Loops

There are several control systems of note in an optical trapping setup. The subcarrier servo controls the accousto-optic modulators (AOMs) which take light from the carrier and frequency shift it to create the subcarrier. The trap cavity control servo and digital system are responsible for locking the cavity and reading out the cavity transfer function.

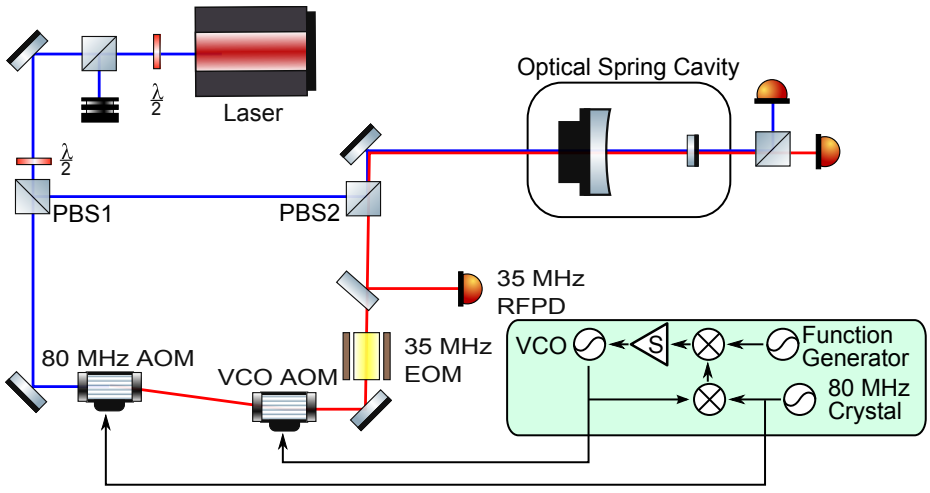

Figure 18 : There are two main control loops in an optical spring system. The first is the subcarrier servo, (green box, lower right) which detunes the subcarrier a set frequency from the carrier. The second controls the laser frequency and the trap cavity input coupler to lock the cavity.

4.1 Subcarrier Servo

The goal of the subcarrier servo is to red detune the subcarrier beam a set frequency away from the carrier beam. The required frequency shift is roughly twice the cavity pole frequency. With the parameters of our experiment, our cavity pole frequency was about 140 kHz, and thus our required detuning was about 300 kHz. There are no easily available AOMs that work in that frequency range. Previous experiments [18] have overcome this by shifting an entire FSR plus the desired detuning, but the FSR of our cavity is about 2 GHz, which is above the range of standard AOMs.

Thus we chose a difference frequency scheme with two AOMs frequency shifting in opposite directions to achieve small offset (200kHz) within a single FSR. This system is controlled by the subcarrier servo, which is designed to lock a VCO (voltage controlled oscillator) a set frequency away from a crystal oscillator. The is accomplished through two mixers and some feedback, as shown in figure 19.

We use directional couplers to get low-power signals from both the 80 MHz crystal oscillator and the VCO so that the majority of the power is driving the AOMs, maximizing the optical power going into the first order mode. The signal from the oscillator is mixed with the output of the VCO to produce a signal where the frequency is the difference between the two signals. This signal is then mixed with the desired offset frequency, set on the function generator, to give a low frequency error signal. The error signal is passed through some filters in the servo, then fed into the VCO frequency modulation input.

We typically monitor two spots in this system: The output of the fast mixer (ZMY-3) and the drive signal from the function generator (200 kHz on the diagram). When locked, the two should have the same frequency and be phase locked. The unity gain frequency of the locked system is about 2 kHz. below that, the servo should suppress frequency noise in the AOM drive (though it will not help for sensing noise).

4.1.1 Measuring frequency noise

We are going to look at the spectrum of the oscillators near 80 MHz to figure out the amount of frequency noise from these oscillators. We're mostly concerned with the frequency noise in the 1 kHz band around the peak.

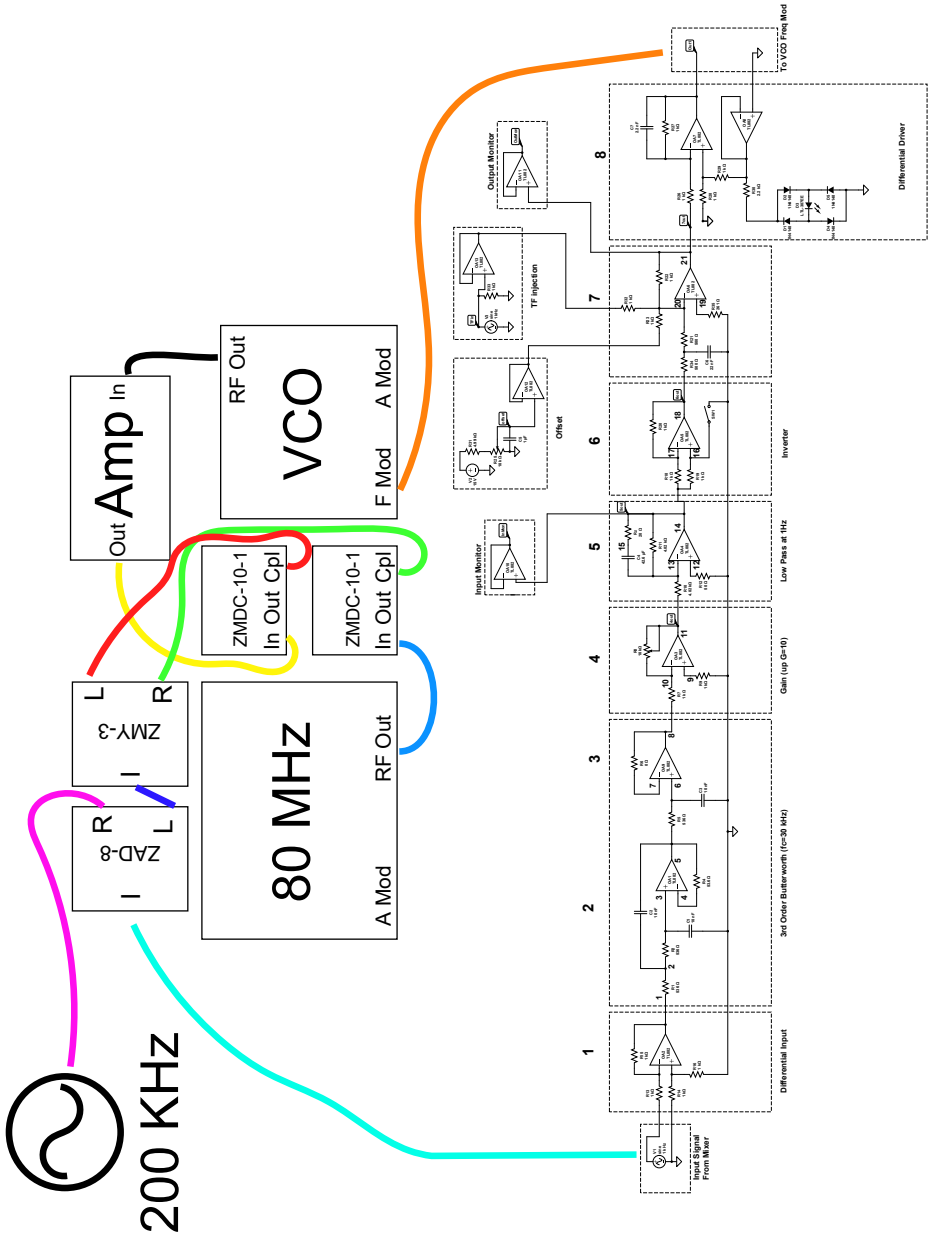

Figure 19 : Subcarrier Servo diagram. The servo locks the VCO output to the 80 MHz oscillator output, offset by the function generator. The VCO and 80 MHz output signals are taken from the directional couplers (ZMDC-10-1), which output a majority of the power through the "Out" terminal to the AOMs. Those signals are fed through a mixer (ZMY-3), then the output is mixed again (ZAD-8) with the function generator (200 kHz). The function generator can be tuned from roughly 50 kHz to 2 MHz.

We begin by assuming that all voltage noise is phase noise (no change in the amplitude). This method gives an upper limit to the noise in the system.

In the following discussion, ω_m is a measurement frequency and ω_c is the carrier frequency.

We expect the voltage output to be $V(t) = V_0 e^{i(\omega_c t + \phi(t))}$, where $\phi(t)$ is the noise in the system.

In the frequency domain,

$$\delta V(\omega_m) = V_0 \delta\phi(\omega_m) = \frac{2\pi V_0}{\omega_m} \delta f(\omega_m). \tag{4.1}$$

It is important to note that we need to sum the effects of the noise at the carrier plus 1 kHz and the carrier minus 1 kHz to get the total frequency noise.

$$\delta f(\omega_m) = \frac{\omega_m \delta V(\omega_m)}{2\pi V_0}. \tag{4.2}$$

We can now calculate the effect of this frequency noise on our optical trap cavity length δx. f_L is the laser frequency.

$$\delta x = \frac{L}{f_L} \delta f = 2.66 \times 10^{-16} \delta f. \tag{4.3}$$

4.1.2 Results

With the subcarrier servo locked at approximately 200 kHz, the noises we measure are:

80 MHz Oscillator: frequency noise $5.4 \times 10^{-3} \frac{\text{Hz}}{\sqrt{\text{Hz}}}$. Position noise $1.4 \times 10^{-18} \frac{\text{m}}{\sqrt{\text{Hz}}}$.

VCO: frequency noise $6.7 \times 10^{-2} \frac{\text{Hz}}{\sqrt{\text{Hz}}}$. Position noise $1.7 \times 10^{-17} \frac{\text{m}}{\sqrt{\text{Hz}}}$.

Both of these values are below the expectation of laser frequency noise at 1 kHz (about $2 \times 10^{-15} \frac{\text{m}}{\sqrt{\text{Hz}}}$) , so that should be acceptable.

4.2 Cavity control loops

Here's a picture of the longitudinal trap as it stands. In general terms, we have a cavity with position and laser feedback, which also has optical spring behavior. Analog and digital loops are shown in figures 22 and 23.

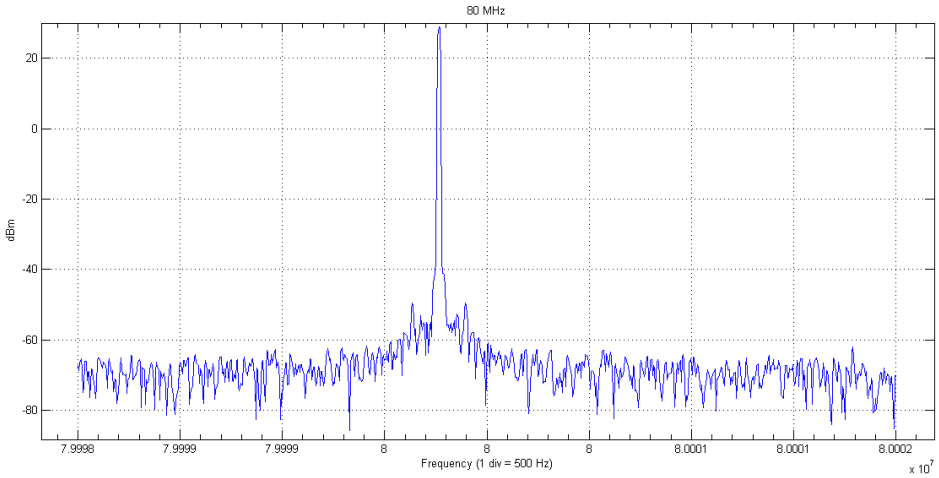

Figure 20 : Spectrum of the 80 MHz crystal oscillator around 80 MHz.

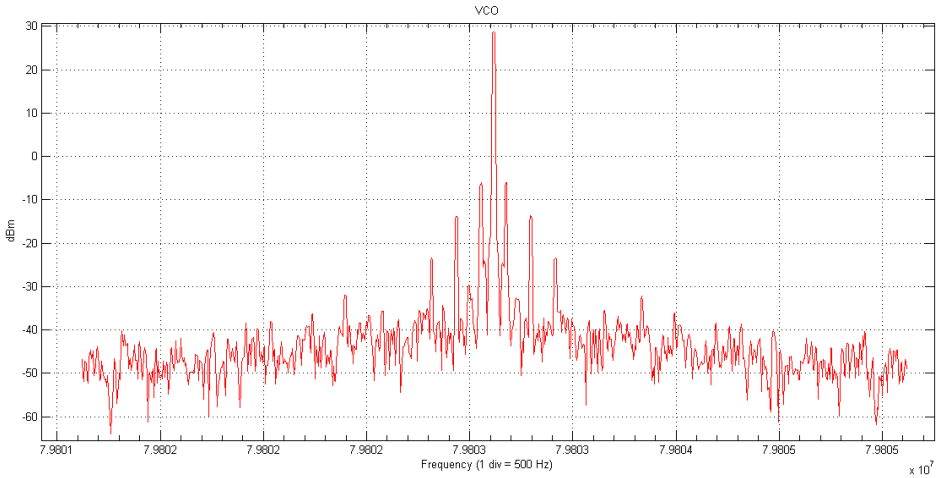

Figure 21 : Spectrum of the locked VCO. The sidebands are likely caused by the function generator.

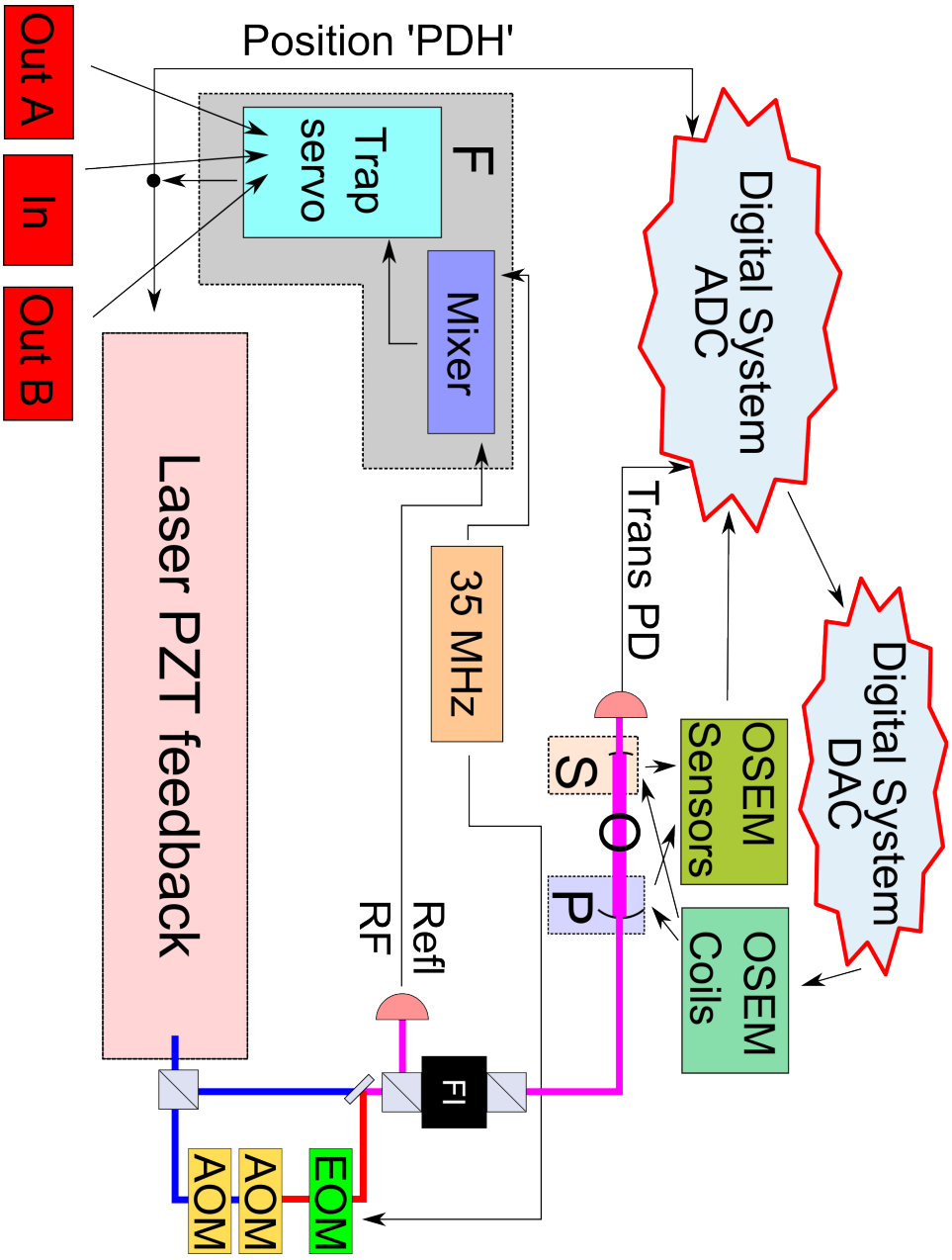

Figure 22 : Analog parts of the locking loop. We lock the cavity (OS) using the PDH signal from the reflected RF photodiode (Refl RF). The feedback signal goes to the laser PZT for fast feedback and to the digital system for slow feedback to the OSEMs. We measure the open loop transfer function of the system by driving the "In" port, then measuring "OutA" divided by "OutB".

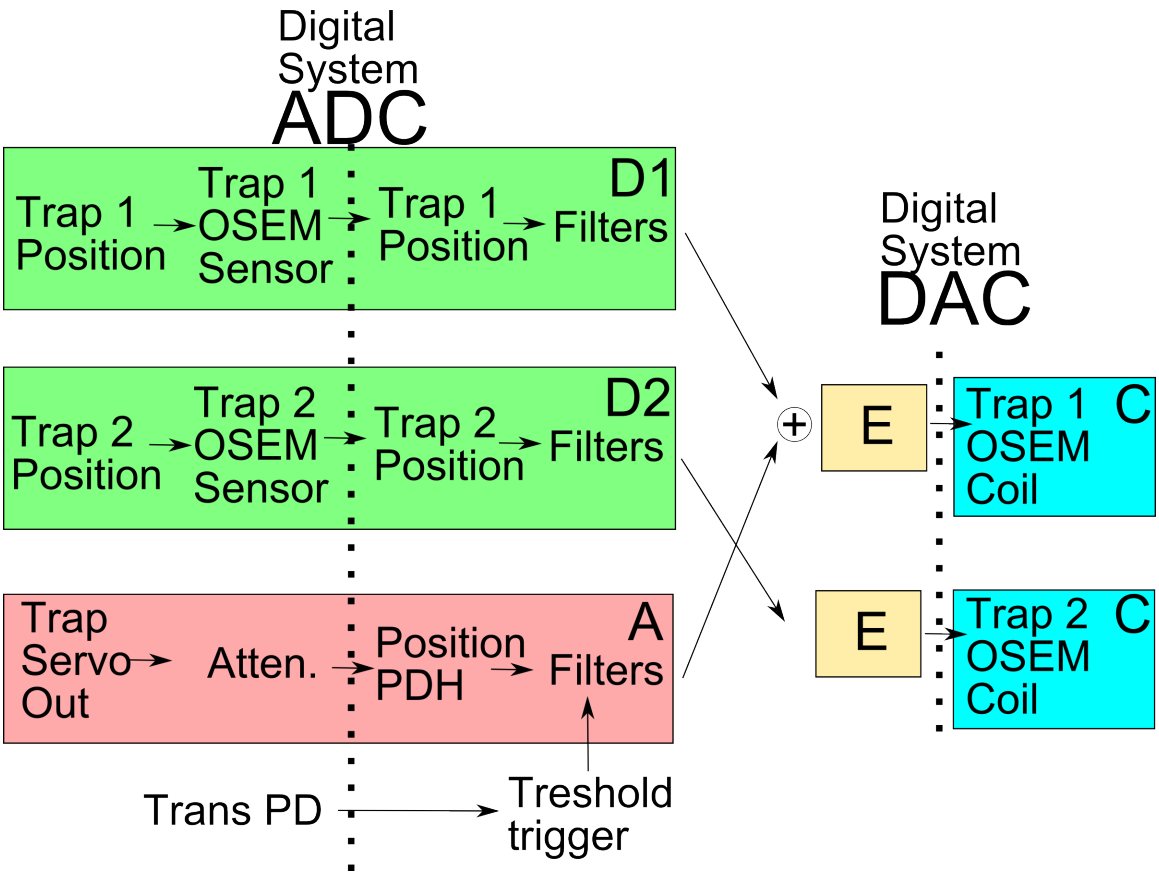

Figure 23 : Digital parts of the locking loop. These parts are responsible for the slow feedback to the OSEM coils. The yaw and optical lever inputs are not relevant to the longitudinal trap.

Each component has a letter associated with it, which represents the transfer function of the associated element. Each of the following sections describes an element and how it is calculated. I am leaving out the input whitening on the analog side and the dewhitening on digital side. They should cancel out every time, so we just leave them off.

Our goal is to be able to reconstruct the entire optical trap from the control point to the error signal. In our measurements, we are using the injection input and the two test outputs of the Trap Servo board. Test out A serves as our error signal (OUT) and Test out B serves as our control signal (IN). The injection happens between the two test outputs. The resulting open loop transfer function is plotted in figure 31. This is based on James Lough's [43] model of the loop, which I have updated and repackaged.

$$\frac{OutA}{OutB} = \left[FHLM + \frac{FAECP + FTCP}{1 + PCED}\right] \frac{1}{1 + SO}. \tag{4.4}$$

There are several different parts to this equation, so we will take a moment to look at each term. Every term in the numerator includes F, the Trap Servo. $FHLM$ is a loop involving the PZT drive of the laser. $FAECP$ and $FTCP$ both rely on pushing the large mass around using the OSEM drive, but $FAECP$ does the drive through the digital system while $FTCP$ uses an analog connection. $PCED$ is the open loop transfer function of the active suspension damping for the large mass; note that this only affects the loops that are driving the large mass. SO is the open loop transfer function of the optical spring acting on the small mirror, which is dependent on the separation between the two mirrors, rather than the absolute position of either.

4.2.1 A : Digital PDH feedback

At the moment, this path has been disconnected because it was not required. Thus we can set $A = 0$.

4.2.2 C : OSEM coils

The OSEM coils convert voltage from the DAC into force on the large mirror via the OSEMs. We have a factor of 4 in the numerator because there are 4 OSEMs acting

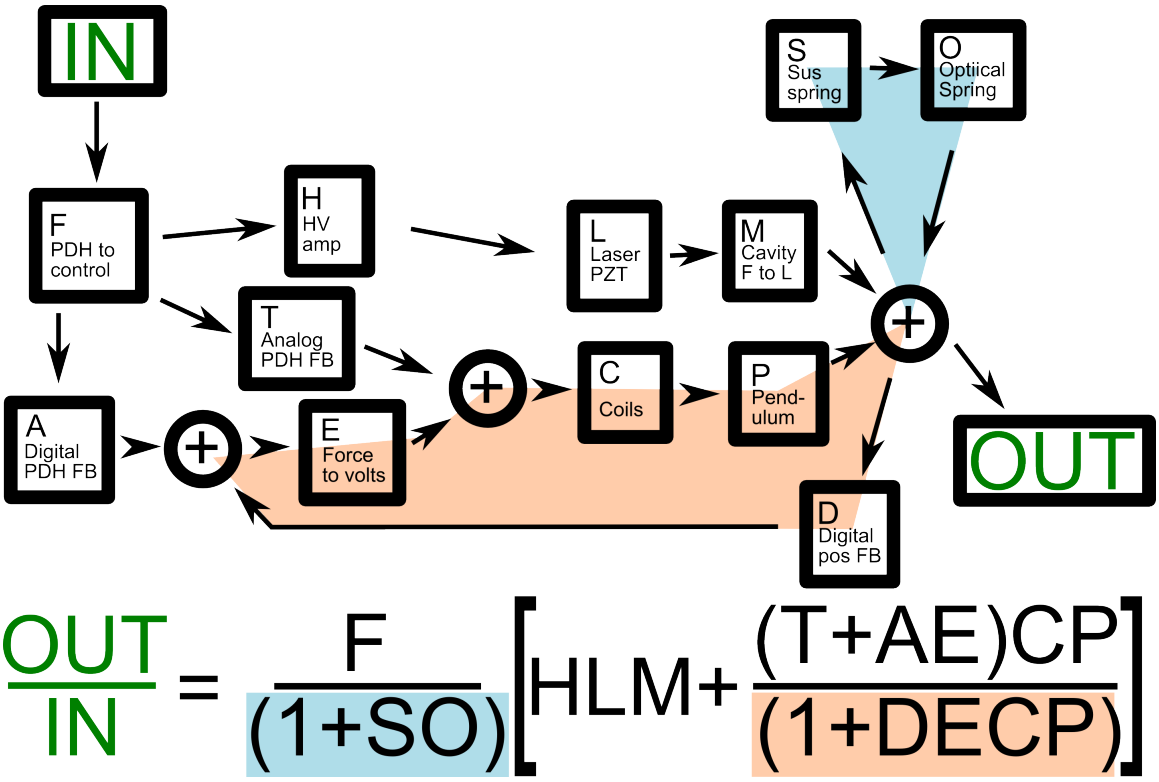

Figure 24 : Block diagram of the open loop transfer function for trap locking and operation. Two closed loops (OS and DECP) are highlighted in blue and red, respectively.

on the mass. The constant (4.91793×10^4 V/N) comes from a measurement made in October 2013 and recorded in the SUGWG logbook (entry number 439).

$$C = \frac{4}{4.91793 \times 10^4 \text{ V/N}}. \tag{4.5}$$

4.2.3 D1 and D2 : Digital feedback based on optic motion

The input to each of these blocks the is motion of a single optic relative to the OSEMs. The OSEMs put out a current proportional to the position of the mass, which is digitized. The output is a drive signal which gets added into the OSEM drive of trap 1 and trap 2, respectively. The position measurements from each optic have filters applied from the TRAP1_SUSPOS and TRAP2_SUSPOS filter banks. In D1, we have an AC coupling filter(Z: 0, P: 0.5), a highpass (Z: 1, P: 100), and a fourth order Chebychev lowpass filter at 200Hz with 1dB of passband ripple (P: $67.3977 \pm \imath 81.4946$, $27.9074 \pm \imath 196.677$ G: -0.891251). There is also a gain of 10, which includes the filter gain, the conversion of position of the optics relative to the OSEMs into voltage, and the conversion from volts to meters in the digital system. See fig. 25.

From the Matlab code:

```
tf = (1i*freq - 0) .* (1i*freq - 1)...
    ./ (1 + 1i*freq / 0.5)...
    ./ (1 + 1i*freq / 100)...
    ./ (1 + 1i*freq / (67.3977+1i*81.4946))...
    ./ (1 + 1i*freq / (67.3977-1i*81.4946))...
    ./ (1 + 1i*freq / (27.9074+1i*196.677))...
    ./ (1 + 1i*freq / (27.9074-1i*196.677))...
    .* -0.891251...
    .* Dgain;
```

We do not consider the effects of D2 because we are not putting any active drive through it. Thus it will not shape the loop as drastically as D1. The coupling between the mirror position and the ring position drops off drastically (f^{-2}) above the position resonance of the glass suspension ($\approx$ 18 Hz). As we improve the lock, we expect that we will be able to reduce or even remove active feedback on the ring.

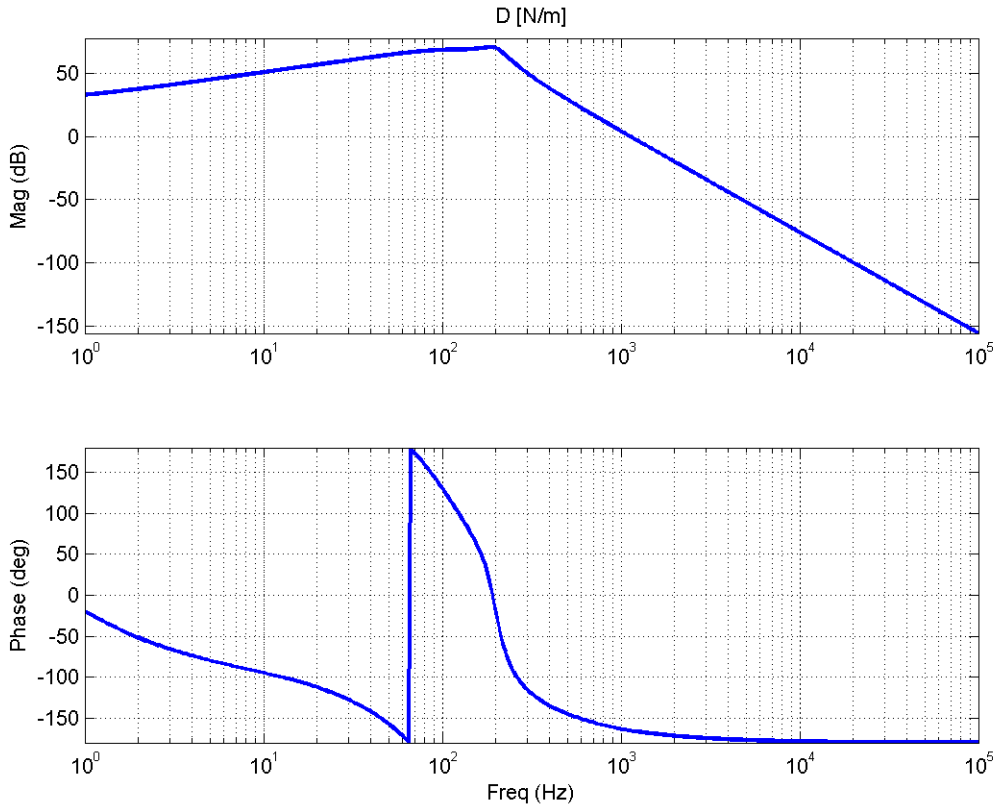

Figure 25 : D1, the transfer function from the position of optic 1, the input coupler, to a digital drive force.

4.2.4 E : Force to volts

The digital system converts the force output of digital filters into volts so that it can be sent out of the digital system to the OSEMs. We include a factor of 4 because we have 4 OSEMs. Note that $CE = 1$.

$$E = \frac{1}{4} 4.91793 \times 10^4 \text{V/N}. \tag{4.6}$$

4.2.5 F : Trap PDH servo

This is the transfer function of the Trap Servo, the RF photodiode, and the mixer. Input to this is the cavity length, read out through the PDH method. The output is a voltage. The variable 'mxrpd,' which is the conversion from cavity length to the voltage output of the mixer, is dependent on power, cavity mode matching, and the PDH readout at the mixer. mxrpd, measured at full power, just below the oscillation point, is about 10^9 V/m. See fig. 26. At the moment, we are only using the 100 Hz integrator. This has been modeled completely with the 'Analog' library developed by Stefan Ballmer, rather than calculating the algebraic expressions.

4.2.6 P : Pendulum

The pendulum transfer function of the large mass converts a force to a displacement in the position direction. The resonant frequency is $f_L = 1.4$Hz and the Q factor is about 200. The mass of the input coupler is $m_L = 300$ g.

$$P = \frac{1}{4\pi^2 \left[m_L (f_L^2 - f^2) + \frac{i f f_L}{2Q} \right]}. \tag{4.7}$$

4.2.7 S : Suspension spring

The glass suspension connects the small optic to the ring; it acts as a high-Q spring. An optical lever is used to damp oscillation modes other than the position mode. It converts a force to a displacement in the position direction. The resonant frequency of the suspension is $f_s = 18$ Hz and the small mass is $m_s = 0.41$ g.

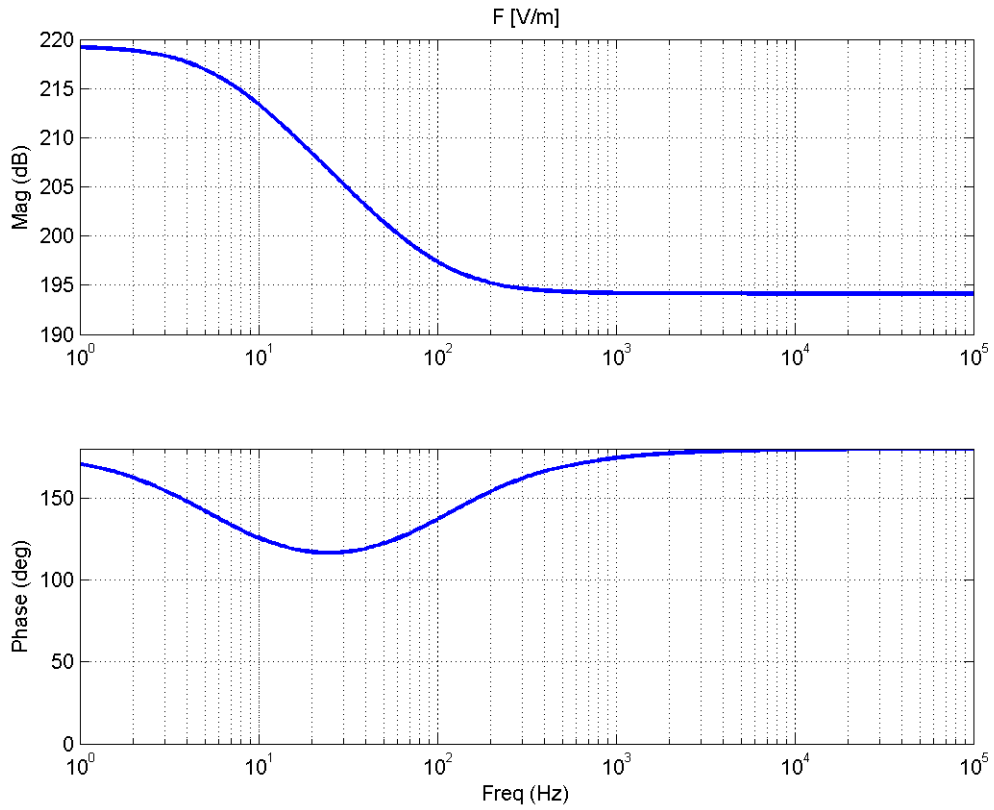

Figure 26 : Calculated trap servo TF. The main components are a 1 kHz lowpass filter and a user-adjustable gain.

$$S = \frac{1}{m_s(2\pi f_s)^2} \frac{1}{\left(1 - \left[\frac{f}{f_s}\right]^2\right)}. \tag{4.8}$$

4.2.8 O : Optical spring

The optical spring has a transfer function that looks very much like that of a physical spring. Depending on detunings and power ratio, we should see stable or unstable behavior. One such transfer function is plotted in figure 28. We should note that optical losses before the cavity have to be considered when determining the power in the cavity, as well as the cavity detuning and angular displacements of the mirrors. At the moment we are calculating this using Finesse [1].

[1] gwoptics.org/finesse/

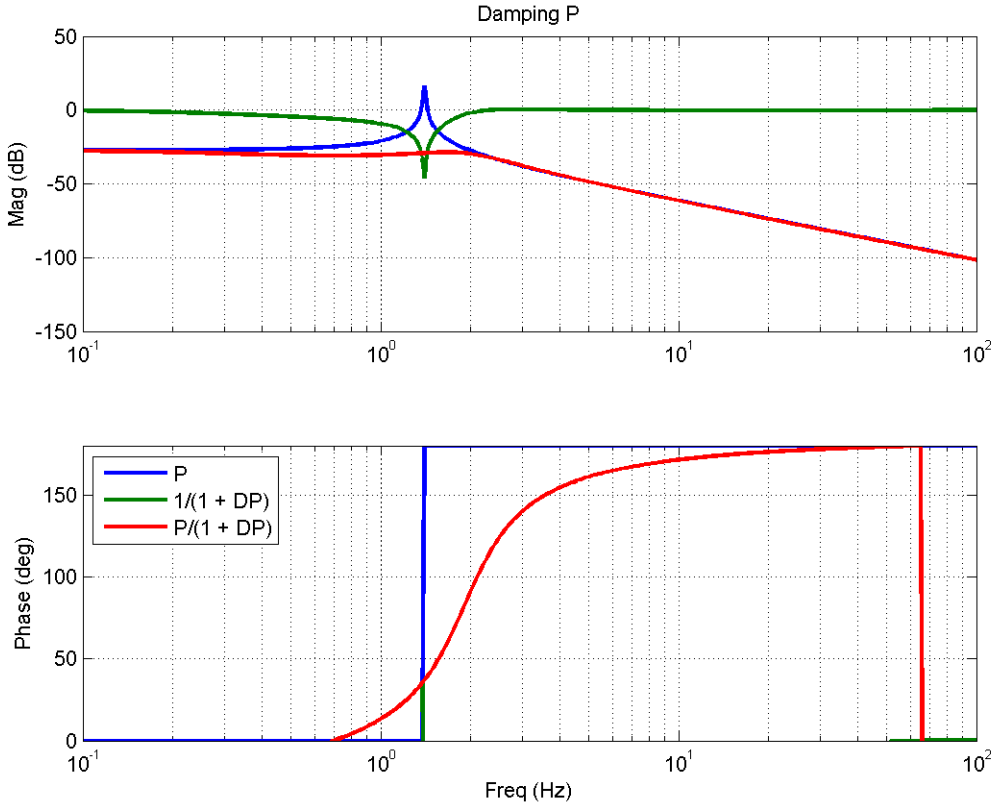

Figure 27 : Damped large mass pendulum transfer function.

Combining this spring constant with S in a closed loop gives us the behavior of the optical spring on the small mass, and thus cavity length. Below, in equation 4.9, is the effect of the optical and mechanical springs on changes in the cavity length.

$$\frac{1}{1+OS} = \frac{k_m - m\omega^2}{k_m + k_{os} - m\omega^2}. \tag{4.9}$$

4.2.9 L : Laser PZT

The laser PZT converts a voltage to a shift in the laser frequency. The number is taken from the product spec sheet.

$$L = -1.7 \times 10^6 \text{ Hz/V}. \tag{4.10}$$

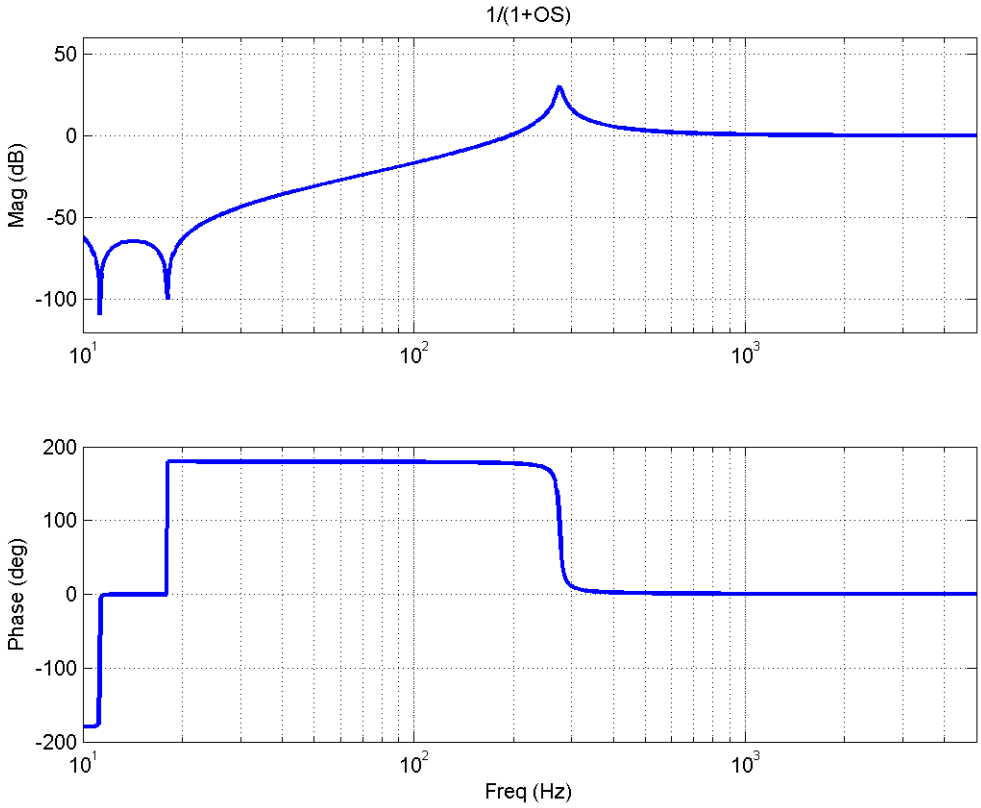

Figure 28 : Plot of the closed loop behavior of the optical spring and the glass suspension.

4.2.10 M : Cavity response

Changes in the laser frequency can be converted into an effective change in the cavity length. The cavity length l is 0.07 m. This only works for $l \gg \lambda_0$.

$$M = \frac{l\lambda_0}{c}. \tag{4.11}$$

4.2.11 H : HV amplifier

H is the HV amplifier (with HV bypass) which drives the laser PZT (See fig. 29). The HV bypass was introduced to bypass the HV amplifier above its unity gain frequency to increase the feedback bandwidth. It is described in the SUGWG ALog in entry 412. The overall behavior of the amplifier and the bypass is designed to look like this simplified model:

$$H = \frac{70}{1 + \imath f/146}. \tag{4.12}$$

We actually interpolate the data for this block, so that we don't run into trouble in the discrepancy region.

4.2.12 T : Analog PDH feedback to coil drivers

This is a SR560 that operates between the Trap Servo control signal and the analog drive for the large optic OSEMs.

It is currently set to a 1 kHz 6 dB lowpass with a gain of 200, so it is modeled as

$$T = \frac{200}{1 - \imath \frac{f}{1\text{ kHz}}}. \tag{4.13}$$

4.3 Photothermal effect on loops

The photothermal effect is directly related to how close the cavity is to resonance. This is affected by the total cavity length and the frequency of the light entering the cavity. In figure 30, we see that the photothermal effect (Pt) can be treated as a closed loop acting on the cavity length L_{cav}.

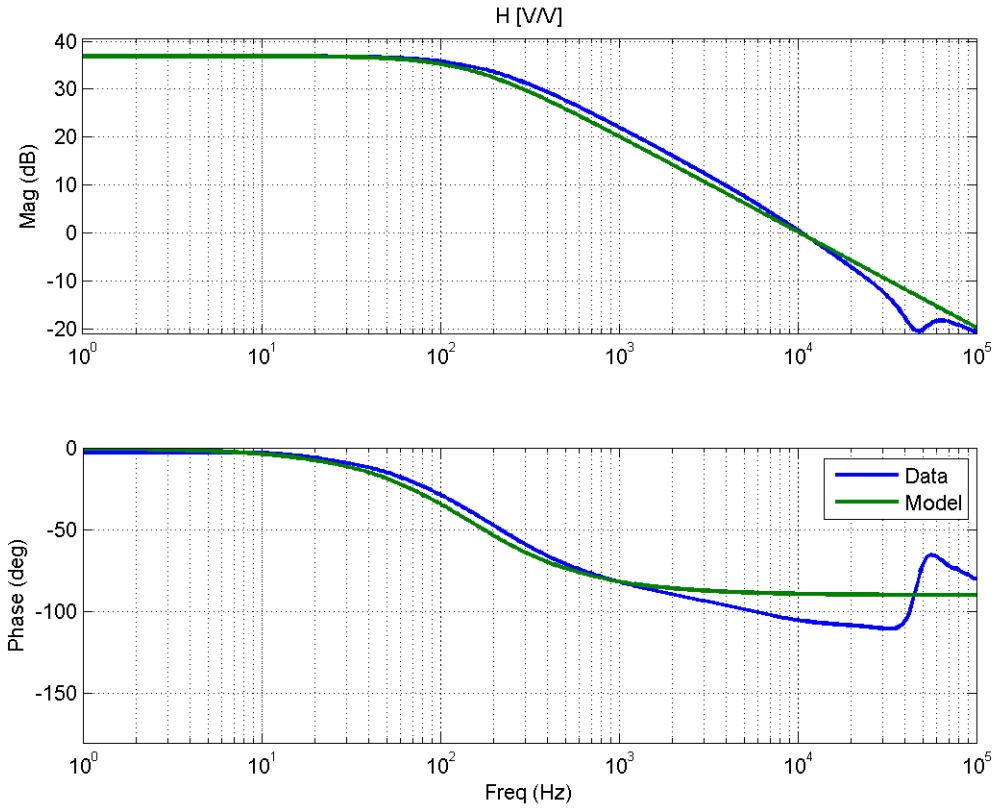

Figure 29 : HV amplifier transfer function. Includes a high-frequency bypass to increase feedback bandwidth.

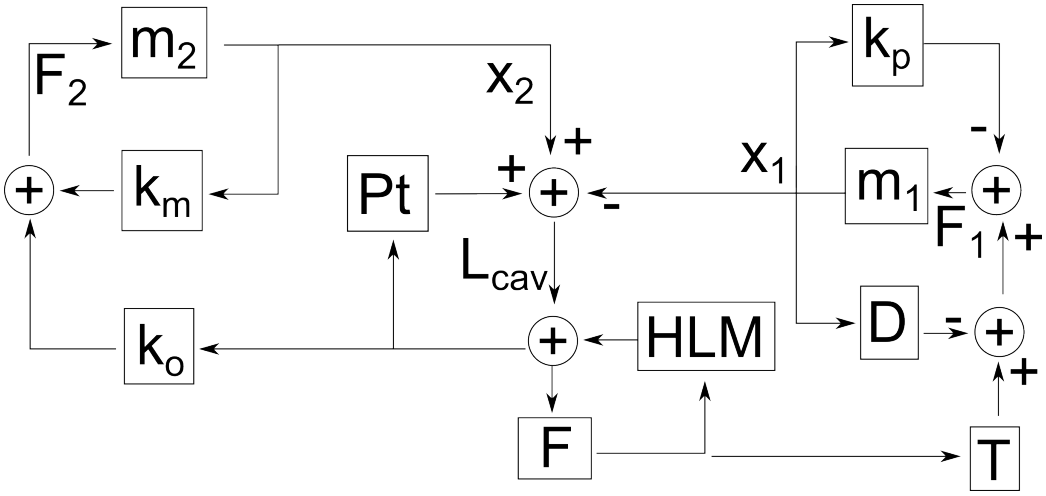

Figure 30 : Loop diagram for a single degree of freedom, including photothermal feedback, Pt. The optical spring loop on the left side (k_O, k_m, and m_2) is affected by the photothermal effect (Pt). We measure the behavior of the optical spring by measuring the open loop transfer function of the system at F, then dividing out the transfer functions of the control system (HLM, T, D, etc.). This leaves us with the closed loop transfer function of the optical spring with the photothermal effect.

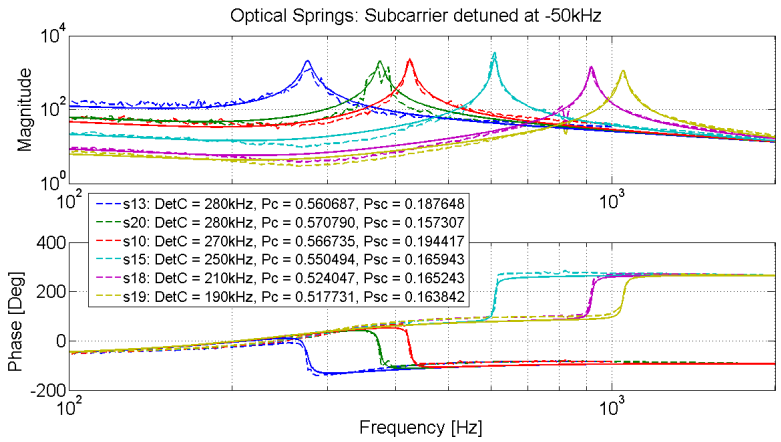

Figure 31 : Open loop TF of the system with several different carrier detunings. Changing the carrier detuning changes the resonant frequency of the springs and their stability. Included are both measurements and corresponding models.

Chapter 5

Observation of photothermal feedback in a stable dual-carrier optical spring

The following chapter is taken from a paper "Observation of photothermal feedback in a stable dual-carrier optical spring" by David Kelley, James Lough, Fabian Mangaa-Sandoval, Antonio Perreca, and Stefan W. Ballmer. It was published in Physical Review D, volume 92, issue 6, on September 24, 2015 [44].

5.1 Abstract

We report on the observation of photothermal feedback in a stable dual-carrier optical spring. The optical spring is realized in a 7 cm Fabry-Perot cavity comprised of a suspended 0.4 g small end mirror and a heavy input coupler, illuminated by two optical fields. The frequency, damping, and stability of the optical spring resonance can be tuned by adjusting the power and detuning of the two optical fields, allowing for a precise measurement of the absorption-induced photothermal feedback. The magnitude and frequency dependence of the observed photothermal effect are consistent with predicted corrections due to transverse thermal diffusion and coating structure. While the observed photothermal feedback tends to destabilize the optical spring, we also propose a small coating modification that would change the sign of the effect, making a single-carrier stable optical spring possible.

5.2 Introduction

The Advanced Laser Interferometer Gravitational-Wave Observatory (aLIGO) [45], together with its international partners Virgo [46] and KAGRA [47], aim to directly observe gravitational waves emitted by astrophysical sources such as coalescencing of black hole and neutron star binary systems. The installation of the Advanced LIGO detectors is completed, and commissioning towards the the first observation run is ongoing. Preliminary astrophysical data is expected in 2015. The sensitivity of those advanced gravitational-wave detectors in the observation band is limited by the quantum noise of light and the thermal noise associated with mirror coatings. A contributor to the thermal noise, expected to dominate in future cryogenic gravitational-wave detectors, is thermo-optic noise [48, 49, 50]. It is caused by dissipation through thermal diffusion.

The same physics also leads to an intensity noise coupling, known in the literature as photo-thermal effect [51]. The low frequency behaviour of the photo-thermal effect was predicted in [49] and experimentally measured in a Fabry-Perot cavity by De Rosa et. al. [52]. The physics relevant for the the high frequency behaviour, dominated by the details of the coating, was investigated in [50] in the context of studying thermo-optic noise. It was extended to a full model of the photo-thermal transfer function in [53]. Here we explore the thermo-optic effect in the context of an optical spring. The coupling acts as an additional feed-back path. The phase of the coupling becomes important and can directly affect the stability of the optical spring resonance. We can exploit this dependence for a precision measurement of the photo-thermal coupling, even if it is driven by the residual few-ppm absorption of a high-quality optic.

The desire to lower the quantum noise in the gravitational-wave observation band has driven the power circulating in the Advanced LIGO arm cavities up to about 800 kW. The high laser power, in turn, couples the angular suspension modes of the two cavity mirrors. This Sidles-Sigg instability [1] creates a soft (unstable) and a hard mode, whose frequency increases with the intra-cavity power. The detector's angular control system must control the soft and damp the hard mode, and at the same time must not contaminate the observation band, starting at 10 Hz in the case of Advanced LIGO. Future gravitational wave detectors aim to extend the observational band to even lower frequencies, further aggravating this limitation. We previously proposed a

model [3] to overcome the angular instabilities, based on a dual-carrier optical spring scheme demonstrated by Corbitt et al., in 2007 at the LIGO laboratory [18]. The proposed angular trap setup uses two dual-carrier beams to illuminate two suspended optical cavities which share a single end mirror. As first step towards the experimental demonstration of the scheme we built and operated a prototype, single-cavity optical trap, capable of controlling the cavity length only [43]. The data presented in this chapter was taken with this prototype. The next version of the angular trap setup will also allow us to measure the photo-thermal effect on a folding mirror. Heinert et. al. [54] predicted excess thermal noise for folding mirrors due to transverse heat diffusion. The result has not yet been experimentally confirmed, but since the same physics will also lead to an enhanced photo-thermal transfer function, the prediction can be verified with a photo-thermal transfer function measurement.

The paper is structured as follows: Sections 5.3 and 5.4 will review the idea of a dual-carrier optical spring and the photo-thermal effect respectively. Section 5.5 describes the experimental setup and we discuss the result in section 5.6. Finally, section 5.7 suggests a coating modification to make a single-carrier optical spring feasible.

5.3 Dual-carrier optical spring

A Fabry-Perot cavity detuned from resonance couples the intra-cavity power linearly to the mirror position. The response is delayed by the cavity storage time. The resulting optical spring constant is given by [3].

$$K_{OS}^{\text{1field}} \approx K_0 \frac{1}{1+\frac{\delta^2}{\gamma^2}-\frac{\Omega^2}{\gamma^2}+i2\frac{\Omega}{\gamma}} \tag{5.1}$$

$$K_0 = P_0 t_1^2 r_2^2 \frac{8kr_1r_2}{c(1-r_1r_2)^3} \frac{\frac{\delta}{\gamma}}{(1+\frac{\delta^2}{\gamma^2})} \tag{5.2}$$

where P_0 is the incident power, corrected for mode-matching losses, $k = 2\pi/\lambda$ is the wave vector of the light, t_i and r_i are the mirror amplitude transmissivity and reflectivity for input coupler ($i = 1$) and end mirror ($i = 2$), and γ, δ and Ω are the cavity line, cavity detuning, and mechanical frequency. The value of K_{OS} lies in either the 2nd or 4th quadrant of the complex plane, and the associated radiation pressure

force creates either a anti-restoring and damping (red detuning) or a restoring and anti-damping force (blue detuning) [17].

Two spatially overlapping optical fields, the carrier and sub-carrier, with opposite detuning sign and with an opportune power ratio can be used to cancel the instability [18]. The total optical spring K_{OS} is the sum of the individual springs

$$K_{OS} = K_{OS}^{c} + K_{OS}^{sc} \tag{5.3}$$

Where K_{OS}^{c} and K_{OS}^{sc} are given by equation 5.1. The dual-carrier optical spring can be tuned to lie in the 1st quadrant for the frequency band of interest. When acting on a suspended cavity end mirror with mass m and mechanical suspension spring constant K_m the optical spring becomes a feed-back loop with a closed loop response function

$$\frac{x}{F_{ext}} = \frac{1}{-m\Omega^2 + K_m + K_{OS}} \tag{5.4}$$

The tunability of the optical spring K_{OS} in both magnitude and phase allows experimental fine-tuning of the poles of equation 5.4 to lie exactly on the real axis, resulting in an infinite Q of the optical spring (critical stablility). Experimentally this can be done up to a maximum Q, above which the measured transfer function data no longer permits distinguishing between a stable and an unstable spring. The phase of the total spring constant at resonance can then be determined with a precision given by $1/Q$. The suspension mechanical spring constant has to have a positive imaginary part, but it can be designed to be very small. Loss angles of 10^{-5} are easily achievable, and are further diluted by the magnitude of the ratio of K_{OS}/K_m. The contribution to the phase of the total spring constant from the mechanical suspension is thus expected to be negligible. The imaginary part of the optical spring K_{OS} on the other hand is closely related to its real part through equations 5.3 and 5.1, and is very accurately predicted based on the resonance frequency, carrier to sub-carrier power ratio as well as the detuning of carrier and subcarrier, i.e. only power ratios and frequencies. As a result, any deviation in phase from the expectation of equation 5.1 around the optical spring resonance is easily and repeatably observable with a precision given by the inverse of the experimentally resolvable Q, and an accuracy determined only by frequency and power ratio measurements.

5.4 Photo-thermal effect

Power absorption on the surface of an optic leads to an increase of the surface temperature. The depth of the heated layer is given by the diffusion length $d_{\mathrm{diff}} = \sqrt{\kappa/(\rho C \Omega)}$, where κ, C and ρ are the thermal conductivity, heat capacity and density of the material, and Ω is the observation angular frequency. In the large-spot size limit, i.e. $\mathrm{w} \gg d_{\mathrm{diff}}$, and neglecting coating effects, the displacement of the surface is given by (e.g. [49, 53])

$$\triangle z = \bar{\alpha} \int_0^\infty T dz = \bar{\alpha} \frac{j}{i\Omega\rho C} \tag{5.5}$$

where $\bar{\alpha} = 2(1+\sigma)\alpha$ is the effective expansion coefficient under the mechanical constraint that the heated spot is part of a much larger optic [50, 55]. α and σ are the regular linear expansion coefficient and Poisson ratio. $j = P/(\pi \mathrm{w}^2)$ is the absorbed average surface intensity of the Gaussian beam with beam radius w ($1/e^2$ intensity). This simple picture needs two important refinements. First, for frequencies Ω around and below $\Omega_c = 2\kappa/(\rho C \mathrm{w}^2)$ the transverse heat diffusion leads to a multiplicative correction factor to equation 5.5 derived by Cerdonio et al. [49]:

$$I(\Omega/\Omega_c) = \frac{1}{\pi} \int_0^\infty du \int_{-\infty}^\infty dv \frac{u^2 e^{-u^2/2}}{(u^2+v^2)\left(1 + \frac{(u^2+v^2)}{i\Omega/\Omega_c}\right)} \tag{5.6}$$

As expected, for $\Omega \gg \Omega_c$, the correction factor approches 1. For a fused Silica substrate, SiO_2, and a Gaussian beam spot radius of $\mathrm{w} = 161$ μm this correction becomes large below $\Omega_c/(2\pi) = 10$ Hz, but is measurably different from unity even at 1 kHz. (See fig 32)

Second, for high frequencies, the diffusion length becomes comparable to the coating thickness. Since the optical field is reflected by a dielectric stack, the effective mirror displacement is given by [50, 53]

$$\triangle z = \sum_i \left[\frac{\partial \phi_c}{\partial \phi_i} (\beta_i + \bar{\alpha}_i n_i) + \bar{\alpha}_i \right] \bar{T}_i d_i \tag{5.7}$$

where $\bar{\alpha}_i$, $\beta_i = dn/dT$ and n_i are the constrained effective expansion coefficient, the temperature dependence of the index of refraction, and the index of refraction itself for layer i. $\frac{\partial \phi_c}{\partial \phi_i}$, the dependence of the coating reflected phase on the round trip optical phase in layer i, is always negative, resulting in a sign change and enhancement of

the bracket in equation 5.7 for the first few layers. $\bar{T}_i d_i$ is the temperature profile driven by the absorped intensity j, integrated across layer i. For a $Ta_2O_5 : SiO_2$ coating used in gravitational wave detectors we find a measureable enhancement of the photo-thermal transfer function around 1 kHz [53]. Additionally, depending on the detailed absorption profile, a sign change can occur above about 100 kHz.

For the experiment parameters discussed in this chapter, i.e. a Gaussian beam spot radius of w = 161 μm and a mirror coating with about 13 doublet layers both effects are relevant in the 100 Hz to 1 kHz band. Their contributions are plotted in figure 32.

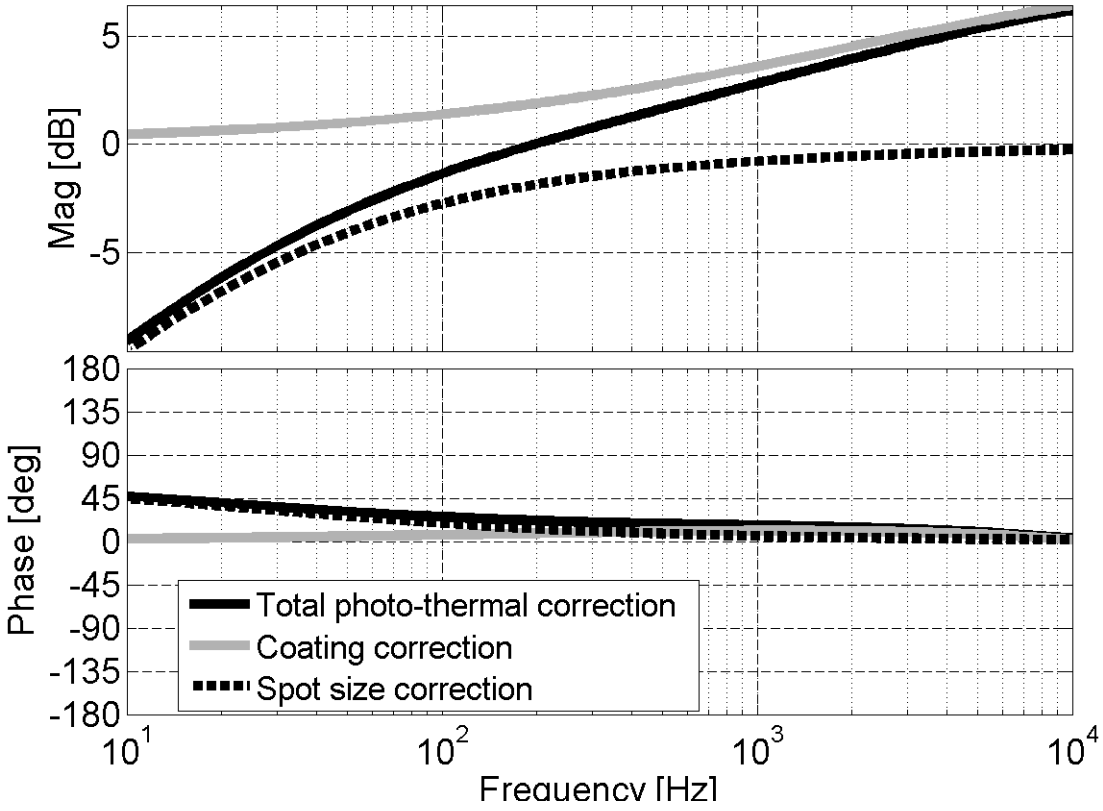

Figure 32 : Correction factors for the photo-thermal transfer function of a fused silica mirror with a dielectric coating (solid black). The solid grey trace is the coating correction for a 13-doublet $\lambda/4$ coating. The dashed black trace shows the effect of a Gaussian beam spot with w = 161 μm radius. To get the full transfer function, multiply with equation 5.5, adding an overall $1/f$ shape. The calculation is based on material parameters show in table 5.

5.5 Experimental setup

5.5.1 Cavity

λ_0	1064 nm
Mirror RoC	5.0 cm
L_0	7.0 cm
Spot size	161 μm
FSR	2.14 GHz
Finesse	7500
Cavity Pole	143 KHz

δf_C	213-290 KHz
δf_{SC}	27-36 KHz
P_C input	225-239 mW
P_{SC} input	65-78 mW

Table 4 : Parameters of the optical spring cavity. The range of values for the carrier and subcarrier detuning frequency (δf_C, δf_{SC}) and input power (P_C, P_{SC}) indicate the variation between individual measurements.

The optical spring cavity is composed of two suspended mirrors in a vacuum chamber, each with radius of curvature RoC = 5 cm and power transmissivity $T = 4.18 \times 10^{-4}$. The measured finesse is 7500 ± 250 and the cavity length is $L_0 = 7.0 \pm 0.2$ cm. We chose a short cavity to minimize frequency noise coupling. The cavity has a free spectral range (FSR) of about 2.14 GHz and cavity pole $f_{pole} = \gamma/(2\pi) = 143$ kHz. The input mirror mass is 300 g, designed to be heavy to make it insensitive to radiation pressure; it is suspended as a single stage pendulum with mechanical resonances, i.e. position, pitch and yaw, close to 1 Hz. The end mirror has a mass of 0.41 ± 0.01 g and is 7.75 mm in diameter. It is suspended with three glass fibers from a 300 g steel ring, shown in figure 33. The steel ring has diameter of 7.6 cm and is itself suspended. The input mirror is actively controlled by an electronic feedback system, while the end mirror is free to move in the glass suspension abobe its resonance frequency of 18 Hz, and is only subject to the optical spring radiation pressure.

5.5.2 Input field preparation

The optical field incident on the optical spring cavity consists of two beams, a carrier and a subcarrier, as described in Section 5.3. As shown in figure 34, a 1064 nm laser is split into a carrier and a subcarrier beam at the polarizing beam splitter PBS1.

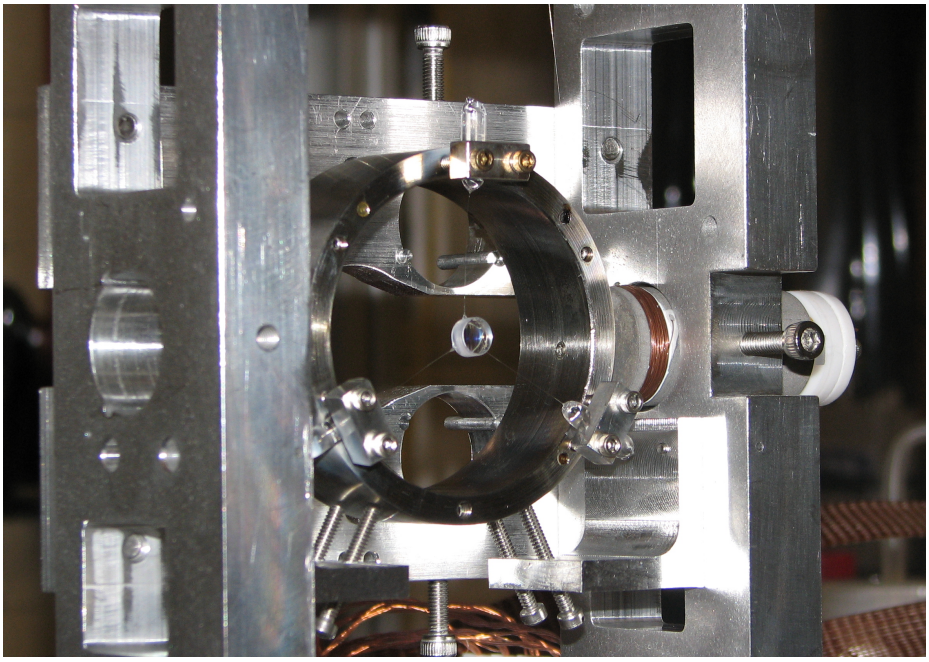

Figure 33 : A picture of the small end mirror suspended from a steel ring by glass fibers. The ring is suspended from a small optics suspension (SOS) with tungsten wire. The SOS provides DC alignment control while allowing the mirror to move freely above the 18Hz resonance of the fiber suspension. The end of the fiber is a small glass nub attached to the mirror with epoxy. This produces a fairly high suspension Q of about $5 \cdot 10^5$. The resulting contribution of damping in the opto-mechanical spring is insignificant compared to the damping from the optical field.

In the subcarrier path two acoustic optic modulators (AOMs) are used to impose a relative frequency shift Δ, on the subcarrier beam, leaving it at a set detuning from the carrier beam. Δ is set using an external signal generator (see Sec. 5.5.3). The two beams recombine at PBS2 and proceed towards the Fabry-Perot cavity with opposite polarization. The total power and the power ratio between the carrier and subcarrier beams are set by two half wave-plates $\lambda/2$.

The subcarrier beam is modulated by a 35 MHz electro-optic modulator (EOM). We measure the modulated light reflected by the cavity with a resonant radio-frequency photodiode (RFPD) and then demodulate to read out the cavity length with the Pound-Drever-Hall technique (PDH) [35]. We use the subcarrier to derive a PDH singal because the subcarrier requires less detuning than the carrier. We can use the PDH signal to actuate on the laser and the suspensions to lock the cavity, then turn down the gain and use the PDH signal for readout.

A small offset added to the PDH error signal shifts the locking point of the cavity to the side of the resonance, setting the subcarrier detuning δ_{sc}. We choose to introduce an offset that corresponds to a negative frequency ("red") detuning. Consequently the carrier is positively ("blue") detuned at $\delta_c = \Delta + \delta_{sc}$. An electronic locking servo can be used to process the error signal and feed back to coils, actuating on magnets mounted on the large cavity mirror, and to the laser frequency.

5.5.3 Subcarrier Servo

The high FSR of our cavity (2.14 GHz) meant that available AOMs, with much lower operating frequency ranges (65 to 95 MHz), were not suitable to lock the carrier and subcarrier on adjacent resonances. However, this same operating range prevents a single AOM from locking the two beams on the same resonance, due to the small cavity linewidth. Thus, we set the subcarrier on the same resonance fringe as the carrier using two AOMs, each one shifting the laser frequency by about 80MHz in opposite directions. One is driven by an 80 MHz crystal oscillator, while the other is driven by a servo-locked Voltage controlled oscillator (VCO) running slightly offset from 80 MHz (see figure 34). To control the offset frequency the 80 MHz signal from the crystal oscillator is mixed with the VCO output, producing a signal at the frequency difference. This difference signal is then mixed with the drive from a function generator, creating the error signal for the servo. The servo drives the

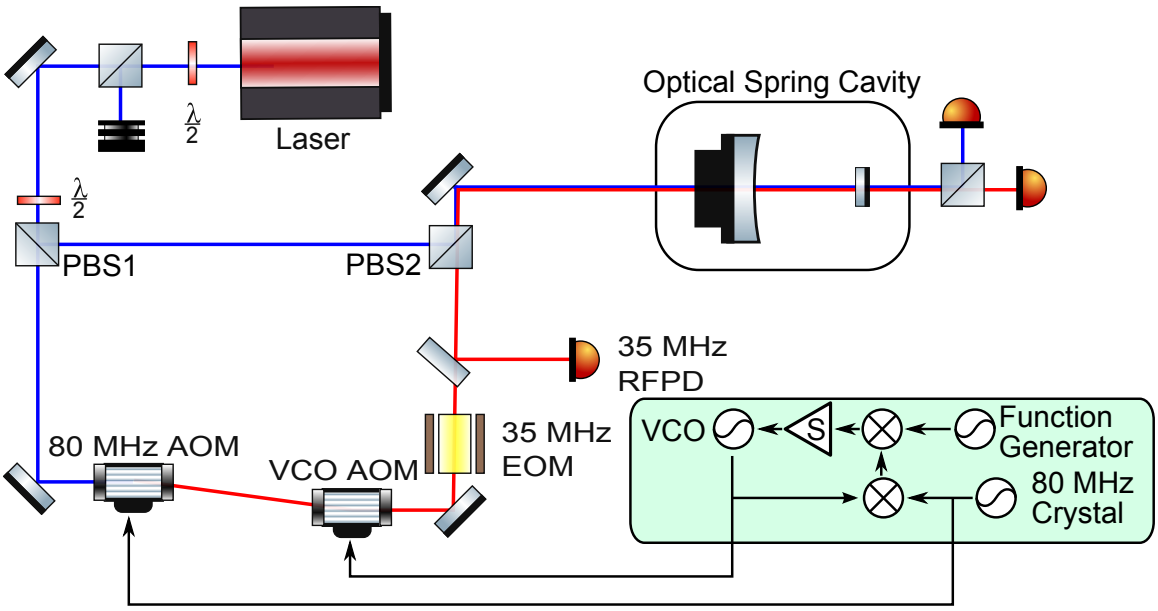

Figure 34 : A schematic layout of the optical trap experiment. The light from the laser is split into the carrier and subcarrier paths at PBS1, with a ratio determined by the $\lambda/2$ plate. The subcarrier path is frequency shifted by two AOMs under the control of the subcarrier servo (described in detail in Section 5.5.3), then recombined with the carrier at PBS2. The co-aligned mode-matched beams enter the cavity, then are individually monitored at the output. We can use the 35 MHz EOM and RFPD in a PDH scheme to read out the cavity length or lock the cavity.

frequency modulation input of the VCO, closing the loop and locking the subcarrier beam to a fixed frequency offset from the carrier beam.

This setup significantly suppresses the frequency noise from the VCO. The remaining subcarrier frequency noise (relative to the carrier) is dominated by fluctuations in the path length difference between carrier and sub-carrier, see figure 34.

5.6 Results

Using the setup described in the previous section, we locked the cavity using a PDH error signal from the sub-carrier, feeding back to the laser frequency actuator and, at low frequencies, the heavy input coupler position. In this configuration we fine-tuned the optical spring parameters (carrier and sub-carrier offset and power) and measured the PDH control loop open loop transfer function. Dividing out the known PDH loop sensing and actuation function gives us the closed loop transfer functions of the optical springs (figure 35). While we demonstrated stable and unstable dual-carrier

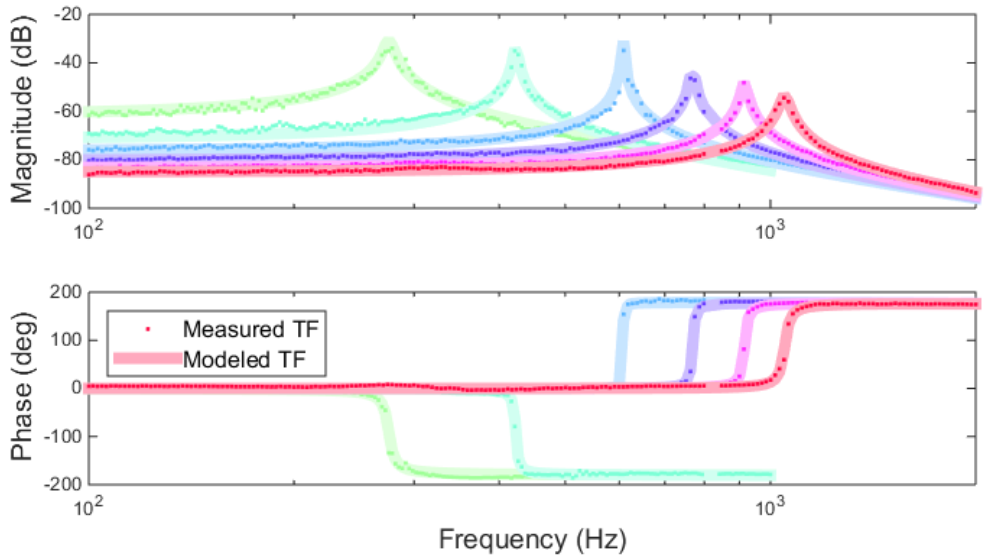

Figure 35 : Data and modeled transfer function for a series of stable and unstable springs. The modeled transfer functions include the full coating and spot size correction, computed with the measured average absorption. Stable springs show a phase drop of 180 degrees at resonance, while unstable springs show a rise of 180 degrees.

optical springs, these measurements revealed a significantly smaller phase margin of the optical spring than expected based on equation 5.4, suggesting the presence of a non-radiation-pressure feed-back path.

At a few ppm, the absorption A of the mirrors has a very small effect on the cavity finesse and no significant impact on the total transmitted power. However, this small amount of absorption still causes local heating of the optic, driving fluctuations in the surface position of the optic, and thus the cavity length, via the photo-thermal effect. If this is the dominant effect, we should be able to include the photo-thermal effect in our model and fit the model to the data, using the absorption as the free parameter. Given a set of optical spring measurements done under similar conditions, we would then expect to find a consistent absorption coefficient across measurements.

5.6.1 Analysis

For each measured optical spring transfer function we record the carrier and subcarrier transmitted powers, P_{tc} and P_{ts}, the optical spring resonance frequency f_{res}, and the difference between the carrier and subcarrier detunings $df_c - df_s$, which is set by the

function generator frequency.

We can then fit the data d using a model m, which includes the photo-thermal effect. In particular we fit the ratio d/m using a least-squares fit to minimize E, the error.

$$E = \Sigma \left| \frac{d}{m} - 1 \right|^2 \tag{5.8}$$

We fit for a small magnitude offset, the subcarrier detuning df_s, and the absorption A. We assess the fitting errors by modeling the noise in each frequency bin of the transfer function measurement, and propagating this noise through the fit. Four of the optical spring transfer functions had a measurement noise of a little less than 1 dB, while the optical springs at 276 Hz and 422 Hz had a significantly higher noise of about 3 dB. We think this noise is dominated by intra-cavity power fluctuations, most likely due to angular fluctuations.

The remaining parameters (cavity transmitted powers and carrier-sub-carrier frequency spacing) we treat as systematic errors. We propagated their measurment errors through the fit. We used a 2% measurement error for the power measurements and a 1 kHz error for the frequency separation.

After determining the absorption A for each optical spring transfer function measurement, we can take a statistical-error-weighted average to arrive at the most probable absorption coefficient for the mirror. For the full photo-thermal model we measure a consistent absorption of 2.60 ± 0.08 ppm (± 0.06 ppm statistical, ± 0.05 ppm systematic) (see figure 36). The naive $1/f$ model yields an absorption of 3.27 ± 0.10 ppm (± 0.08 ppm statistical, ± 0.06 ppm systematic). The detailed model with coating and spot size corrections is slightly preferred by the data over the naive $1/f$ model, i.e. the result is more consistent with the same absorption at all frequencies. However the errors in our mesurement are too large to make this statement with any sigificant certainty.

Since this measurement is based on the missing optical spring phase on resonance, we can also express the result as extra phase. Near the resonance the optical spring constant is close to real, while the photo-thermal effect is almost purely imaginary. Thus we approximately find for the extra phase ϕ

$$\phi = 2m\Omega^2 \frac{c}{2} \frac{\bar{\alpha}}{\Omega \rho C \mathrm{w}^2 \pi} A I_{\mathrm{corr}} \approx 0.4^\circ \frac{A I_{\mathrm{corr}}}{1 \text{ ppm}} \frac{f}{1 \text{ kHz}} \tag{5.9}$$

Here the leading factor of two accounts for the two mirrors, I_{corr} is the real part of

the total correction factor plotted in figure 32, and we used the material parameters for fused silica (see table 5). Figure 37 shows the measured extra phase on resonance, together with the prediction from the photo-thermal feed-back with the best-fit absorption. The figure also shows the expected phase due to the dual-carrier optical spring, as well as the total phase of the complete model. Finally it is worth mentioning that this is a remarkably precise way to measure the phase of the open loop transfer function - the error bars in figure 37 are as small as 0.04°.

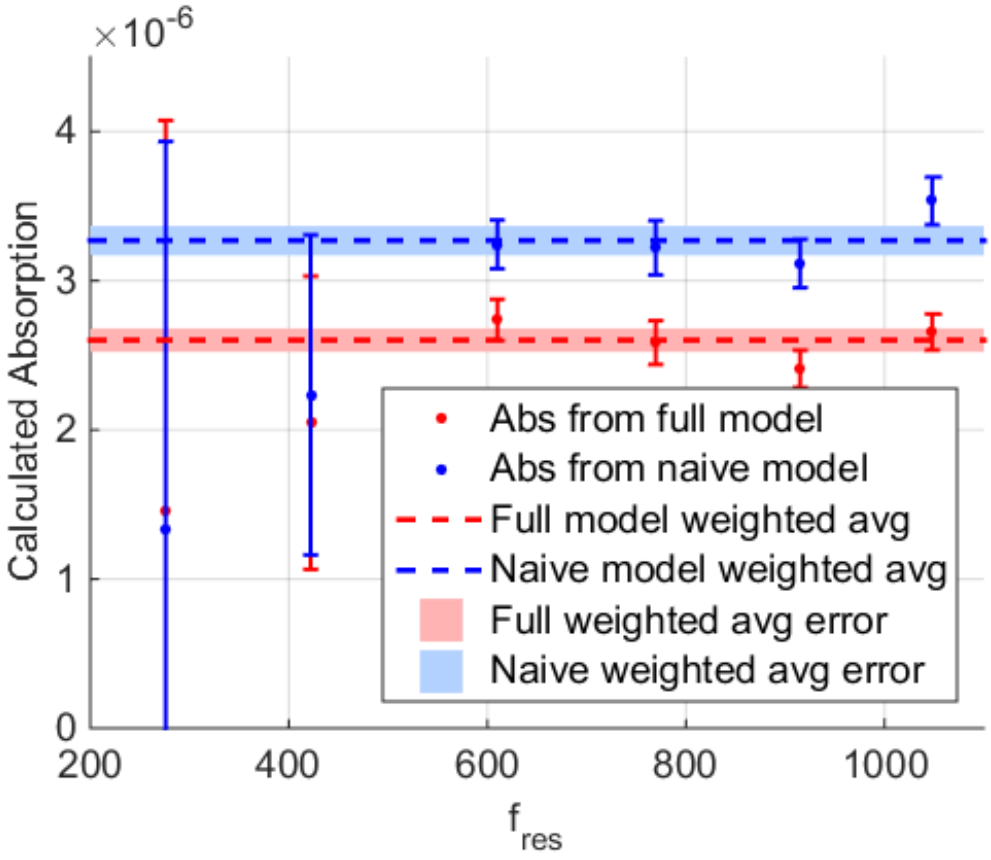

Figure 36 : Absorption fit for naive and full models. The full model absorption is consistent with a constant absorption of 2.60 ± 0.08 ppm. The naive $1/f$ model predicts 3.27 ± 0.10 ppm. The transfer function data for the lowest two resonant frequencies was significantly noisier. Also, at lower frequencies the photo-thermal effect has a smaller effect on the total optical spring. Both effects result in the larger error bars at low frequencies.

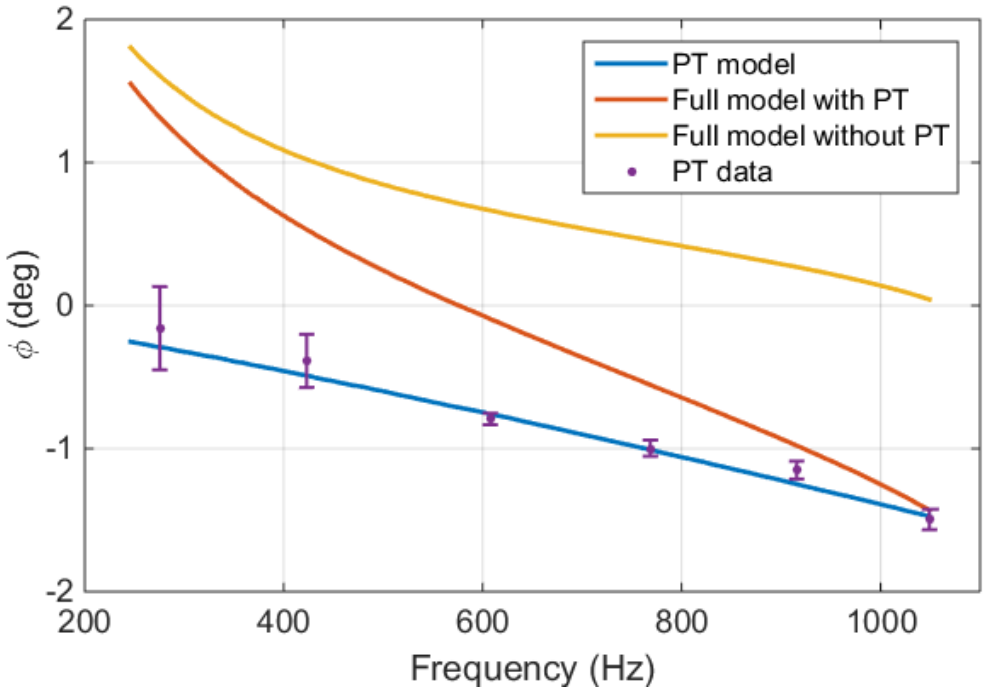

Figure 37 : Feedback phase in the system due to the optical spring and photo-thermal effect. The measured extra phase is consistent with 2.60 ppm of absorption. The error bars are as small as $\pm 0.04°$, a remarkable precision for an open loop transfer function phase measurement.

5.7 Stable single-carrier optical spring

In the experiment at hand the photo-thermal feed-back always pushed the optical spring resonance closer to instability. Perhaps the most interesting question is whether we can change the sign of this feed-back path and exploit it to stabilize an otherwise unstable optical spring. It was pointed out in [53] that this naturally occurs above about 100 kHz for a regular dielectric coating. At those frequencies the thermal diffusion length only affects the first few layers of the coating, which affect the overall coating reflected phase differently than the rest of the coating. However it is actually quite simple to get this sign inversion to occur at a much lower frequency. Increasing the thickness of the initial half-wavelength SiO_2 layer - but keeping it an odd multiple of half the wavelength - will boost the effect from the first layer, thus lowering the frequency at which this sign inversion occurs. Indeed this effect can be strong enough that the damping effect from the sub-carrier is not needed to generate a stable optical spring. To illustrate this, figure 38 shows a set of six optical springs with parameters

identical to the ones shown in figure 35, except that we set the sub-carrier power to zero (i.e. they are single-carrier optical springs), and we increased the first SiO_2 coating layer from 0.5 wavelength to 20.5 wavelength.

Such a modified coating would thus allow detuned self-locking of an optical cavity, using just one laser frequency. It does rely on a small amount (order 1 ppm) of optical absorption in the coating, but this level of absorption is often unavoidable anyway, and does not prevent high-finesse cavities.

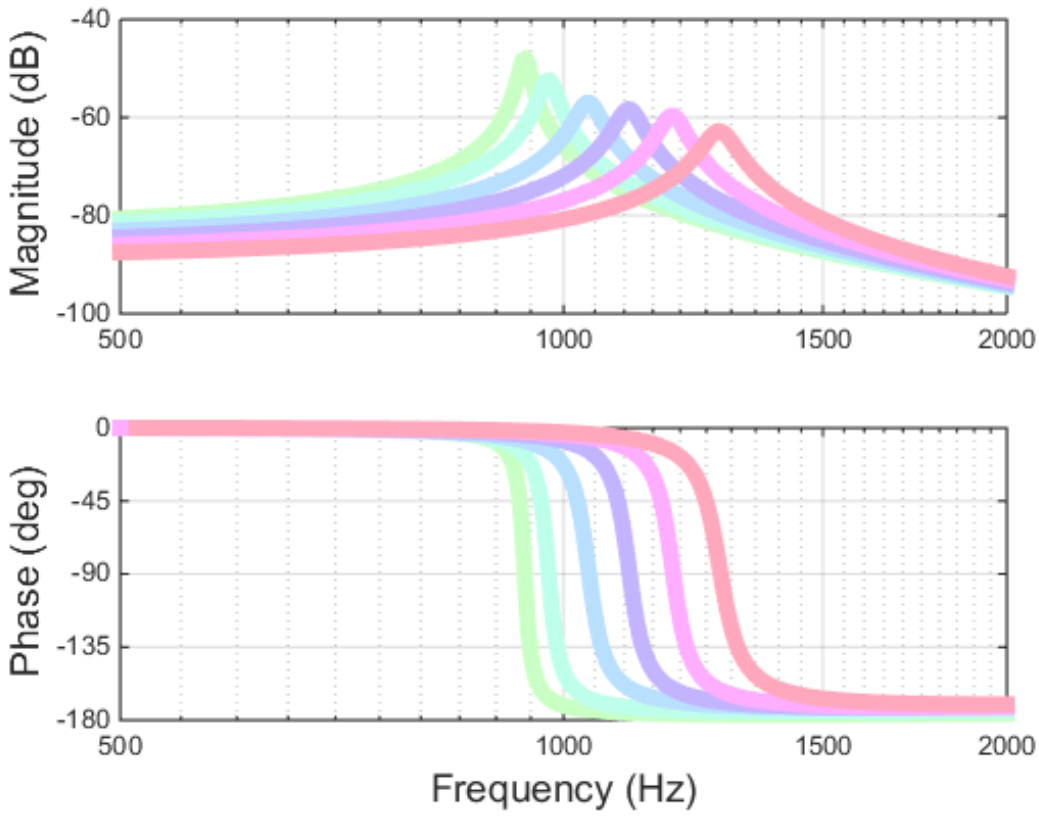

Figure 38 : Stable single-carrier optical springs (no sub-carrier) with modified coating - the first coating layer is 20.5 wavelength thick. See text for details. The six traces otherwise have the same parameters as the best-fit optical springs in figure 35.

5.8 Conclusions

We observed photo-thermal feedback in an experimental optical spring setup for a 0.4 gram mirror. We made measurements for a range of optical spring resonant

frequencies, and used a least squares fit to calculate the absorption. The data is consistent with the predictions of the complete model presented in Section 5.4, but only sligthly prefers it over a simple model that ignores any heat diffusion in the coating and transverse to the optical axis. We also show that a small modification of the first layer of the high-reflectivity coating would be enough to reverse the sign of the photo-thermal feed-back, to the extent that a single-carrier, dynamically and statically stable optical spring becomes feasable.

Repeating the presented measurement with a folding mirror in a cavity should also allow us to confirm the predicted enhancement of thermal noise for folding mirrors [54] . This noise will affect any gravitational-wave interferometer design making use of folding mirrors in the arm cavities [33].

Parameters Ta_2O_5:SiO_2	Symbol	SiO_2	Ta_2O_5	Unit
Refractive Index (@1064 nm)	n	1.45	2.06	-
Specific Heat	C	746	306	J/kg/K
Density	ρ	2200	6850	kg/m^3
Thermal Conductivity	κ	1.38	33	W/m/K
Thermal expansion coef.	α	0.51	3.6	ppm/K
Thermo-Optic coef. (1μm)	$\beta = \frac{dn}{dT}$	8	14	ppm/K
Poisson ratio	σ	0.17	0.23	-
Youngs Modulus	E	72.80	140	GPa

Table 5 : Parameters for fused silica (SiO_2) and tantulum-pentoxide (Ta_2O_5). The values are taken from [50] and [55].

Chapter 6

Angular trapping

6.1 Introduction

The Advanced LIGO detectors are now running and taking science data. Final upgrades should have the detectors at design sensitivity in a few years. At that point, we will need to have potential upgrades designed and demonstrated so that they can be considered for incorporation into the detectors.

One such area of interest is the use of radiation pressure to control of interferometer test masses. The demonstration of radiation pressure control by Corbitt et al. showed that the method has a very strong promise [18]. We seek to extend radiation pressure control to two and possibly three degrees of freedom for use in gravitational wave detectors [19].

There is a significant radiation pressure effect called the Sidels-Sigg instability, which describes the coupling of two mirrors in a Fabry-Perot cavity via radiation pressure [1]. This sets a lower limit on the required angular control bandwidth. As laser power increases, this inevitably results in higher noise contamination by angular control noise. Angular optical trapping can damp the relative motion of test masses and control the Sidles-Sigg instability. Its fundamental noise limit is quantum radiation pressure noise, making it a promising candidate for low-noise angular control.

6.2 Optical Springs

In this chapter, we will discuss the control of a mirror using two pairs of optical springs, creating two stable degrees of freedom in a single mirror. One pair will be a executed in a straight cavity and one will be in a folded cavity. In a previous paper, we have derived the behavior of a single optical spring in a straight cavity:

$$K_{OS} \approx P_0 t_1^2 \frac{8k}{c(1-r_1 r_2)^3} \frac{\frac{\delta}{\gamma}}{(1+\frac{\delta^2}{\gamma^2})} \frac{1}{1+\frac{\delta^2}{\gamma^2}-\frac{\Omega^2}{\gamma^2}+i2\frac{\Omega}{\gamma}}. \tag{6.1}$$

In section 6.6, we demonstrate the optical spring behavior of a folded cavity optical spring.

$$K_{OS} \approx P_0 t_1^2 \frac{32k}{c(1-(r_1 r_2)^2)^3} \frac{\frac{\delta}{\gamma}}{(1+\frac{\delta^2}{\gamma^2})} \frac{1}{1+\frac{\delta^2}{\gamma^2}-\frac{\Omega^2}{\gamma^2}+i2\frac{\Omega}{\gamma}}. \tag{6.2}$$

We note that the only differences between the two equations are a factor of four in the numerator and the change of $r_1 r_2$ to $(r_1 r_2)^2$ in the denominator.

Because these beams are exerting force on a single mirror, we expect some crosstalk between the straight optical spring pair and the folded optical spring pair. We have attempted to minimize this though our choice of spot locations on the mirror (see appendix A).

6.3 Setup

Our experiment (see fig. 39) uses a 2 Watt 1064 nm Nd:YAG laser. The laser beam is split into a carrier beam and a subcarrier beam, then the subcarrier is frequency shifted by a tunable amount, described in more detail in section IV of our previous paper [44]. The two beams are mode matched and spatially recombined (in opposite linear polarizations) in a Mach-Zehnder-style setup. The recombined beam is then split using an unpolarized beamsplitter into main and side beams. The main beam enters the straight cavity, while the side beam enters the folded cavity. Both polarizations of both beams are monitored in transmission and reflection.

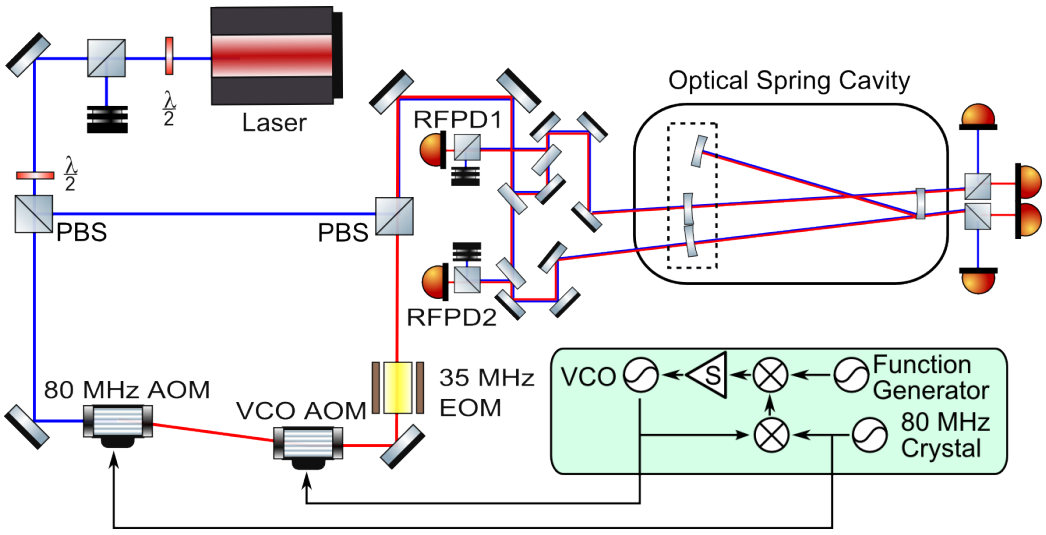

Figure 39 : Layout of the angular trap cavity experiment. The light from the laser is split into the carrier and subcarrier paths with a polarizing beam splitter (PBS), with a ratio determined by the $\lambda/2$ plate. The subcarrier path is frequency shifted by two AOMs under the control of the subcarrier servo then recombined with the carrier with another PBS. The co-aligned mode-matched beams are then split into main and side paths, which enter the trap cavity. The main beam has a straight optical path and is read out in transmission by broadband photodiodes and in reflection by RFPD1. The side beam has a folded optical path and is read out in transmission by broadband photodiodes and in reflection by RFPD2. We can use the 35 MHz modulation from the EOM with the two RFPDs in a PDH scheme to read out the cavity lengths or lock the cavities.

Parameter	Straight	Folded
λ_0	1064 nm	1064 nm
Mirror1,3,4 RoC	7.5 cm	7.5 cm
Mirror2 RoC	5.0 cm	5.0 cm
L_0	10.0 cm	20.0 cm
M1,3,4 Spot size	268 μm	268 μm
M2 Spot size	155 μm	155 μm
FSR	1.50 GHz	0.75 GHz
Finesse	7500	3750
Cavity Pole	98.6 kHz	98.6 kHz
Cavity angle, θ	0 deg	11 deg

Table 6 : Optical setup for the angular trap. The straight and folded cavities have different parameters due to the difference in total length and number of mirrors.

6.4 Results

We stably locked the main beam and achieved many concurrent two-second locks on the side beam using a transmitted power offset lock.

We could not extend the locks of the side cavity for longer periods due to a technical complication that I will describe below. We do not think that this is a fundamental problem. In the following subsections, I describe a few challenges, resolutions, and options for the further pursuit of side locking.

6.4.1 Angular loop bandwidth

The expectation was that we could lock the angular cavity after we locked the main cavity by pushing on the yaw of the optics. Based on a calculation of range for the small optic, we could change the cavity length by $\lambda/2$ or one FSR by rotating the small optic about 20 μ rad. The difficulty came in the bandwidth required to lock the side cavity.

Pushing on the yaw of the large optic results in a cavity length change of 2.9 $\mu m/mrad$, which means one FSR is about 190 μrad. This is due to the fact that you only change the length by the difference in the distance between the two side mirrors and the center of mass in the input coupler. This means that we have a factor of 10

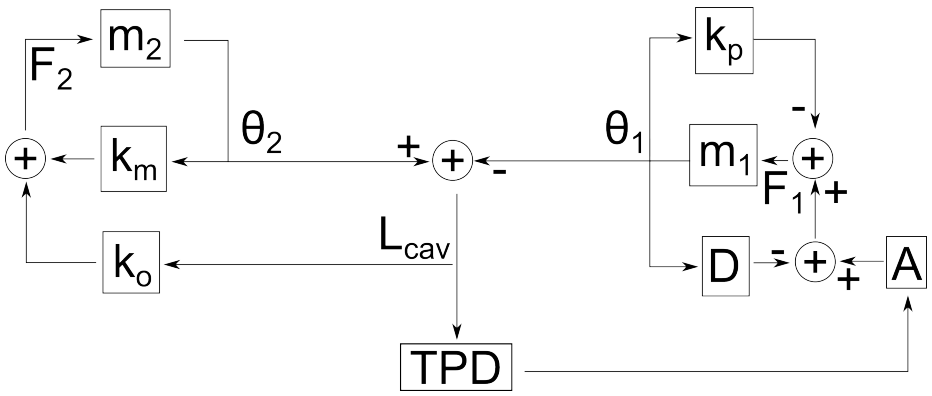

Figure 40 : Control loop structure for side cavity. Transmitted power is fed into yaw control for the input coupler.

lower gain in feedback to the large mirror yaw, compared to that of the small mirror yaw.

Both optics have a yaw resonance around 1 Hz. The small mirror also has a yaw resonance around 22 Hz. The more troubling thing is that something rings up in yaw around 66 Hz when we lock the side cavity. We are running out of range and the cavity loses lock. See figs 41 and 42.

We think that the 66 Hz oscillation is a yaw mode of the ring suspension but it does not show up in the OSEMs. There are hints of the oscillation in the yaw optical lever signal after the resonance is rung up, so we should be able to clean up that signal and might be able to use that for damping feedback.

6.4.2 Resolving bandwidth issues

The biggest concern is to increase the bandwidth of the feedback system, so that we can damp this and other high-frequency modes. There are several approaches that could work. They are given in order of increasing invasiveness.

Optical spring behavior

By design, the small mirror is very strongly affected by radiation pressure. We could use this to our advantage, creating a stable optical spring to damp the motion. Otherwise, we could turn down the laser power or further detune it to reduce the energy

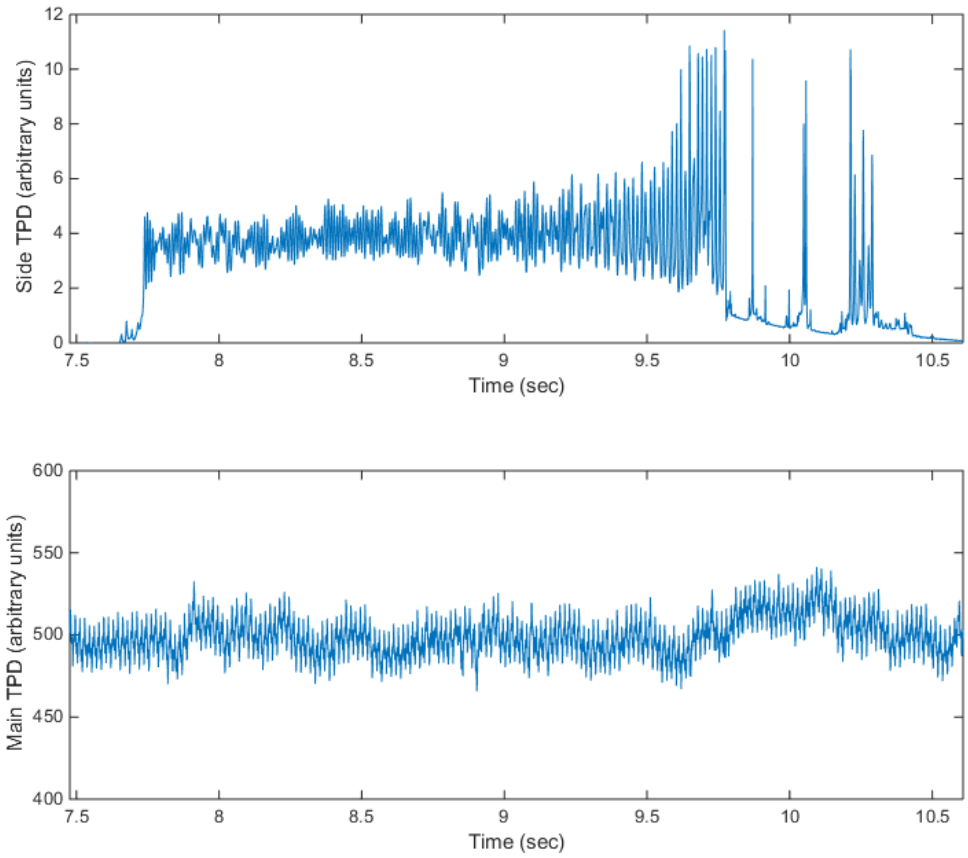

Figure 41 : Using a transmission power offset lock, we were able to temporarily achieve a concurrent lock of the main and side cavities. However, a yaw resonance in the small mirror suspension at about 66 Hz consistently rang up. Without enough control loop bandwidth, we could not damp this motion.

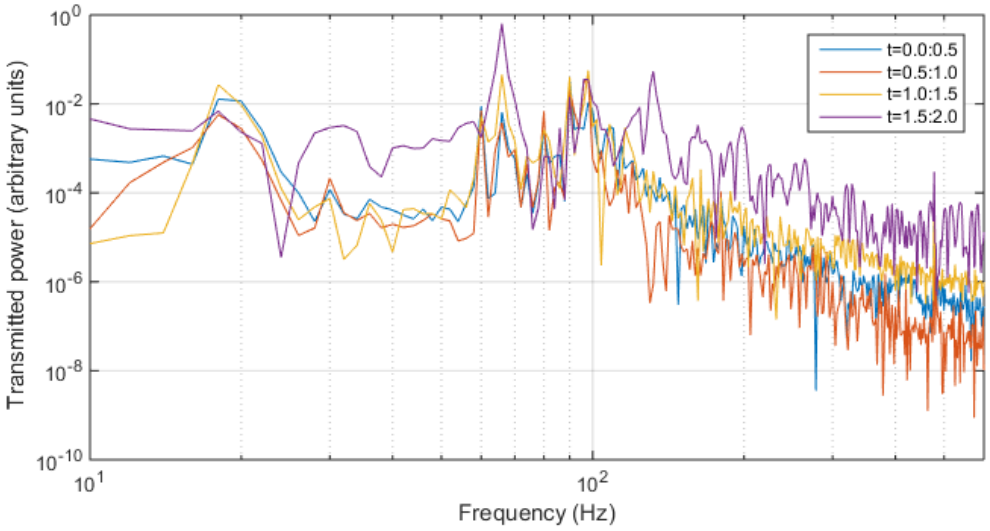

Figure 42 : Spectrum of the two second lock shown in fig 41. The four traces for show spectra taken every 0.5 seconds from $t = 0$ to $t = 2.0$ The line at 66 Hz rings up over time. In the last trace, we can see the harmonics of 66 Hz also rung up.

coupling into the 66 Hz mode.

Improve OSEM diagonalization

By improving the diagonalization in the two suspensions, we can reduce the amount of the dynamic range devoted to stabilizing the optics with respect to the suspensions and also possibly reduce the required bandwidth for the main cavity lock. This would free up more dynamic range for the side cavity lock.

Inter-cavity coupling

We saw a fair amount of power couple from the main cavity into the side cavity. This is probably caused by clipping or another source of scatter. This was temporarily fixed by changing the polarization of the side beam relative to that of the main beam, but this is not a good long-term solution, because the introduction of the carrier beam into the cavity will presumably cause carrier-to-subcarrier coupling for separate beams with the same polarization.

Install AOM

An AOM in a double-pass configuration could be used to actuate on one of the two paths, essentially introducing a variable frequency drive. We can get up to ±30 MHz of actuation using a double-passed AOM, which should be plenty to cover the cavity pole (about 100 kHz). The significant challenge would lie in the behavior of the two different polarizations (carrier and subcarrier) in the AOM, which could lead to unacceptable losses. This could be used for higher frequency feedback.

Additional laser

Setting up an entirely separate path would be the best way to guarantee that the side cavity could be locked, but it would require a lot of time and funds.

6.5 Noise sources

There are four main players in this game: The laser beam, the suspensions, the small mirror, and the seismic noise that couples into the system. The interactions between these components result in the vast majority of the noise that we expect to see in the output.

6.5.1 Quantum Noise

Quantum noise is unavoidable (though reducible via squeezing) in optical experiments. The radiation pressure force F_{RP} on the small mirror due to a laser with power P can be written $F_{RP} = 2P/c$. Quantum fluctuations ΔP in that power cause a fluctuating force on the mirror which results in unwanted motion of that mirror. Thus we see that

$$\Delta x = \frac{2\Delta P}{mc\left(-\omega^2 + \omega_0^2 + \frac{i\omega\omega_0}{Q}\right)}. \tag{6.3}$$

Two different things can affect the fluctuation in power. Fundamentally, the shot noise in the system causes fluctuation. Practically, the laser has some intensity noise that we can filter (using for instance the ISS), but we are nonetheless subject to. The

product manual says that the intensity noise should be less than 0.1% of the RMS power between 10 Hz and 2 MHz. With the "noiseater" option, we should be getting about -150 dB/$\sqrt{\text{Hz}}$ RIN (relative intensity noise). This is about the same level as the shot noise. The shot noise inside the cavity is given by

$$\Delta P_{sn} = G\sqrt{\frac{2hcP_{in}}{\lambda}} \tag{6.4}$$

where P_{in} is the power entering the cavity, and G is the gain factor determined by the transmission and reflection coefficients of the two cavity mirrors.

$$\sqrt{G} = t_1 e^{\frac{\imath\omega L}{c}} + t_1 r_1 r_2 e^{3\frac{\imath\omega L}{c}} \ldots = \frac{t_1 e^{\frac{\imath\omega L}{c}}}{1 - r_1 r_2 e^{2\frac{\imath\omega L}{c}}}. \tag{6.5}$$

We combine the shot noise for the positively and negatively detuned beams to get the total.

The motion caused by radiation pressure noise is also damped by the optical spring, so we multiply our answer by the closed-loop gain of the spring-pendulum system.

Shot noise itself also plays a role in our measurement. Our most accurate measurement of the small mirror motion is the PDH signal from the beam reflected by the cavity (because the sidebands are far from the cavity resonance). By sweeping the mirror position, knowing the free spectral range (FSR) of our cavity, we can calibrate the PDH error signal to give us the change in the length of the cavity over time.

This measurement is limited by the quantum efficiency of the photodiode and the shot noise of the incoming light. This shot noise is a function of the reflected power from the cavity.

It is important to note that this noise should not change the system, only hinder our ability to measure the system (unless we decide to feed back on the PDH signal).

$$P_{ref} = P_{in}\left[r_1 - \frac{t_1^2 r_2 e^{2\imath\frac{\omega L}{c}}}{1 - r_1 r_2 e^{2\imath\frac{\omega L}{c}}}\right]^2. \tag{6.6}$$

The above is the power reflected from a cavity. Calculating this value for the carrier and subcarrier beams gives us the total reflected power.

The shot noise is given by [56]

$$S_P = \sqrt{\frac{2hcP_{ref}}{\lambda}}. \tag{6.7}$$

We can express this as position noise of a Fabry-Perot cavity due to shot noise using the calibration of power to length in the reflected beam.

$$S_L = \frac{\sqrt{hc}}{8}\frac{\sqrt{\lambda}}{F\sqrt{P_c}}. \tag{6.8}$$

In this equation, P_c is the power in the carrier field; using the reflected power is a reasonable approximation. F is the cavity finesse. The calculated shot noise is several orders of magnitude below the dominant noise sources, so we shouldn't have to worry about it too much. This effect could be increased if the carrier field of the beam was lower.

We see a position noise due to the fundamental limits on our measurement. Referred shot noise should just be inverse filtered by the cavity pole (but we do not see it because our cavity pole is much higher than our experiment bandwidth).

6.5.2 Frequency Noise

Fundamentally, the optical spring sees small fluctuations in laser frequency and small fluctuations in the cavity length as the same thing: a change in the detuning of the laser from the cavity resonance. This means that laser frequency noise can be a significant contributor to the 'motion' seen by the spring, but it also means that the optical spring will move the cavity length to counteract changes in the laser frequency.

We know the frequency noise of the laser from the datasheet [1]. We can convert frequency noise to a position noise because we know the free spectral range (FSR) of the cavity and the wavelength; changing the frequency by one FSR is equivalent to moving the end mirror one wavelength. We have to consider the round trip path for the laser, which introduces the factor of 2 in the denominator.

$$x_f n = \delta f \frac{\lambda}{2FSR}. \tag{6.9}$$

[1] Coherent, *Mephisto* coherent.com/downloads/Mephisto_DS_1013revA_2.pdf

This is the apparent motion that would be introduced into an undamped cavity. Because this cavity can react to the change in frequency, the effect is reduced by the closed loop gain of the optical spring system.

6.5.3 Thermal Noise

Thermal noise is broken up into two subsections: mirror and suspension.

For a suspension, we have to consider the dissipative/damping parts (because anywhere energy gets out, it can also get in!).

We'll be using a version of the Fluctuation-Dissipation Theorem:

$$x^2_{therm}(f) = \frac{4k_BT}{\omega^2}\Re(Z^{-1}(f)). \tag{6.10}$$

Where $\Re(Z^{-1}(f))$ is the real part of the inverse of the impedance Z of the system. It is defined by the relation $F_{ext} = Z(f)v(f)$. In other words, it's a measure of the force required to give your system a velocity v. Thus we find

$$\left(\frac{i\omega x}{F}\right)^{-1} \equiv Z = b + i\omega m - \frac{ik}{\omega} \tag{6.11}$$

$$Z^{-1} = \frac{b + i(k/\omega - m\omega)}{b^2 + (m\omega - k/\omega)^2}. \tag{6.12}$$

At this point I should point out that we need to be careful about the difference between k, the effective spring constant of the small mass suspension, and k_B, Boltzmann's constant. Combining Eqns. (6.10) and (6.12) gives us an equation for the suspension thermal noise. We're using the values for the position mode of the small suspension: $f_0 = 14.1$ Hz and $Q \approx 200$. This value for Q may be too low (which could lead to a lower-than-predicted thermal suspension noise).

$$x_{therm} = \frac{F_{therm}}{-m\omega^2} = \sqrt{\frac{4k_BTb}{\omega^2(b^2 + (\omega m - k/\omega)^2)}}. \tag{6.13}$$

The mirror noise (including the coating and internal modes) is harder to predict, because the specifications on the coating are not freely given by the manufacturer. I use the parameters for coating materials from Stefan Ballmer's angular trap proposal

document. The dominant noise (determined using GWINC[2]) in the frequency range of interest is the coating Brownian noise. I have used the `getCoatBrownian` function from GWINC to plot it.

6.5.4 Seismic noise

To calculate the seismic noise, we have to start with a spectrum measured in lab. After that, we apply the transfer functions of the suspensions and the closed loop gain of the OSEM loops to get a good idea of how much noise we'll see. We are curious mostly about position and bounce modes of vibration. The position obviously concerns the trap, but the bounce modes of the two suspensions are distinct and very close to a strong peak in the Syracuse University seismic spectrum. Unchecked, the seismic noise peak drives up the bounce modes, making the cavity unlockable. The bounce mode can also couple to position through the pitch mode. We have reduced this bounce mode by building small blade springs and fitting them to the top of the suspension, giving vertical isolation above 7 Hz. We have implemented a feedback loop in the digital system to control the 7 Hz resonance via the bounce-to-pitch coupling.

6.5.5 OSEMs

Optical sensing electromagnets (OSEMs) are used in our experiment to position the large mirror and the ring supporting the small mirror. We have glued small magnets onto the back side of the large mass and the ring. We sense the position of these magnets using pairs of LEDs and photodiodes in a 'shadow sensor' configuration. We feed this signal through a control loop, then actuate on a coil surrounding the shadow sensor. These devices are limited by the shot noise of the shadow sensor. We can calculate the effect of this noise on the mirror by multiplying the sensing noise by the position loop closed loop transfer function and the glass fiber suspension transfer function. This seems to be somewhat limiting right now. It may be beneficial to change the loop.

[2] awiki.ligo-wa.caltech.edu/aLIGO/GWINC

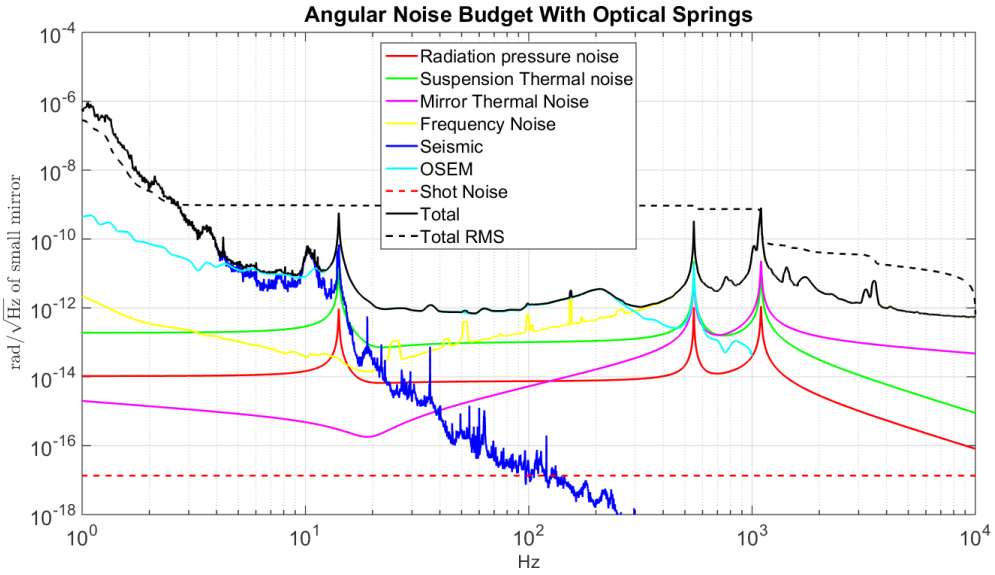

Figure 43 : Expected noise budget for the angular trap. The noises associated with mirror position motion or frequency noise are damped by an expected optical spring. At low frequencies, the total noise is dominated by seismic noise. Starting around 10 Hz, we see the effects of OSEM noise and laser frequency noise dominating the noise spectrum. At very high frequencies, we see the effects of thermal noise at the resonant frequencies of the optical springs.

6.6 Folded cavity optical spring derivation

To determine the behavior of a folded optical spring, we can compare it to the standard optical spring derivation [3].

We begin with a folded cavity with three mirrors, shown in fig. 44. We assume that M3 and M4 have the same amplitude reflectivity as M1, r_1, while we allow the end mirror to have a different reflectivity, r_2. The incoming field is $E = e^{\frac{i2\pi ct}{\lambda}}$. The average round-trip path length is $L = 2L_0$, where L_0 is the optical patch length between mirrors M3 and M4. We consider microscopic changes in cavity length d_n, which are discreet samples of a harmonic oscillation $d(t) = x_0 e^{i\Omega t}$. The light travel time between M3 and M4 is $\tau = \frac{L_0}{c}$. It is important to note that the cavity length L_0 of the folded cavity is twice that of the straight cavity in our experiment.

We can use the same X and Y notation as the original derivation in Chapter 2 with one small change. $Y = e^{-i\Omega 2\tau}$ is the same, but now $X = (r_1 r_2)^2 e^{\frac{-i2\pi L}{\lambda}}$ because the optical path touches M3 and M4 once and M2 twice.

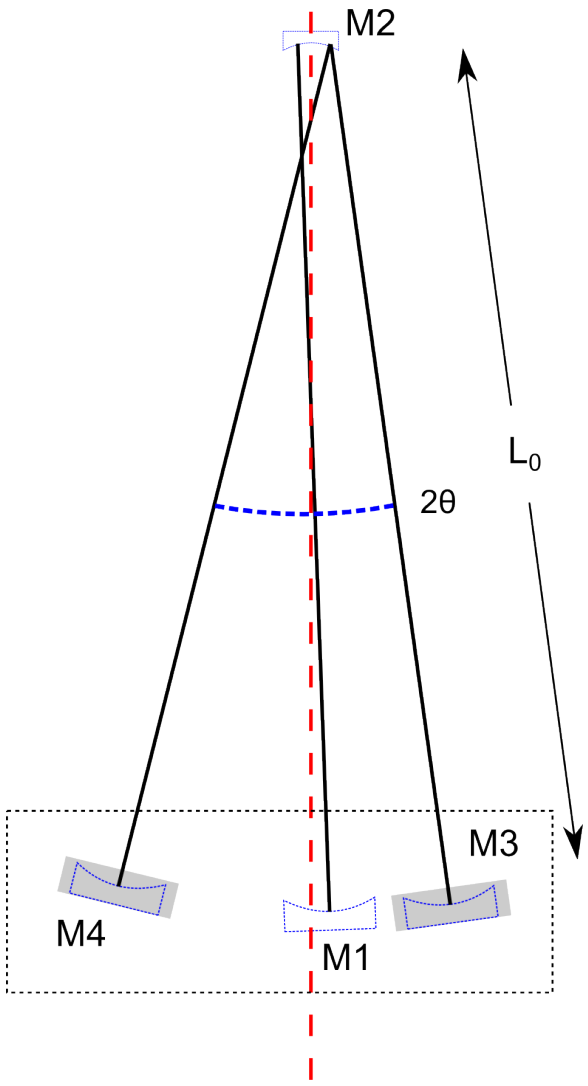

Figure 44 : Layout of the angular trap cavity. Light enters through mirrors M1 and M3. The angle θ of the folded cavity is measured from the normal of M1.

We consider a set of displacements d_n, discretely sampled from a continuously oscillating function. This is equivalent to driving the cavity length at angular frequency Ω.

$$d(t) = x_0 e^{i\Omega(t-(2n-1)\tau)} \tag{6.14}$$

$$d_1 = x_0 e^{i\Omega(t-\tau)} \tag{6.15}$$

$$d_n = Y^{2n-2} d_1. \tag{6.16}$$

Following [3], we get an equation for the electric field in the cavity, which we must change to reflect that we can only have real values for d_1.

$$E_{tot} = \frac{t_1 E}{1-X}\left[1 - \frac{4i\pi d_1}{\lambda}\frac{X}{1-Y^2X}\right]$$

$$E_{tot} = \frac{t_1 E}{1-X}\left[1 - \frac{4i\pi}{2\lambda}\left(\frac{d_1}{1-Y^2X} + \frac{\bar{d}_1}{1-\overline{Y}^2X}\right)\right]. \tag{6.17}$$

Then we get the cavity power:

$$P = E_{tot}\cdot\overline{E}_{tot} = -P_0 t^2\left[\frac{i2\pi Y}{\lambda(1-X)(1-\overline{X})}\left(\frac{X}{1-Y^2X} - \frac{\overline{X}}{1-Y^2\overline{X}}\right)\delta L + cc\right] \tag{6.18}$$

We add an extra $Y^{1/2}$ term to get to the other side of the cavity. It is important to note that the change in cavity length δL used here is strictly that: the cavity length. If we want to transpose that into longitudinal change, we need to multiply by a geometric factor (see fig. 44):

$$\delta L = \frac{2\delta z}{\cos(\theta)}. \tag{6.19}$$

There is similarly a geometric correction when calculating the radiation pressure force F_{rad}

$$F_{rad} = \frac{2r_2^2}{c}P(2\cos(\theta)) = -K_z\delta z \tag{6.20}$$

$$= \frac{2r_2^2}{c}(2\cos(\theta))P_0 t^2\left[\frac{i4\pi Y^{3/2}}{\lambda(1-X)(1-\overline{X})}\left(\frac{X}{1-Y^2X} - \frac{\overline{X}}{1-Y^2\overline{X}}\right)\frac{2\delta z}{\cos(\theta)} + cc\right].$$

thus

$$K_z = \frac{8r_2^2}{c} P_0 t^2 \frac{i4\pi Y^{3/2}}{\lambda(1-X)(1-\overline{X})} \left(\frac{X}{1-Y^2X} - \frac{\overline{X}}{1-Y^2\overline{X}} \right). \tag{6.21}$$

With detuning:

$$X \to X = (r_1 r_2)^2 e^{-i2\delta\tau}. \tag{6.22}$$

Here $\delta = \omega_0 - \omega_{res}$, the angular frequency detuning from the cavity resonance, $\omega_{res} = 2\pi nc/L$, and ω_0 is the frequency of the laser.

$$\begin{aligned} K_{OS} = \quad & -P_0 t^2 r_2^2 \frac{32i\pi e^{-\frac{3}{2}i\Omega\tau}}{\lambda c(1-(r_1r_2)^2 e^{i2\delta\tau})(1-(r_1r_2)^2 e^{-i2\delta\tau})} \times \\ & \left(\frac{(r_1r_2)^2 e^{-i\delta\tau}}{1-(r_1r_2)^2 e^{-2i\Omega\tau} e^{-i2\delta\tau}} - \frac{(r_1r_2)^2 e^{i2\delta\tau}}{1-(r_1r_2)^2 e^{-2i\Omega\tau} e^{i2\delta\tau}} \right). \end{aligned} \tag{6.23}$$

The finesse for the folded cavity is $F = \pi \frac{FSR}{\gamma} \approx \frac{\pi}{1-(r_1r_2)^2}$, which is half that for a straight cavity using the same mirrors. Since the FSR is also half of that for the straight cavity, γ is the same here as it is for the longitudinal trap.

$$K_{OS} \approx P_0 t_1^2 \frac{32k}{c(1-(r_1r_2)^2)^3} \frac{\frac{\delta}{\gamma}}{(1+\frac{\delta^2}{\gamma^2})} \frac{1}{1+\frac{\delta^2}{\gamma^2} - \frac{\Omega^2}{\gamma^2} + i2\frac{\Omega}{\gamma}}. \tag{6.24}$$

Comparing this result to the same result for a straight cavity (Eq. 6.1), we see that the folded cavity spring constant is four times larger in magnitude than a similar straight cavity, and there is a change of $r_1 r_2$ to $(r_1 r_2)^2$.

Chapter 7

Application

7.1 Motivation

Angular control in LIGO is an important contribution to the noise budget at the frequencies of highest sensitivity [57].

There are four different angular modes for the two Fabry-Perot arms in the LIGO interferometer, shown in figure 45. The two hard modes are stable as the power increases, which means that the radiation pressure will push the mirrors back to an equilibrium position. The two soft modes are unstable as the power increases, pushing the mirrors away from equilibrium. Despite being stable, the hard modes still exhibit a resonant behavior that will need to be damped.

Angular noise can couple in to differential arm length (DARM) though the interaction between beam spot motion (BSM) and angular motion (θ) on mirrors. This happens in two ways: both a static offset in the BSM with mirror angular noise and a static angular offset with BSM noise can create DARM noise.

$$\hat{\Delta L}(f) = \hat{d}_{spot}(f) * \hat{\theta}_{Mirror}(f) \approx \hat{d}_{spot}(f) * \theta^{RMS}_{Mirror}(f) + d^{RMS}_{spot}(f) * \hat{\theta}_{Mirror}(f) \quad (7.1)$$

Barsotti and Evans showed that in Science Mode, angular noise from Common Soft and Differential Soft (the two modes of the arms that are unstable at high power) contribute the most to DARM noise. They also showed that in the final design of aLIGO, the soft mode is unstable with frequencies of -.17 and -.21 Hz for pitch and yaw, respectively. The control systems currently used for angular control must be

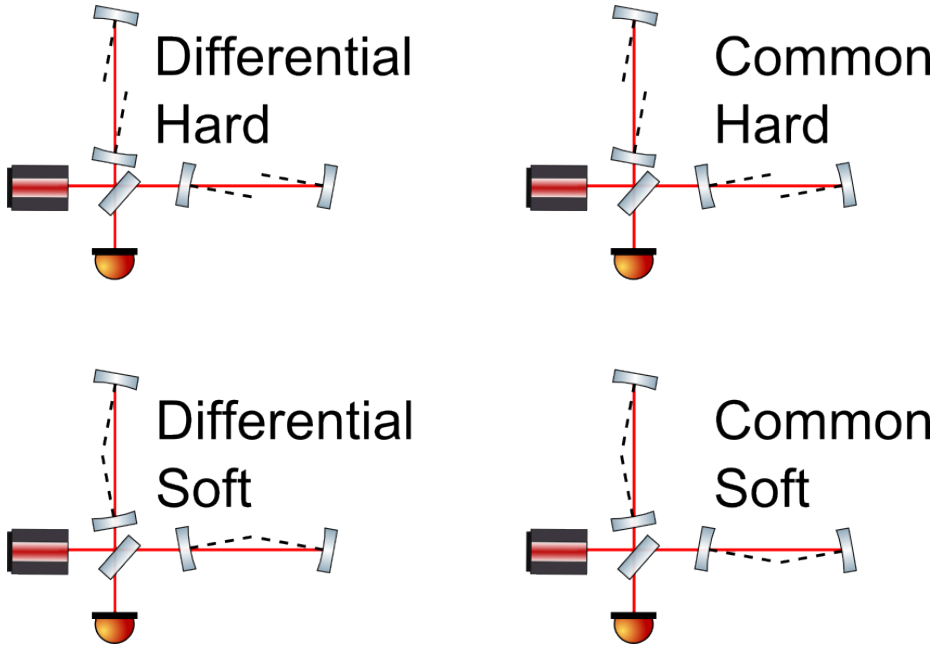

Figure 45 : The four Sidles-sigg modes of the Fabry-Perot cavities in LIGO. The two hard modes are stable and the two soft modes are unstable. All of modes must be damped with control loops.

used to damp the unstable modes and the resonances of the stable modes, which leads to injected sensing noise. For an optical angular control system to be useful, it must provide damping in that frequency range to stabilize the modes.

Using angular trapping methods, we can reduce the sensing noise injection by damping the angular motion $\hat{\theta}_{Mirror}(f)$.

7.2 Applying angular control

For our discussion, we will disregard the distinction between common and differential modes of the interferometer.

7.2.1 Single spring 4km damping

If we assume that the length will be stabilized with the main beam of the interferometer, we only really need to control the angular motion. We will consider only the yaw of the mirrors for this exploration, but there should not be any obstacles to applying the method to both pitch and yaw.

It seems like we could do this with a single folded cavity (see fig 46). In this configuration, ETMs and ITMs would have 'Buddy' mirrors attached to the sides to create an angular optical spring cavity.

This has several benefits that look quite appealing. The yaw of the ETM is damped relative to the ITM. If implemented ideally, the radiation pressure will be independent of small angular motions of the ETM. This particular configuration (see table 8 has a UGF of about 8 Hz, so it should also damp the hard mode (Barsotti and Evans give a hard mode frequency of 3.05 Hz). This would also, as a byproduct, give a very sensitive readout of the yaw of the ETM via the PDH error signal.

There are several concerns that would need to be addressed. This configuration could actively couple angular noise in the ITM into length noise at the ETM. It would also require massive engineering changes to manufacture and align a monolithic test mass with Buddy mirrors bonded onto the sides. These mirrors would also need to be very carefully manufactured and attached, because the cavity could not be realigned once assembled.

The design has to be careful of losses due to long-storage-time optical cavities[58], but the finesse is low enough in this configuration ($F = 7850$) to avoid a significant impact from the effects. The design also has the potential to introduce increased thermal noise to the length degree of freedom, due to the added buddy mirrors. We have neglected the thermal noise effects in this analysis, but it should be addressed.

Parameter	**Metric**
Cavity round-trip length, $4L$	16 Km
Buddy Mirror power transmission, T1,T2	200 ppm
Buddy Mirror power absorption, T1, T2	2 ppm
Buddy Diameter D	15 cm
Buddy Thickness t	10 cm
Buddy ROC	3.5 km
Cavity FSR	18.7 kHz
Cavity Finesse	7850

Table 7 : Characteristics of proposed angular design. The transmissivity and absorption values are easily achievable with current dielectric coatings.

Table 8 lists the parameters for a possible optical spring design. If we lock the

Parameter	**Metric**
Carrier input power P_c	6 W
Subcarrier input power P_s	.15 W
Carrier Detuning df_c	19 Hz
Subcarrier Detuning df_s	-5 Hz
OS Angle θ	62.5 μrad
OLG UGF	7.9 Hz
Phase at UGF	-169.3 deg

Table 8 : Characteristics of proposed angular optical spring. The relatively low power (about 6 watts) is easily achievable. The detunings will require careful design because they are very small.

laser to the frequency of the main cavity laser, we can take advantage of the fantastic frequency stabilization of a 4 km cavity, and also remove the common mode length noise of associated with relative frequency fluctuations. The very small frequency detunings would still present a significant challenge to implement and maintain.

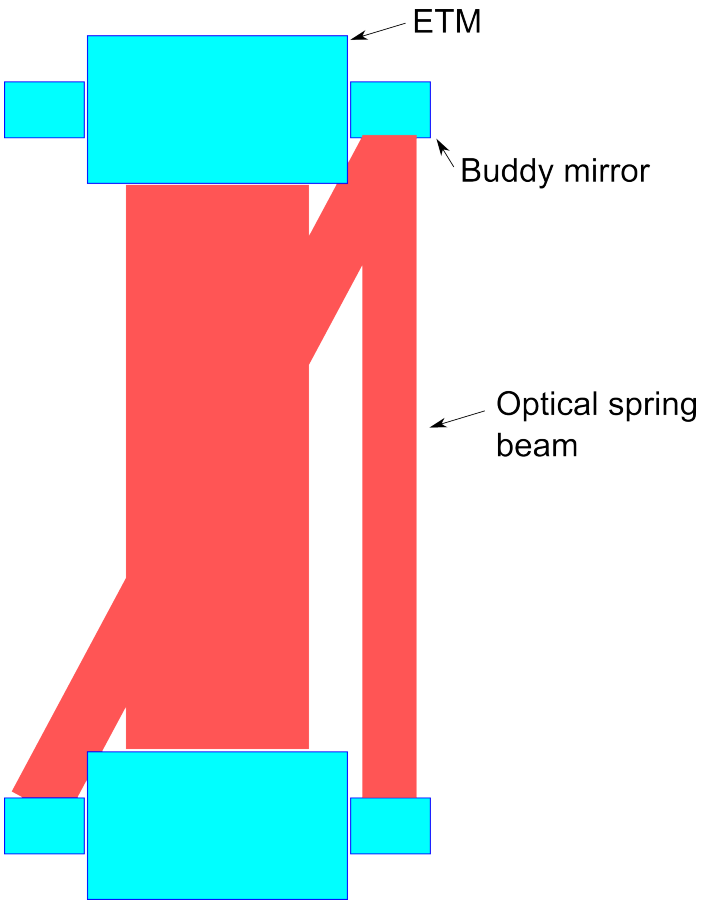

Figure 46 : Diagram of a folded cavity 4km angular control scheme. This configuration relies on 'Buddy' mirrors attached to the side of the test masses.

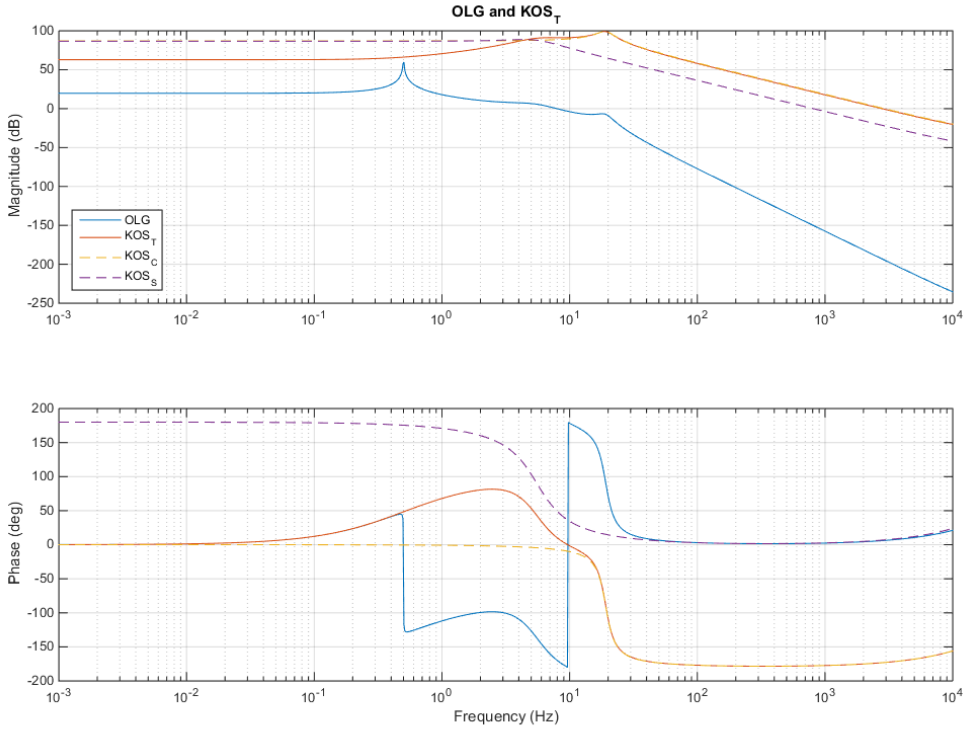

Figure 47 : Open loop gain (OLG) of the angular control scheme and optical springs. The optical springs shown are the carrier and subcarrier optical spring constants (KOS_C and KOS_S) and the total optical spring (KOS_T).

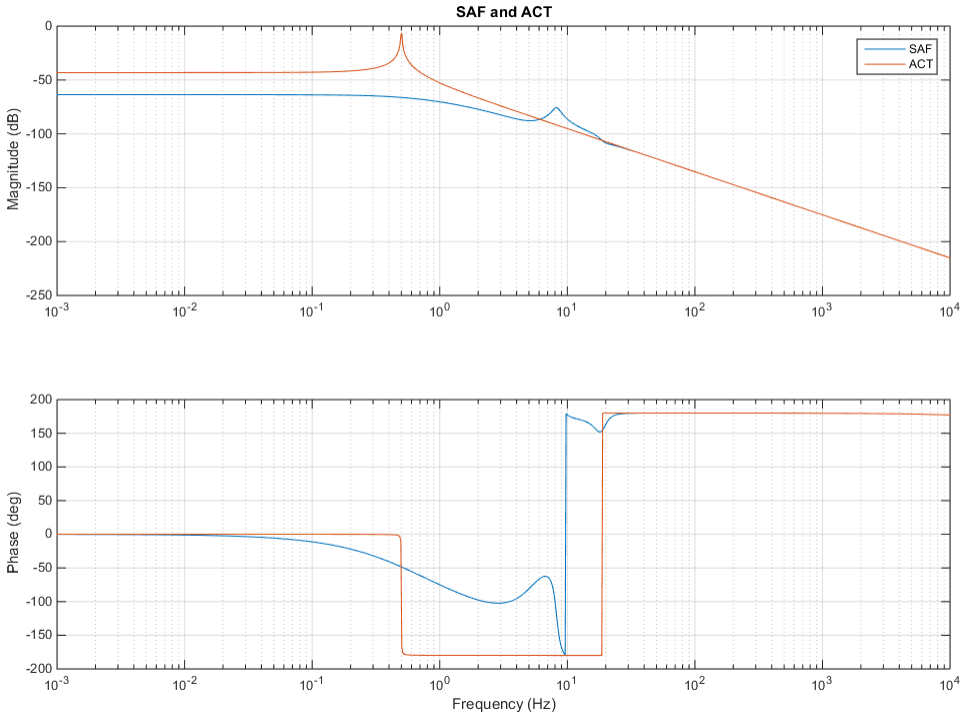

Figure 48 : The actuation function (ACF) and spring actuation function ($SAF = CLG \times ACF$) of the proposed angular control scheme. The actuation function includes the yaw pendulum behavior ($1/f^2$) of the mass and the yaw resonant frequency (chosen to be 0.5 Hz) of the ETM.

Chapter 8

Conclusion

8.1 Summary

aLIGO has begun taking data and will achieve design sensitivity over the next few years. At that point, the next generation of upgrades and improvements must be nearly ready to implement. One possible such upgrade would be to damp the unwanted angular motion in the test masses using radiation pressure feedback. This has the potential benefits of reducing the angular noise of the system and thus also reducing the amount of noise that couples from angular motion into cavity length.

We have explored the implementation and uses of radiation pressure feedback, optical springs, to control the motion of a mirror. We demonstrated in several ways the underlying principles and behavior of optical springs, in both straight and folded cavities. We discussed the mechanical design of the experiment, with the addition of blade springs to reduce the influence of seismic noise on the experiment. We reviewed the feedback and controls in use for the optical traps. We measured and modeled the causes and effects of the photothermal effect in an optical spring system. We explored one- and two-degree-of-freedom traps, and, while we could not get the angular trap stably locked for more than two seconds, we have laid out the path to do so. We designed and modeled a full-scale implementation of angular optical springs to damp the Sidles-Sigg instability in the aLIGO configuration.

These developments should lay a strong groundwork for continued research into the applications and uses of radiation pressure feedback in aLIGO and beyond.

8.2 Future work

There are several things left unfinished that will hopefully deliver interesting results:

1. Improving the stability of the SU angular optical trap experiment and damping the 66 Hz resonance that seems to be preventing extended locks. There are a number of possibilities to increase the bandwidth and damp the motion outlined in Section 6.4.2.

2. Exploring the possibility of a a single stable optical spring with a specialized optical coating. We expect that dielectric coating manufacturers could do a custom run with a very thick first layer to create a "self-locking" cavity. The mirror could be mounted using the same cold weld method described in Section 3.2, then tested with the single-mirror input coupler from Chapter 5.

3. Designing and demonstrating a large scale angular trap in aLIGO. A detailed noise budget needs to be drafted using a modified version of GWINC or a similar tool to insure that we would not be introducing too much thermal noise. After that, a prototype of the design would need to be built at e.g. the Caltech 40 m interferometer to develop control systems and test predictions.

Appendix A

Beam Separation

A.1 Definitions

- P_m Input power of the main beam
- P_s Input power of the side beam
- f_m Main cavity finesse
- f_s Side cavity finesse
- R_c Radius of curvature of payload mirror (5 cm)
- θ_m Main beam angle from optical axis. Origin is at center of curvature.
- θ_s Side beam angle from optical axis. Origin is at center of curvature.
- c Speed of light
- R Payload mirror radius
- h Payload mirror thickness
- m Payload mirror mass
- $I = \frac{m}{12}(3R^2 + h^2)$ Payload mirror moment of inertia
- $G = \frac{P_m f_m}{P_s f_s}$ Handy constant
- $d = \theta_m R_c - \theta_s R_c$ Beam spot seperation

A.2 Balancing torques

We want the mirror to be stationary, so the net torque on the mirror should be zero.

Force on payload mirror due to radiation pressure of the two beams:

$$F_m = \frac{2P_m f_m}{c} \qquad F_s = \frac{2P_s f_s}{c}$$

$$\tau = F_m \theta_m R_c + F_s \theta_s R_c = 0$$

substituting in d,

$$\theta_m = \frac{d}{R_c(1+G)}$$

A.3 Eliminating beam coupling

We propose that there is a spot somewhere on the surface of the payload mirror where the sum of torque and force due to one beam makes the net force zero. We place one beam spot at r_1. We'd like to put the other beam in the null spot r_2 so that there is no force coupling between the two.

$$Fs = \frac{2P_s f_s}{c} = m\omega^2 x \qquad x = \frac{F_s}{m\omega^2}$$
$$\tau_s = F_s r_1 = I\omega^2 \phi \qquad \phi = \frac{F_s r_1}{I\omega^2}$$

Let's find a point these effects cancel:

$$r_2\phi - x = 0 \qquad r_2 = \frac{x}{\phi} = \frac{I}{mr_1}$$

It should be noted that the previously used d can also be expressed as $d = r_2 - r_1$.

$$r_2 = \theta_2 R_c = \theta_m R_c$$

$$r_2 = \frac{d}{1+G}$$

$$\frac{I}{m} = \frac{(r_2 - r_1)r_1}{1+G} = \frac{\left(\frac{I}{mr_1} + r_1\right) r_1}{1+G}$$

$$r_1 = \sqrt{\frac{I}{mG}} \qquad r_2 = \sqrt{\frac{IG}{m}}$$

These radii are the ideal horizontal distances from the payload mirror optical axis to the beam spots.

Bibliography

[1] J.A. Sidles and D. Sigg. Optical torques in suspended fabryperot interferometers. *Phys. Lett. A*, 354(3):167 – 172, 2006.

[2] A.E. Siegman. *Lasers*. University Science Books, 1986.

[3] A. Perreca, J. Lough, D. Kelley, and S. W. Ballmer. Multidimensional optical trapping of a mirror. *Phys. Rev. D*, 89(12):122002, June 2014.

[4] B. P. Abbott, R. Abbott, R. Adhikari, P. Ajith, B. Allen, G. Allen, R. S. Amin, S. B. Anderson, W. G. Anderson, M. A. Arain, and et al. LIGO: the Laser Interferometer Gravitational-Wave Observatory. *Rep. Prog. Phys.*, 72(7):076901, 2009.

[5] J. R. Smith and LIGO Scientific Collaboration. The path to the enhanced and advanced LIGO gravitational-wave detectors. *Classical Quantum Gravity*, 26(11):114013, 2009.

[6] G. M. Harry and LIGO Scientific Collaboration. Advanced LIGO: the next generation of gravitational wave detectors. *Classical and Quantum Gravity*, 27(8):084006, April 2010.

[7] Giovanni Losurdo. Ground-based gravitational wave interferometric detectors of the first and second generation: an overview. *Classical Quantum Gravity*, 29(12):124005, 2012.

[8] C. M. Caves. Quantum-Mechanical Radiation-Pressure Fluctuations in an Interferometer. *Phys. Rev. Lett.*, 45:75–79, 1980.

[9] W.-T. Ni. Quantum measurements and the standard quantum limit. *Phys. Rev. A*, 33:2225–2229, 1986.

[10] S. L. Danilishin and F. Y. Khalili. Quantum Measurement Theory in Gravitational-Wave Detectors. *Living Rev. Relativity*, 15:5, 2012.

[11] Y. Chen. Macroscopic quantum mechanics: theory and experimental concepts of optomechanics. *J. Phys. B*, 46(10):104001, 2013.

[12] LIGO Document. Report No LIGO-T1000416-v3, 2010.

[13] V. B. Braginsky, S. E. Strigin, and S. P. Vyatchanin. Analysis of parametric oscillatory instability in power recycled LIGO interferometer. *Phys. Lett. A*, 305:111–124, 2002.

[14] O. Arcizet, T. Briant, A. Heidmann, and M. Pinard. Beating quantum limits in an optomechanical sensor by cavity detuning. *Phys. Rev. A*, 73(3):033819, 2006.

[15] T. Corbitt, D. Ottaway, E. Innerhofer, J. Pelc, and N. Mavalvala. Measurement of radiation-pressure-induced optomechanical dynamics in a suspended Fabry-Perot cavity. *Phys. Rev. A*, 74(2):021802, 2006.

[16] T. J. Kippenberg, H. Rokhsari, T. Carmon, A. Scherer, and K. J. Vahala. Analysis of Radiation-Pressure Induced Mechanical Oscillation of an Optical Microcavity. *Phys. Rev. Lett.*, 95(3):033901, 2005.

[17] B. S. Sheard, M. B. Gray, C. M. Mow-Lowry, D. E. McClelland, and S. E. Whitcomb. Observation and characterization of an optical spring. *Phys. Rev. A*, 69(5):051801, 2004.

[18] Thomas Corbitt, Yanbei Chen, Edith Innerhofer, Helge Müller-Ebhardt, David Ottaway, Henning Rehbein, Daniel Sigg, Stanley Whitcomb, Christopher Wipf, and Nergis Mavalvala. An all-optical trap for a gram-scale mirror. *Phys. Rev. Lett.*, 98:150802, 2007.

[19] M. Punturo and et al. The third generation of gravitational wave observatories and their science reach. *Classical Quantum Gravity*, 27(8):084007, 2010.

[20] V.B. Braginsky, S.E. Strigin, and S.P. Vyatchanin. Parametric oscillatory instability in FabryPerot interferometer. *Phys. Lett. A*, 287(56):331 – 338, 2001.

[21] Katherine L. Dooley, Lisa Barsotti, Rana X. Adhikari, Matthew Evans, Tobin T. Fricke, Peter Fritschel, Valera Frolov, Keita Kawabe, and Nicolás Smith-Lefebvre. Angular control of optical cavities in a radiation-pressure-dominated regime: the enhanced ligo case. *J. Opt. Soc. Am. A*, 30(12):2618–2626, 2013.

[22] Eiichi Hirose, Keita Kawabe, Daniel Sigg, Rana Adhikari, and Peter R. Saulson. Angular instability due to radiation pressure in the ligo gravitational-wave detector. *Appl. Opt.*, 49(18):3474–3484, 2010.

[23] C. Genes, D. Vitali, P. Tombesi, S. Gigan, and M. Aspelmeyer. Ground-state cooling of a micromechanical oscillator: Comparing cold damping and cavity-assisted cooling schemes. *Phys. Rev. A*, 77(3):033804, 2008.

[24] J. D. Teufel, T. Donner, D. Li, J. W. Harlow, M. S. Allman, K. Cicak, A. J. Sirois, J. D. Whittaker, K. W. Lehnert, and R. W. Simmonds. Sideband cooling of micromechanical motion to the quantum ground state. *Nature*, 475:359–363, 2011.

[25] A. D. O'Connell, M. Hofheinz, M. Ansmann, R. C. Bialczak, M. Lenander, E. Lucero, M. Neeley, D. Sank, H. Wang, M. Weides, J. Wenner, J. M. Martinis, and A. N. Cleland. Quantum ground state and single-phonon control of a mechanical resonator. *Nature*, 464:697–703, 2010.

[26] J. Chan, T. P. M. Alegre, A. H. Safavi-Naeini, J. T. Hill, A. Krause, S. Gröblacher, M. Aspelmeyer, and O. Painter. Laser cooling of a nanomechanical oscillator into its quantum ground state. *Nature*, 478:89–92, 2011.

[27] Thomas Corbitt, Christopher Wipf, Timothy Bodiya, David Ottaway, Daniel Sigg, Nicolas Smith, Stanley Whitcomb, and Nergis Mavalvala. Optical dilution and feedback cooling of a gram-scale oscillator to 6.9 mk. *Phys. Rev. Lett.*, 99:160801, 2007.

[28] N. Matsumoto, Y. Michimura, G. Hayase, Y. Aso, and K. Tsubono. Classical pendulum feels quantum back-action. *ArXiv Quantum Physics e-prints*, 2013.

[29] P. R. Saulson. Thermal noise in mechanical experiments. *Phys. Rev. D*, 42:2437–2445, 1990.

[30] A. L. Greensite. *Elements of modern control theory.* Spartan Books, New York, 1970.

[31] G. F. Franklin and A Powell, J. D. Emami-Naeini. *Elements of modern control theory.* Addison-Wesley, Reading, MA, 1994.

[32] V. B. Braginsky and S. P. Vyatchanin. Low quantum noise tranquilizer for Fabry-Perot interferometer. *Phys. Lett. A*, 293:228–234, 2002.

[33] S. W. Ballmer and D. J. Ottaway. New class of optical beams for large baseline interferometric gravitational wave detectors. *Phys. Rev. D*, 88(6):062004, 2013.

[34] A. E. Siegman. *Lasers.* University Science Books, Herndon, VA, 1986.

[35] E. D. Black. An introduction to Pound-Drever-Hall laser frequency stabilization. *Am. J. Phys.*, 69:79–87, 2001.

[36] N. Mavalvala. *Alignment Issues in Laser Interferometric Gravitational-Wave Detectors.* PhD thesis, Massachusetts Institute of Technology, 1997.

[37] Justin Greenhalgh. Investigation of blade spring design parameters. Technical Report LIGO-T030285, LIGO Project, 2003.

[38] Warren Young, Richard G Budynas, Richard Budynas, and Ali Sadegh. *Rourke's Formulas for stress and strain.* McGraw-Hill, 2011.

[39] Calum I. Torrie, Ken Mason, Dennis Coyne, Janeen Romie, Doug Cook, Mike Meyer, Mick Flanigan, and Norna Robertson. Process for manufacturing cantilever spring blades for advligo. Technical Report LIGO-E0900023, LIGO Project, 2010.

[40] Dennis Coyne. Ligo vacuum compatible materials list. Technical Report LIGO-E960050, LIGO Project, 1996.

[41] Michael Smith and Jesse Amato-Grill. Design equations for initially flat blade springs at arbitrary mounting angles. Technical Report LIGO-T0900324, LIGO Project, 2009.

[42] Giacomo Ciani. Ham auxiliary suspensions modeling and test results. Technical Report LIGO-T1000339, LIGO Project, 2010.

[43] James Lough. *Optical Spring Stabilization*. PhD thesis, Syracuse University, 2014. Dissertations - ALL. Paper 172.

[44] David Kelley, James Lough, Fabian Mangaña Sandoval, Antonio Perreca, and Stefan W. Ballmer. Observation of photothermal feedback in a stable dual-carrier optical spring. *Phys. Rev. D*, 92:062003, Sep 2015.

[45] Gregory M Harry and the LIGO Scientific Collaboration. Advanced ligo: the next generation of gravitational wave detectors. *Classical and Quantum Gravity*, 27(8):084006, 2010.

[46] J. Degallaix et. al. Advanced Virgo Status. In G. Auger, P. Binétruy, and E. Plagnol, editors, *9th LISA Symposium*, volume 467 of *Astronomical Society of the Pacific Conference Series*, page 151, January 2013.

[47] Kentaro Somiya. Detector configuration of KAGRA: The Japanese cryogenic gravitational-wave detector. *Class.Quant.Grav.*, 29:124007, 2012.

[48] V.B. Braginsky, M.L. Gorodetsky, and S.P. Vyatchanin. Thermo-refractive noise in gravitational wave antennae. *Physics Letters A*, 271(56):303 – 307, 2000.

[49] M. Cerdonio, L. Conti, A. Heidmann, and M. Pinard. Thermoelastic effects at low temperatures and quantum limits in displacement measurements. *Phys. Rev. D*, 63:082003, Mar 2001.

[50] M. Evans, S. Ballmer, M. Fejer, P. Fritschel, G. Harry, and G. Ogin. Thermo-optic noise in coated mirrors for high-precision optical measurements. *Phys. Rev. D*, 78:102003, Nov 2008.

[51] V.B. Braginsky, M.L. Gorodetsky, and S.P. Vyatchanin. Thermodynamical fluctuations and photo-thermal shot noise in gravitational wave antennae. *Physics Letters A*, 264(1):1 – 10, 1999.

[52] M. De Rosa, L. Conti, M. Cerdonio, M. Pinard, and F. Marin. Experimental measurement of the dynamic photothermal effect in fabry-perot cavities for gravitational wave detectors. *Phys. Rev. Lett.*, 89:237402, Nov 2002.

[53] Stefan W. Ballmer. Photothermal transfer function of dielectric mirrors for precision measurements. *Phys. Rev. D*, 91:023010, Jan 2015.

[54] D. Heinert, K. Craig, H. Grote, S. Hild, H. Lück, R. Nawrodt, A. Simakov, D. V. Vasilyev, D. P. Vyatchanin, S. and H. Wittel. Thermal noise of folding mirrors. *Phys. Rev. D*, 90:042001, Aug 2014.

[55] M. M. Fejer, S. Rowan, G. Cagnoli, D. R. M. Crooks, A. Gretarsson, G. M. Harry, J. Hough, S. D. Penn, P. H. Sneddon, and S. P. Vyatchanin. Thermoelastic dissipation in inhomogeneous media: loss measurements and displacement noise in coated test masses for interferometric gravitational wave detectors. *Phys. Rev. D*, 70:082003, Oct 2004.

[56] Eric D. Black. An introduction to pounddreverhall laser frequency stabilization. *American Journal of Physics*, 69(1):79–87, 2001.

[57] L. Barsotti and M. Evans. Modeling of alignment sensing and control for advanced ligo. Technical Report LIGO-T0900511, LIGO Project, 2009.

[58] T. Isogai, J. Miller, P. Kwee, L. Barsotti, and M. Evans. Loss in long-storage-time optical cavities. *Opt. Express*, 21(24):30114–30125, Dec 2013.

Curriculum Vitae

Title of Dissertation

Angular trapping of a mirror using radiation pressure

Full Name

David B. Kelley

Place and Date of Birth

Poughkeepsie, New York December 3, 1987

Colleges and Universities,	Years attended and degrees
Massachusetts Institute of Technology	2006–2010, B.S.
Syracuse University	2010–2015, M.S.,Ph.D.

Publications

1. Perreca A, Lough J, Kelley D, and Ballmer S W, *Multidimensional optical trapping of a mirror*, prd **89** 122002 (June 2014)

2. Kelley D, Lough J, Manga na Sandoval F, Perreca A, and Ballmer S W, *Observation of photothermal feedback in a stable dual-carrier optical spring*, Phys Rev D **92** 062003 (Sep 2015), `http://link.aps.org/doi/10.1103/PhysRevD.92.062003`

Awards and Fellowships

2010 Syracuse Graduate Student Fellowship

Major Department

Physics